ABSTRACT

Title of Document: OPTICAL COHERENCE TOMOGRAPHY AS A DIAGNOSTIC TOOL IN RENAL TRANSPLANT AND CANCER IMAGING

Jeremiah Wierwille, Doctor of Philosophy, 2011

Directed By: Assistant Professor Dr. Yu Chen, Fischell Department of Bioengineering

This dissertation aims to investigate optical coherence tomography (OCT) as a diagnostic technology in renal imaging through two main arenas: renal transplantation and renal cancer.

Part 1: Ischemia-reperfusion injury, which frequently occurs after kidney transplant, is a major contributing factor in delayed-graft function leading to varying degrees of early renal dysfunction. Real-time assessment of graft morphological and hemodynamic changes could help to evaluate graft condition and offer valuable information to predict the prognosis of graft injury for patient-specific management strategies. Previous studies have shown the ability of OCT to monitor structural changes associated with ischemia-reperfusion injury *in vivo*. Therefore, we investigated the ability of Doppler OCT (DOCT) to image microcirculatory changes in real time in the kidney glomerulus *in vivo* in an animal model and quantified observed changes in blood flow in 3D. Then, we translated OCT/DOCT technology into clinical testing for renal imaging

during transplantation procedures and demonstrated the ability of OCT/DOCT to reveal renal tubular morphology and blood flow immediately following reperfusion.

Part 2: For solid renal masses, nephron sparing procedures have been developed as an alternative to radical nephrectomy. However, achieving a negative tumor margin is critical to ensuring the best oncological efficacy for precluding tumor recurrence. OCT is a high-resolution, real-time imaging technology that has shown the ability to distinguish cancerous tissue from normal in several systems of the body based on changes in tissue optical properties. Therefore, we investigated the capability of OCT to quantify differences in optical properties between tumor and normal renal tissue. However, we did not observe a significant difference in optical attenuation between tumor and normal tissue in *ex vivo* specimens. These results suggest that further studies or possible alternative metrics need to be investigated to determine if OCT is able to detect renal neoplasms.

OPTICAL COHERENCE TOMOGRAPHY AS A DIAGNOSTIC TOOL IN RENAL TRANSPLANT AND CANCER IMAGING

By

Jeremiah Wierwille

Dissertation submitted to the Faculty of the Graduate School of the
University of Maryland, College Park, in partial fulfillment
of the requirements for the degree of
Doctor of Philosophy
2011

Advisory Committee:
Assistant Professor Yu Chen, Chair
Professor Peter Andrews
Associate Professor Keith Herold
Associate Professor Michael Phelan
Associate Professor Nam Sun Wang, Dean's Representative

Dedication

This dissertation is dedicated to my wonderful wife Lauren and to my family for being a never ending source of love and support throughout the program at the University of Maryland. I also want to dedicate this work to the friends I have made during the last several years in my doctoral studies. Coming to a new place where you do not know anyone can be lonely, but their friendship helped me to work harder and succeed.

Acknowledgements

First, I would like to thank my adviser, Dr. Yu Chen, for welcoming me into his lab as one of his students and teaching me about the incredible world of optical imaging. His guidance and instruction have helped me develop as a scientist and researcher over the past several years. I am grateful for the time and energy he has put into educating and training me on various optical imaging technologies, specifically optical coherence tomography and fluorescence confocal scanning microscopy. Also, I am thankful for his constant support especially in the form of his constructive criticism that has continually challenged me to improve my research faculties. Finally, I am glad to have had the privilege to work with Dr. Chen because I do not think there is a nicer guy any student could have had as an adviser.

I would also like to thank other individuals who have aided me along the way in my research. To begin with, I want to thank my lab mates Chao-Wei Chen and Chia-Pin Liang. They have been my constant companions in the lab over the past couple years helping me conduct research, trouble-shoot problems, and, most essentially, in keeping the lab light-hearted and fun. I also want to thank Dr. Shuai Yuan for showing me the ropes when I first entered the lab and for allowing me to help him on several projects to get my feet wet during my first year.

A special thank you goes to my former adviser, Dr. Keith Herold, who first mentored me, got me started in graduate research, and provided me incredible experiences and discussions with Dr. Magdi Saba and Dr. Steven Shorofsky at the University of Maryland Medical Center in Baltimore. I enjoyed all the stimulating

discussions we had and learning I received working together on the VTSO project.

I also want to acknowledge many collaborators I have worked with during my research. First, I want to thank Dr. Peter Andrews who was willing to be a major part of the first two projects in this dissertation. He helped me in many aspects my research on the kidney by passing on knowledge about animal surgery, physiology/pathology of the kidney, and for being a visionary for the application of optical coherence tomography in renal imaging. In addition, I want to thank Dr. Maristela Onozato for her expertise and aid on the animal studies too. Next, I want to thank Dr. Michael Phelan at the University of Maryland Medical Center for allowing me to do a clinical trial with him and for being flexible and understanding all the times I showed up at the last minute, and I want to thank Dr. Keith Melancon at Georgetown University Medical Center for his helping in the kidney transplant imaging research. My thanks also go to Dr. Tongtong Wu for her helpful insights and assistance on the statistical analysis of our clinical data.

Of course, I want to give my sincerest thanks and appreciation to my irreplaceable wife, Lauren, who has been by my side throughout my graduate work. I cannot over-express my thanks to her for her understanding and for the sacrifices she has made. A huge thanks also goes out to my family, especially my parents, for their love and support. They have been a source of inspiration, motivation, and wisdom during the ups and downs of graduate school.

I also want to give my thanks to the editors and reviewers of my manuscripts for critically evaluating my work and supplying constructive feedback that I could incorporate and further refine my research. I thank my dissertation committee as well for

their help and direction in my research.

Table of Contents

Dedication ii
Acknowledgements iii
List of Tables ix
List of Figures x
Abbreviations xiii
1. Introduction 1
1.1. Biomedical Optics 2
1.2. Optical Imaging 4
1.3. Optical Coherence Tomography 9
1.3.1. Light Source, Interferometry, and System Design 10
1.3.2. Axial Resolution 17
1.3.3. Transverse Resolution 20
1.3.4. Sensitivity 24
1.3.5. Phase Stability 25
1.3.6. Advantages of OCT 27
1.3.7. Clinical Potential of OCT 28
1.4. Doppler Optical Coherence Tomography 29
1.4.1. Principle and Calculation of Doppler Velocity 30
1.4.2. Detection Limits of DOCT 32
1.4.3. Determination of Flow with DOCT 33
2. Background on the Clinical Application 36
2.1. The Renal System 36
3. Rat Kidney Blood Flow Imaging 42
3.1. Introduction 42
3.2. Material and Methods 44
3.2.1. Optical Coherence Tomography (OCT) and Doppler OCT 44
3.2.2. Animal Model and Experimental Setup 45
3.2.3. OCT/DOCT Image Processing and Quantification 46
3.2.4. Statistical Analysis 50
3.3. Results 51
3.4. Discussion 59

3.5. Conclusion 62
4. OCT/DOCT Imaging of Human Kidney Transplant 63
4.1. Introduction 63
4.1.1. Kidney Injury 63
4.1.2. Renal Blood Flow Imaging Modalities 64
4.1.3. Optical Imaging Techniques for Renal Monitoring and Evaluation 69
4.2. Material and Methods 70
4.2.1. OCT System Setup and Design 70
4.2.2. Transplant Patients and Data Collection 75
4.2.3. Image Analysis 78
4.2.4. Evaluation of Post-Graft Function 80
4.3. Results 80
4.3.1. Ex Vivo Kidney Imaging 80
4.3.2. In Vivo Kidney Imaging 81
4.4. Discussion 89
4.4.1. Critique of Methods 91
4.4.2. Future Direction 91
4.5. Conclusion 93
5. OCT Imaging of Renal Cancer in Humans 95
5.1. Introduction 95
5.1.1. Renal Cancer 95
5.1.2. Renal Cancer Treatment 96
5.1.3. OCT Imaging 97
5.1.4. Previous Studies 98
5.2. Materials and Methods 100
5.2.1. Renal Specimen 100
5.2.2. Sample Preparation 101
5.2.3. Data Collection 101
5.2.4. Image Analysis 103
5.2.5. Pathological Evaluation 104
5.2.6. Statistical Analysis 105
5.3. Results 106

5.4. Discussion 110
5.5. Conclusions 115
6. Conclusion 116
6.1. Summary and Impact of Work 116
6.2. Future Work 118
6.3. Conclusions 120
7. References 124

List of Tables

Table 1. OCT System Specifications. 14

Table 2. Scoring System for Semi-Quantitative Image Analysis..... 79

Table 3. Human Kidney Transplant Semi-Quantitative Image Analysis..... 87

Table 4. Patient demographical and pathological data..... 105

Table 5. Patient-specific pathological diagnoses from Figure 46. 110

List of Figures

Figure 1. Transmission versus reflectance imaging modes. 5

Figure 2. Light scattering in tissue 6

Figure 3. Absorption spectra for biological tissue 7

Figure 4. Spatial resolution versus depth of penetration for various imaging techniques . 8

Figure 5. Michelson interferometer diagram used for performing low-coherence interferometry. 11

Figure 6. Coherence fringe for low-coherence light source 12

Figure 7. Fourier-domain, swept-source optical coherence tomography (OCT) system setup 13

Figure 8. Formation of OCT image 15

Figure 9. OCT swept-source laser power spectrum 16

Figure 10. OCT axial resolution calibration using stationary mirror 19

Figure 11. Depth of penetration calibration 20

Figure 12. Focusing gate and the effect on transverse resolution 22

Figure 13. Transverse resolution 24

Figure 14. OCT phase stability 26

Figure 15. DOCT calibration using tube phantoms 32

Figure 16. Calculation of flow from DOCT velocity 34

Figure 17. DOCT flow rate calibration using capillary tubes 35

Figure 18. Frontal section of the human kidney 37

Figure 19. Kidney nephron 38

Figure 20. Kidney glomerulus (filtering component in the nephron) 39

Figure 21. Normal versus cancerous *ex vivo* kidney tissue..... 41

Figure 22. OCT/DOCT Microscope Setup 45

Figure 23. Manual selection of glomerular boundary..... 48

Figure 24. Flow chart describing CDV and Doppler flow calculations..... 50

Figure 25. OCT and DOCT imaging of rat glomerulus..... 52

Figure 26. (A) Top-down (vertical projection) view showing numerous clustered DOCT signals within the glomerulus representing red blood cell velocities. Image size: 325 × 278 μm. (B) Three-dimensional (3D) rendering of the 3D OCT/DOCT data set of the glomerulus..... 54

Figure 27. Representative OCT and DOCT images (XZ) from 3 different physiological states..... 56

Figure 28. Blood flow histogram comparison 57

Figure 29. Analysis of in vivo DOCT imaging of rat glomeruli..... 58

Figure 30. Schematic of hand-held OCT imaging probe for intra-operative kidney imaging 72

Figure 31. Demonstration of OCT handheld probe used in ex vivo and in vivo kidney transplant imaging..... 73

Figure 32. Portable hand-held OCT imaging system setup for clinical imaging during kidney transplantation.. 74

Figure 33. Intra-operative OCT/DOCT imaging of kidney post-reperfusion..... 77

Figure 34. Examples of *in vivo* OCT images of human kidney depicting the scoring descriptions in Table 2 for tubule size/shape and tubule density/uniformity 80

Figure 35. *Ex vivo* OCT imaging of human donor kidney..... 81

Figure 36. OCT imaging of *in vivo* human kidney showing open uriniferous tubules below the renal capsule 82

Figure 37. OCT imaging of *in vivo* human kidney showing uriniferous tubules below the renal capsule 83

Figure 38. OCT/DOCT imaging of *in vivo* kidney 84

Figure 39. OCT/DOCT imaging of *in vivo* human kidney showing regional variations in the openness of uriniferous tubules 85

Figure 40. Additional OCT/DOCT imaging of *in vivo* human kidney showing regional variations in the openness of uriniferous tubules 85

Figure 41. *In vivo* human kidney showing open tubules and cortical blood flow. 86

Figure 42. Summary of serum creatinine values for the first post-operative week.. 88

Figure 43. Correlation between serum creatinine at day 1 and day 8 post-operative and the OCT/DOCT image scoring index 89

Figure 44. Location of OCT imaging during both (A) radical and (B) partial nephrectomy 103

Figure 45. Representative OCT images and axial profiles for renal tissue 107

Figure 46. Representative OCT images from normal and tumor regions for all patients 108

Figure 47. Quantitative OCT imaging analysis results 110

Abbreviations

2D	Two-Dimensional
3D	Three-Dimensional
AKI	Acute Kidney Injury
AML	Angiomyolipoma
A-SCAN	Axial Scan
ASL	Arterial Spin Labelling
CDV	Cummulative Doppler Volume
CE	Contrast Enhanced
CM	Confocal Microscopy
CT	Computed Tomography
DCE	Dynamic Contrast Enhanced
DFR	Doppler Flow Range
DOCT	Doppler Optical Coherence Tomography
DOT	Diffuse Optical Tomography
FOV	Field-of-View
FWHM	Full-Width Half-Maximum
GV	Glomerular Volume
IL	Intralipid
LOT	Laminar Optical Tomography
MPM	Multi-Photon Microscopy
MRI	Magnetic Resonance Imaging
n	Refractive Index
NA	Numerical Aperture
OCT	Optical Coherence Tomography
PAT	Photoacoustic Tomography
PET	Positron Emission Tomography
RBF	Renal Blood Flow
RCC	Renal Cell Carcinoma
SNR	Signal-to-Noise Ratio
SPECT	Single-Positron Emission Computed Tomography
TCC	Transition Cell Carcinoma
US	Ultrasound
USAF	United States Air Force
XY	En-Face
XZ	Cross-sectional
2D	Two-Dimensional

1. Introduction

Optical coherence tomography (OCT) is a high-resolution optical imaging modality that holds much promise for clinical medicine as it is capable of acquiring micrometer level images of the biological tissue subsurface. The interest in OCT as a diagnostic medical imaging tool has exploded over the past decade due to the performance and versatility of its application, and its capacity is constantly being transformed because of the technological advances with light sources, detectors, and processing algorithms. These attributes have pushed OCT into the spotlight for bed-side use in the clinic for diagnostic imaging. OCT is able to measure the optical properties of tissue and retrieve structural information (backscattered light intensity) as well as characterization and state of biological tissue (attenuation coefficient, phase, polarization, and other optical properties). Altogether, OCT has become a powerful tool for medical imaging. The scope of the research in this dissertation consists of three parts which investigate the utility and feasibility of OCT in renal imaging. The first section demonstrates OCT and Doppler OCT (DOCT) quantitative imaging in the living rat kidney; then, the second section translates that technique into the clinic to demonstrate real-time OCT/DOCT imaging of the living human kidney during renal transplantation; finally, the last section investigates the ability of OCT to distinguish between cancerous and normal renal tissue in human renal cancer patient specimens (ex vivo) by evaluating the differences in their optical properties. This opening chapter serves to introduce OCT and its place in the field of biomedical optics and provide a foundation upon which to explore the work presented herein.

1.1.Biomedical Optics

In a broad sense, biomedical optics is a field that deals with the application of light in the ultraviolet-visible-infrared regions of the electromagnetic spectrum for diagnostic and therapeutic purposes. The field has evolved rapidly since the first reported study of laser technology in the 1960 by Maiman.[1] Diagnostic applications primarily include imaging and spectroscopy, and for therapeutic applications, various forms of light-based therapy have been introduced and many have already been incorporated into common clinical practice. Also, the nature of the physical interaction between light and biological tissue is an important area of study in this field.

Lasers have become a standard tool in clinics for several applications, the largest consisting of medical laser surgery and treatment. The application of lasers in medicine can be broken down in to approximately five categories based on the fluence rate of the laser light applied to biological tissue. On the higher end of laser fluence rates is the photomechanical mode of laser therapy that is primarily used in ophthalmology for non-invasive iridectomies and capsulectomies to puncture holes in the iris and remove tissue in the eye.[2] Then, a step down in laser fluence yields the ablative mode that is also used in ophthalmology for treating keratotomy, various forms of keratophakia, and corneal ablation,[3-5] and it is also used in angioplasty[6, 7] and joint surgery.[8] Another mode with yet lower fluence, is the photothermal mode, which has become prominent in the field of oncology for selectively treating cancer using photosensitive particles (e.g. endogenous chromophores, fluorescent dyes, and gold nanoparticles),[9-12] and recently in laser immunotherapy for treating metastatic cancer.[13, 14] In addition, at this level of irradiation

blood coagulation (thrombogenicity) can be achieved in small vessels.[15] Then, at lower fluence rates below hyperthermia is the photochemical mode. Photodynamic therapy is most popular form of this mode for treating certain diseases by causing the generation of singlet oxygen species through photochemical reactions with non-thermal, low doses of light irradiation.[16, 17] Finally, at low fluence rates light can be used for a number of biostimulation and wound healing treatments.[18] Low laser level therapy (LLLT) that is part of this category has also been proposed to support treating tinnitus, epilepsy, pain, thrombosis, light hypersensitivity, physical trauma or surgery recovery, hyperlipidemia, and strengthening of the immune system.[19] The application of light has found its way into a variety of different medical applications with varying intensities, wavelengths, and transmissions.

Imaging as a medical diagnostic tool has been developed and used abundantly with new techniques and methods being developed aggressively in recent decades. Non-optical imaging methods such as MRI, CT, US, X-ray, etc. are widely used to assist in the diagnosis, treatment, and monitoring of various diseases or injury. In light of the widespread advantages imaging provides physicians, every technique has inherent drawbacks and limitations whether it is resolution, acquisition time, sensitivity, specificity, safety, or cost. New imaging technology is constantly being investigated and tested to overcome or alleviate these limitations. Optical imaging has come to be widely used in biomedical imaging on account that its strengths can satisfy several of these criteria above competing technology. The use of optics can be less expensive, provide high-resolution and quick imaging time, be highly accurate, ensure minimal health risk, and designed to be portable or miniaturized. However, optical imaging techniques are far

from a universal answer to all imaging issues as they carry their own inherent limitations such as small field-of-view, shallow imaging depths compared to other modalities, and inability to detect certain biological parameters that other imaging techniques can detect. In essence, optical imaging fits into the biomedical imaging scene to offer certain advantages over other modalities but is also limited in capability compared to other modalities. In the next section, techniques and applications of optical imaging will be introduced and covered.

1.2.Optical Imaging

In the field of biomedical optics, optical imaging techniques are directed at the use of light for the visualization and investigation of biological tissues. Two modes of imaging are employed to collect a signal from tissue: transmission mode and reflectance mode. Using transmission mode, such as in conventional brightfield microscopy, light is propagated through a sample and collected by a detector on the opposing side as the source (see Figure 1A). In contrast, optical imaging that relies on reflectance mode operates by collecting light that has entered the sample, collided with molecules in the tissue, scattered in different directions, and ultimately exits the tissue and returns to a detector that is on the same side as the light source (see Figure 1B).

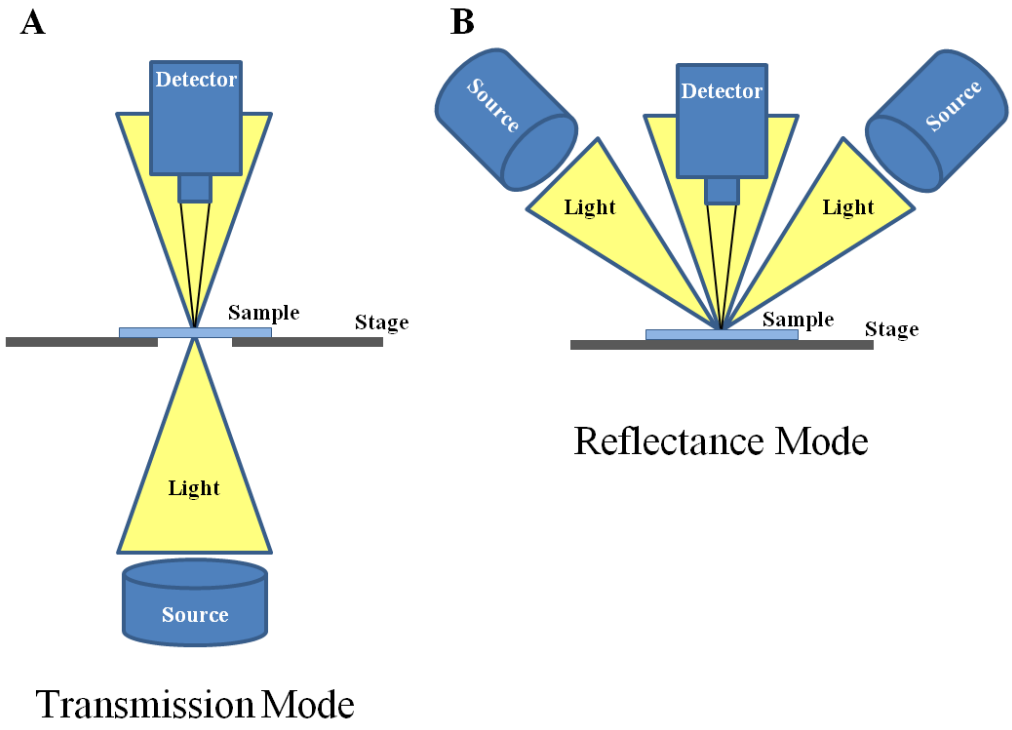

Figure 1. Transmission versus reflectance imaging modes.

When light enters tissue it interactions with the molecules of the tissue as it propagates through. However, when light interacts with tissue subtle changes occur in the property of the light. Depending on the index of refraction, the light might be bent at different angels as it enter different substances in the tissue, and when it encounters cellular structures light protein fibers, cell membranes, organelles, nuclei, etc. the light is scattered in random directions. The degree of scattering is a function of the size, orientation, and refractive index of the structures the light collides with. An example of how light scatters as it enter tissue is depicted below in Figure 2.

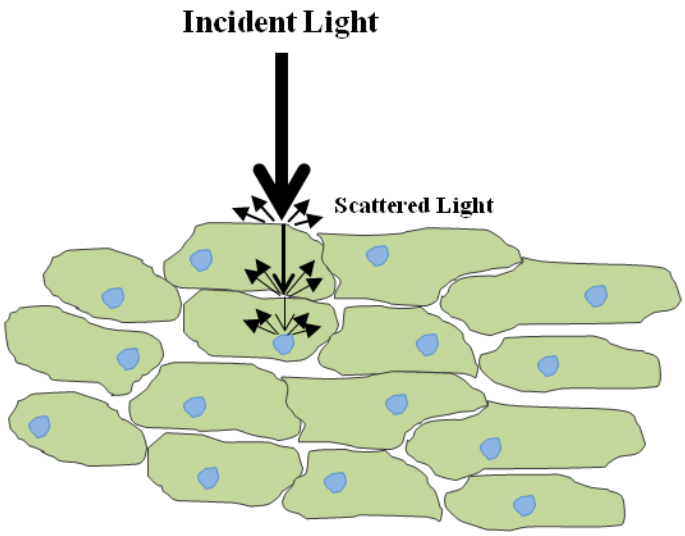

Figure 2. Light scattering in tissue. As light passes through each structural barrier, light is scattered causing the intensity of the propagating beam to be diminished.

Another way that light interacts with tissue besides scattering is through absorption within tissue. Certain components of cells inherently absorb light. Main light absorbers in tissue consist of water, hemoglobin (both in its oxygenated form and deoxygenated form), and melanosomes (see Figure 3). Absorption peaks of these various constituents can be used as a diagnostic marker for their presence and concentration in tissue. Absorbed light can also be re-emitted through several mechanisms, such as fluorescence, Raman scattering, and others that are associated with specific energy shifts and timescales with respect to the absorbed photons.

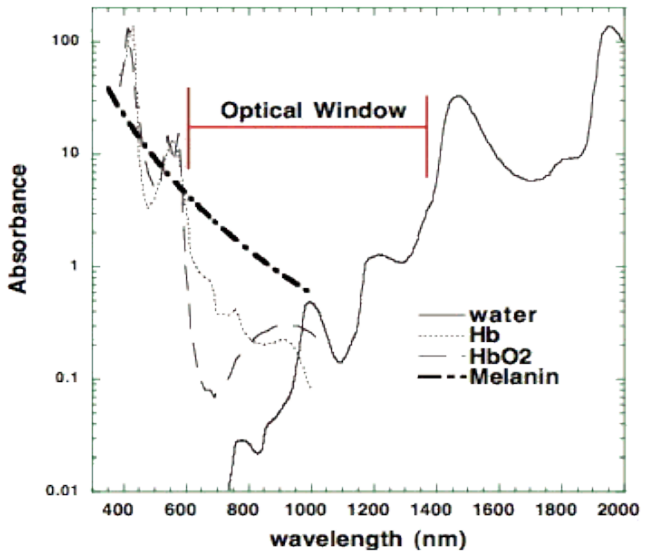

Figure 3. Absorption spectra for biological tissue. The various curves depict the absorption of predominant endogenous constituents of tissue, i.e., water, deoxyhemoglobin (Hb), oxygenated hemoglobin (HbO_2), and melanin. Used by permission. Source: http://www.photobiology.info/Hamblin.html

Light transmission in biological tissue is relatively high in the wavelength range of approximately 650 to 1400 nm. The lower limit of this range is impeded by scattering and absorption of native chromophores hemoglobin and melanin and the upper limit is caused by the increased absorption of water at longer wavelengths. With these endogenous molecules as the main obstacles of light, optical imaging is optimal within the range of 650-1400 nm, which is known as the "optical window" of tissue. In this range, optical imaging can be performed at deeper penetration in the infrared region (e.g. 1300 nm) or with higher resolution in the visible-near-infrared region (e.g. 650-800 nm). Thus, optical imaging techniques must balance a close trade-off between resolution and imaging depth.

An assortment of popular imaging modalities (optical imaging as well as others such as MRI, CT, US, etc.) are presented in Figure 4 along axes that compare the achievable depth of penetration of each technique compared to their spatial resolution capability. Optical techniques cover a broad imaging range from microscopic (multi-photon microscopy) to macroscopic scales (diffuse optical tomography). As can be seen in Figure 4, there exist a rough monotonic relationship between depth of penetration and spatial resolution that is also wavelength dependent.

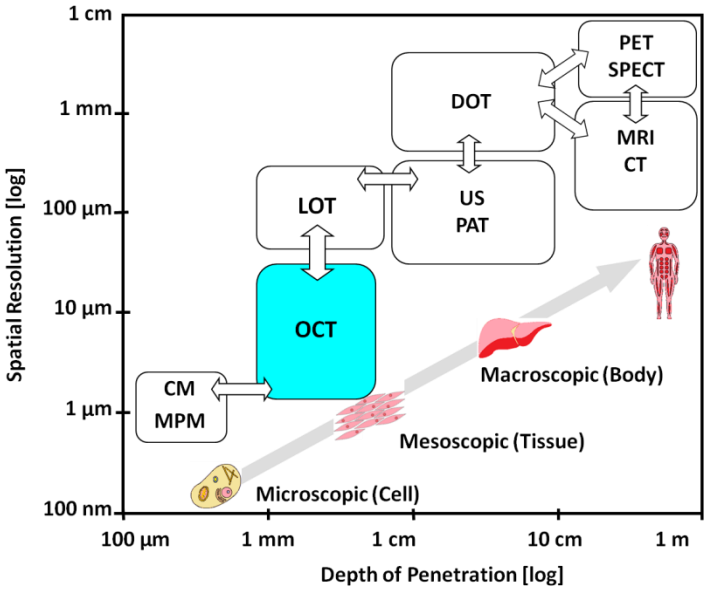

Figure 4. Spatial resolution versus depth of penetration for various imaging techniques. Abbreviations: CM: confocal microscopy; MPM: multi-photon microscopy; OCT: optical coherence tomography; LOT: laminar optical tomography; US: ultrasound; PAT: photoacoustic tomography; DOT: diffuse optical tomography; MRI: magnetic resonance imaging; CT: computed tomography; PET: positron emission tomography; SPECT: single-photon emission computed tomography.

High-resolution optical imaging techniques, like confocal microscopy and multi-photon microscopy on the lower left hand side of Figure 4, can achieve very high spatial

resolution but comparatively shallow depth penetration. With these high-resolution techniques, contrast is provided by staining, exogenous fluorescent probes, or endogenous fluorophores. Typically, these techniques are employed for 2D planar imaging. 3D imaging is possible using dynamic optics to adjust the focusing depth during image acquisition, but can only be acquired in scattering media (biological tissue) by beam scanning.

Conversely, deep penetrating optical imaging techniques, like diffuse optical tomography, offers the ability to image with a wide field-of-view but at the expense of lower resolutions (trade-off is on the order of 3 magnitudes for both parameters). Significant research in recent years has been dedicated to developing this technique for mammography screening as a viable option to replace current X-ray mammography.[20-22] Currently, X-ray mammography utilizes ionizing radiation but this may be replaced soon with non-ionizing optical mammography techniques.

Between the two extremes of these optical imaging techniques (MPM and DOT) is optical coherence tomography (OCT), which is a reflectance based optical imaging technique that can provide microscopic to mesoscopic scale imaging with no need of exogenous contrast agents. The research presented in this thesis targets the translation of this imaging technique as it applies to possible uses in the field of nephrology. Specifically, we investigate if OCT can be used for applications in renal transplant and renal cancer patients.

1.3.Optical Coherence Tomography

Optical coherence tomography (OCT) is a non-invasive, high-resolution,

coherence-based imaging technology that uses infrared or near-infrared light to acquire cross-sectional images or three-dimensional (3D) volumes of the subsurface microstructure of superficial tissues. Since its emergence in the early 1990s,[23] OCT has become a highly investigated imaging technology on account of its potential for medical diagnosis and monitoring of therapy non-invasively in vivo with resolutions approaching that of conventional histology.[24] In situ and in vivo visualization of biological tissue at high resolution was not achievable with histopathology. OCT is a non-contact, interferometric imaging modality that can resolve subsurface structures non-destructively within intact tissue. With this capability OCT can offer an "optical biopsy" approach for tissue that cannot be excised such as retinal tissue and vascular tissue, and easy access to the inner surfaces of hollow organs and body cavities such as the gastrointestinal tract and urinary tract/bladder.

Cross-sectional OCT images are produced by scanning the beam across the surface of the sample and collecting a series of axial (vertical) profiles which formulate a two-dimensional (2D) image. Axial profiles of the sample are produced by low-coherence interferometry of the backscattered light from the sample. The magnitude of this backscattered light at a given depth in the axial profile is represented in a 2D cross-sectional image by the pixel intensity at the corresponding point for a particular echo time delay. A more thorough technical explanation regarding OCT will be provided in the following section(s).

1.3.1. Light Source, Interferometry, and System Design

OCT forms an image representing the internal structure of a sample by measuring

echo delays and the intensities of back-reflected light. Since the velocity of light is too fast to clock with electronic equipment, the timing of echo delays cannot be directly measured. The way OCT determines the location of optical echo delays is through a technique called low-coherence interferometry. In low-coherence interferometry, back-reflected or backscattered light is measured against light that travels a known reference path. The classic Michelson interferometer design is shown below in Figure 5.

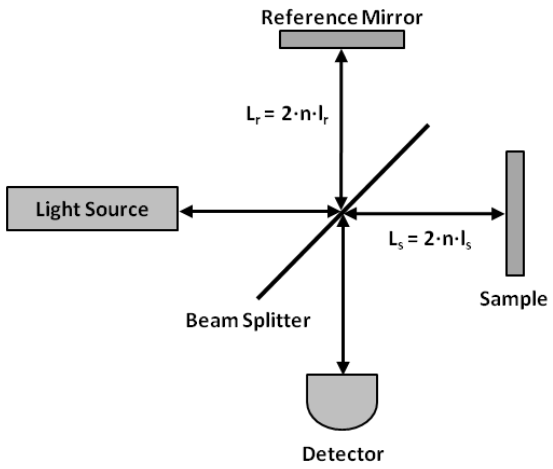

Figure 5. Michelson interferometer diagram used for performing low-coherence interferometry.

Because detector response times cannot compare with the high speed of light, the Michelson interferometer compares light backscattered from a sample with light from a "reference" mirror, which consists of a mirror with a predetermined path length correlating to a specific depth location in the sample. Michelson interferometry operates by splitting a beam from a low-coherence light source into two separate paths using fiber optics to control the path of the light. One "arm" of the interferometer contains a modulating probe that focuses the beam and can scan it across the surface of the sample.

This "arm" is responsible for directing the beam and then additionally collecting backscattered light as it returns from the sample. The other "arm" contains the known reference path which is a mirror that causes the light to travel a specified distance. The total round-trip path length (L_r) for the "reference" arm is equal to $2nl_r$ where n is the index of refraction (typically equal to 1.0 for air) and l_r is the distance the mirror is away from the beam splitter where the light is initially separated. The path length of the "sample" arm is similar $L_s = 2nl_s$. Interference between the sample and reference signals returning from the sample and the mirror only occurs within the "coherence gate (length)" of the light source. For a low-coherence light source the gating window is equal to Δz as show below in Figure 6.

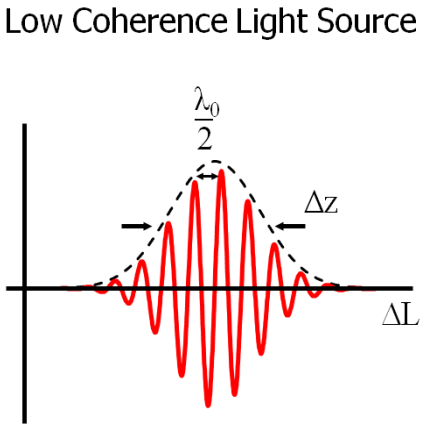

Figure 6. Coherence fringe for low-coherence light source. λ_0 is the center wavelength, Δz is the full-width, half-maximum (FWHM) distance, and ΔL is path length difference between the sample and reference arm. $\lambda_0/2$ is the fringe period.

This means that light interferes or forms an interference pattern if the path length between the two arms of the interferometer is within the coherence length of the light. When the path length is within the coherence "gate" an interference fringe is formed

according to the recombination of light returning from each arm. However, only a fraction of the ballistic photons entering the sample are scattered and re-collected by the objective lens. These backscattered photons can enable the measurement of the sample's optical properties, specifically of interest is the light attenuation coefficient (μ_t). A conventional schematic diagram of OCT is shown below in Figure 7. The reference and sample arm from the Michelson interferometer design illustrated above in Figure 5 are labeled accordingly in Figure 7 below.

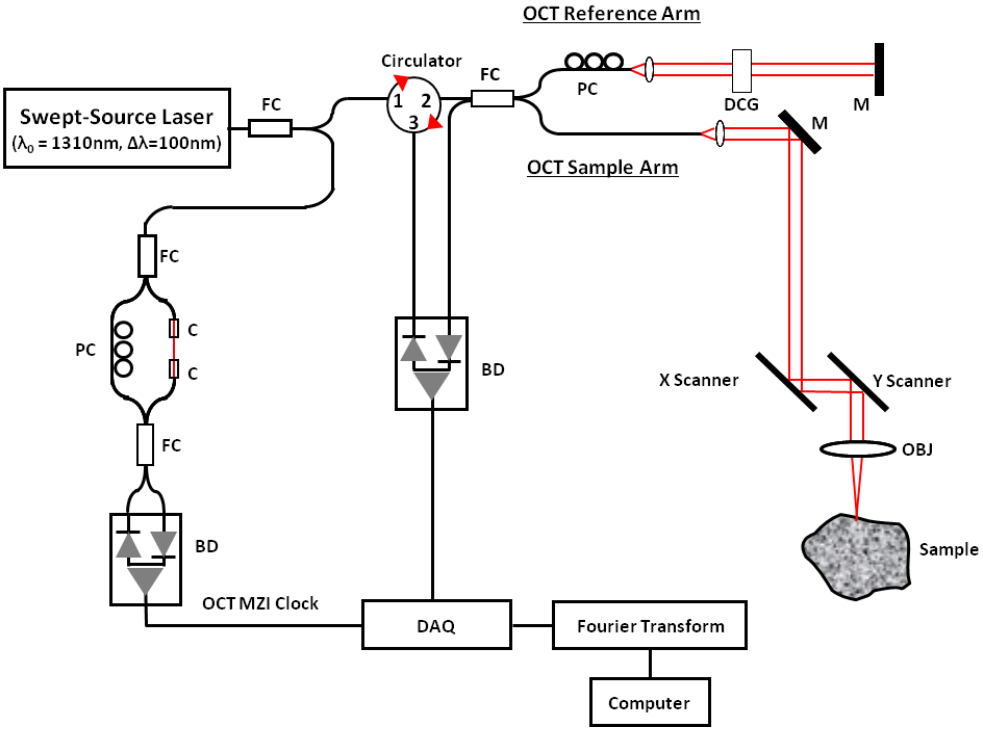

Figure 7. Fourier-domain, swept-source optical coherence tomography (OCT) system setup. Axial and transverse resolution, imaging speed, imaging depth, and field-of-view parameters are listed in Table 1 below. OCT system schematic abbreviations, FC: fiber coupler, PC: polarization controller, C: collimator, MZI: Mach-Zehnder interferometer (frequency clock), M: mirror, BD: balanced detector, DAQ: data acquisition board, DCG: dispersion compensating glasses, OBJ: objective. Light path lengths not proportional to actual distance.

As depicted above in Figure 4, OCT can have a range of penetration depths and spatial resolutions. The specifications listed below in Table 1 are general specifications for the OCT system but can be altered through using different optics or light sources.

Table 1. OCT System Specifications.

OCT Specifications	
Axial Resolution	~12 μm
Transverse Resolution	2-30 μm (variable)
Imaging Speed	1D: 16 kHz 2D: 30 Hz 3D: 17s (variable)
Imaging Depth	~1-2 mm
Field-of-View	0.2-10 mm (variable)

By scanning a beam across the surface of a sample, a 2D cross-sectional image of the sample can be generated showing the backscattered light intensity with respect to penetration depth (see Figure 8). This is performed by stacking adjacent axial scans together as the beam moves laterally across the surface of tissue. By repetitively scanning 2D cross-sectional images in this manner and stepping the beam across the surface of a sample in the direction perpendicular to the 2D scanning, a 3D volumetric image data set can be obtained enabling the generation of *en face* (lateral plane) images that are similar to normal light microscopy, and furthermore, enabling even oblique slices with arbitrary

orientation to be extracted.

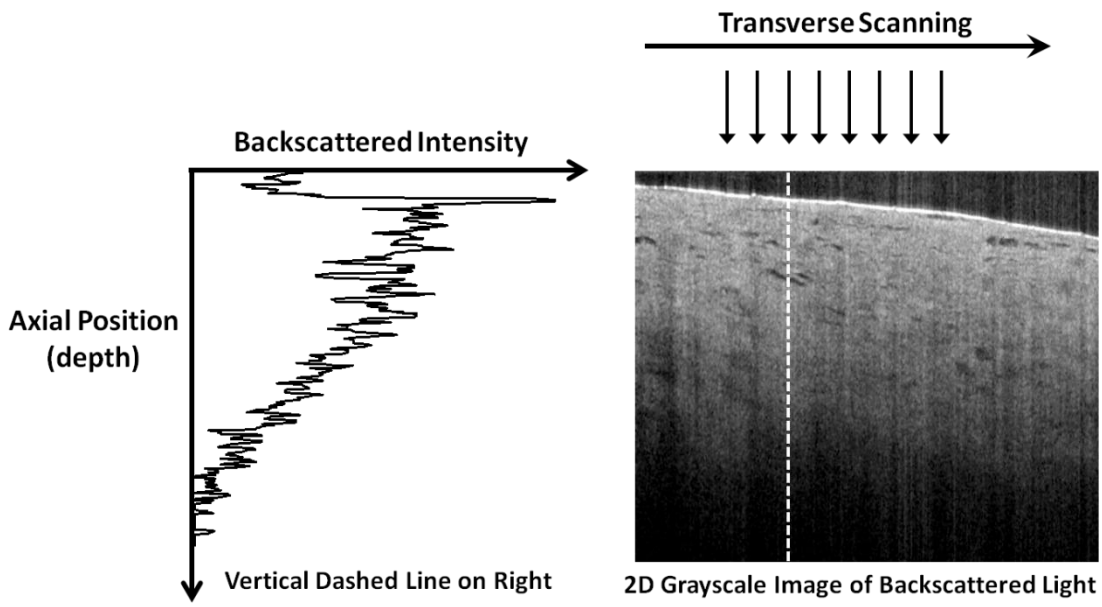

Figure 8. Formation of OCT image. OCT measures the backscattering intensity as a function of depth. Cross-sectional images are generated by scanning a beam across the tissue. A gray scale or false color image can then be displayed representing the reflected light intensity at every depth point and lateral position.

The coherence length of the light source and the spot size of the beam focus on the sample are the determining factors that determine the axial and lateral resolutions of the system. Axial and lateral resolutions are dependent upon the light source and optical components employed in constructing the OCT system. These two parameters of our OCT system design will be discussed individually in more detail in the following sections.

As was shown in Figure 3, biological tissue has less absorption and scattering in the near-infrared (NIR) / infrared (IR) wavelength range (700-1300 nm).[25] This region is

known as the "water window" or "optical window" because frequencies of light in this NIR/IR region are able to transmit better than regions lower or higher than this window. Therefore, to maximize penetration depth the wavelength of the light source should be such that absorption of the photons in the sample is minimized. The OCT system used in this research employs a 1300 nm swept-source laser with ~100 nm bandwidth. The normalized power spectrum of our light source is show below in Figure 9.

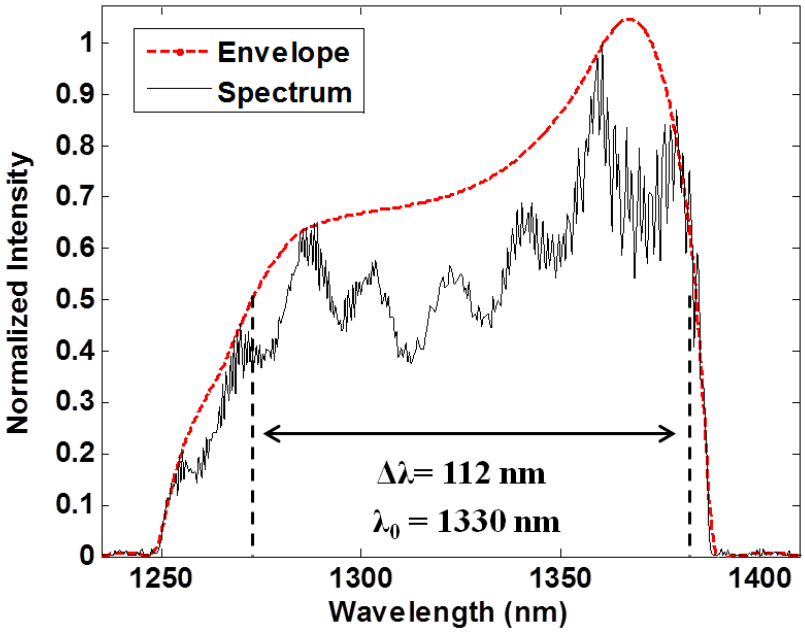

Figure 9. OCT swept-source laser power spectrum. The center wavelength (λ_0) is ~1330 nm and the FWHM bandwidth ($\Delta\lambda$) is ~112 nm. These exact specifications are listed in this thesis in general terms as λ_0 = 1300 nm and $\Delta\lambda$ = 100 nm since the spectrum has slightly changed over time during the course of the experiments.

Since imaging depth is wavelength dependent, the longer wavelength we use (1300 nm) offers better penetration than alternative light sources around 800 nm by a factor of approximately 2.[26] At NIR wavelengths light scattering is the predominant factor in signal attenuation as the degree of absorption is drastically less. But, OCT

contrast is a function of both scattering and absorption as incident light propagates through tissue and is backscattered from collision with internal structures and travels back to the objective lens. Due to the scattering and absorption effects of tissue, OCT has a relatively shallow depth of penetration. On account of the interactions between the light and tissue, the maximum imaging depth for OCT is only ~2-3 mm.

Light is attenuated both as it enters into tissue and as it travels back out. According to the Beer-Lambert law, light attenuation in tissue follows an exponential decay function. The total attenuation coefficient (μ_t) of the ballistic photons is the sum of absorbed (μ_a) and scattered (μ_s) light ($\mu_t = \mu_s + \mu_a$). But, because light scattering is much greater than absorption in the NIR region ($\mu_s >> \mu_a$), the total attenuation coefficient can be approximated by the exponential attenuation due to scattering alone ($\mu_t \approx \mu_s$). The scattering coefficient (μ_s) is a parameter that describes the probability per unit length of a photon being scattered in the tissue. Tissue/cell distribution, size, density, and orientation are all critical factors affecting light scattering. Tissue scattering properties are highly dependent on changes in the refractive index at object boundaries (e.g. cell membranes, protein fibers, etc.). Raising the refractive index mismatch between components within tissue increases the relative scattering of light as it enters the tissue.

1.3.2. Axial Resolution

OCT axial resolution is dependent upon the width and shape of the bandwidth from the light source and typically ranges from ~1-15 μm. In order to achieve a high axial resolution, the coherence length of the light source has to be as short as possible because axial resolution is determined by the coherence length of the light source. The coherence

length (Δz) is related to the center wavelength (λ_0) and the full-width-half-maximum (FWHM) bandwidth ($\Delta\lambda$) and can be calculated according to Eq. (1):

$$\Delta z = \frac{2 \cdot \ln(2)}{\pi} \cdot \frac{\lambda_0^2}{\Delta\lambda} \qquad (1)$$

Given that the coherence length of the light source in medium with refractive index *n* is *Δz/n*, some light sources with large bandwidth can offer super-high axial resolution of approximately 1 μm in tissue.[27]

Using a 1310 nm center wavelength light source with a 100 nm bandwidth, the theoretical axial resolution is 7.45 μm. Experimentally, the calibrated axial resolution using a stationary mirror as a point reflector is ~16 μm in air and ~12 μm in tissue as demonstrated in Figure 10. This is the axial (vertical) resolution of the OCT light source utilized in the research presented herein.

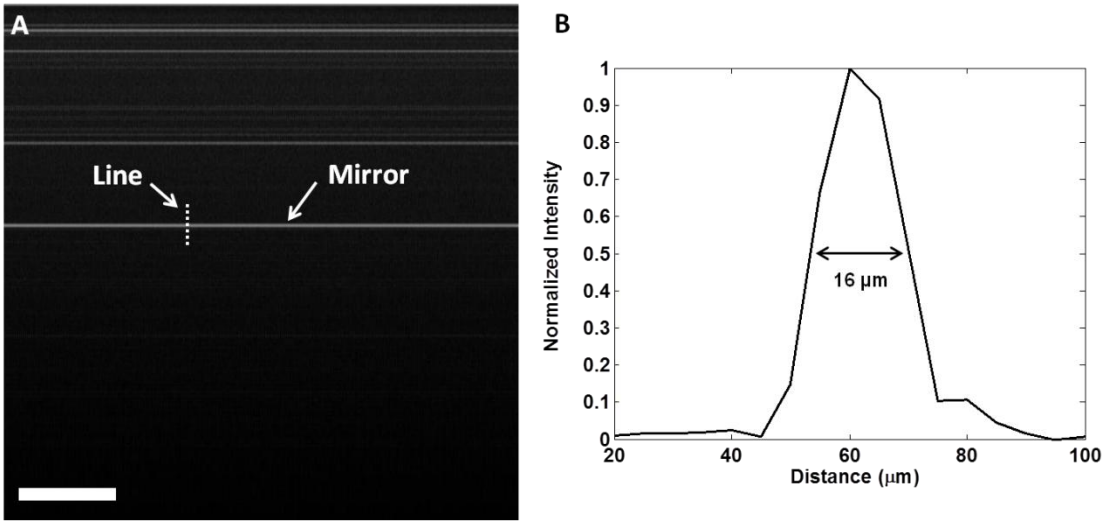

Figure 10. OCT axial resolution calibration using stationary mirror. Vertical width of mirror represents coherence length of the light source. (A) Cross-section image of stationary mirror in air. (B) Line plot of dashed line in (A) across mirror. Vertical resolution is defined as the distance at 50% FWHM. In air (n=1.0), the axial resolution is ~16 μm, and thus, in tissue (n=1.33) it is ~12 μm. [n=refractive index]

Also, our OCT system's imaging depth was determined experimentally to be 2.63 mm in air and therefore is 1.98 mm in tissue (see Figure 11). To determine the imaging distance in air, a stationary mirror is moved vertically exactly a certain specific distance using a precise micromanipulator with a microscope stage. Then, the full distance of the OCT image depth can be extrapolated from that movement. The change in the index of refraction from air (n=1.0) to tissue (n=1.33) decreases the imaging depth by the inverse factor of the index of refraction. Thus, an imaging depth in tissue is equal to 2.63 mm divided by 1.33 is equal to 1.98 mm.

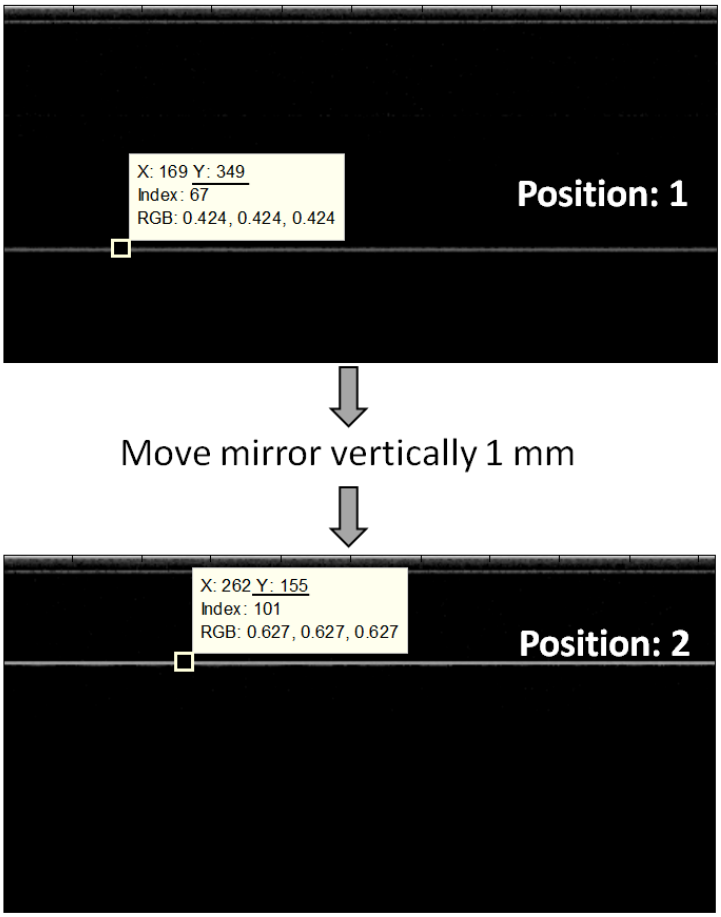

Figure 11. Depth of penetration calibration. Stationary mirror (indicated by horizontal line passing through square data cursor) was moved manually exactly 1mm vertically. The difference in pixels represents a depth of 1 mm in air. With 512 pixels per axial scan, the OCT imaging depth in air (n=1.0) was determined to be 2.6256 mm and therefore is 1.9797 mm in tissue (n≈1.33). [n=refractive index]

1.3.3. Transverse Resolution

OCT transverse resolution is dependent on the interrelation between the scan size, sampling density, and laser spot size formed according to the numerical aperture (NA) of the objective lens (focusing component) in the sample arm. The scan size is the physical distance which the beam travels across the surface of the sample and the sampling density

is a function of the step size of the beam (i.e. the number of axial scans that are recorded per 2D image). However, the minimum transverse resolution is ultimately determined by the magnification of the objective lens. Low NA lenses achieve a large spot size but longer depth of focus. In contrast, high NA lenses achieve a smaller spot size but shorter depth of focus. The relationship between the transverse resolution and depth of focus is depicted in Figure 12. The focusing gate is the light profile that is focused into the lens. A thinner focusing "waist" from a high NA lens can achieve higher transverse resolutions than a wider "waist" from a lower NA lens. The "waist" of the focusing gate is the distance at the narrowest part of the light profile, denoted by Δx.

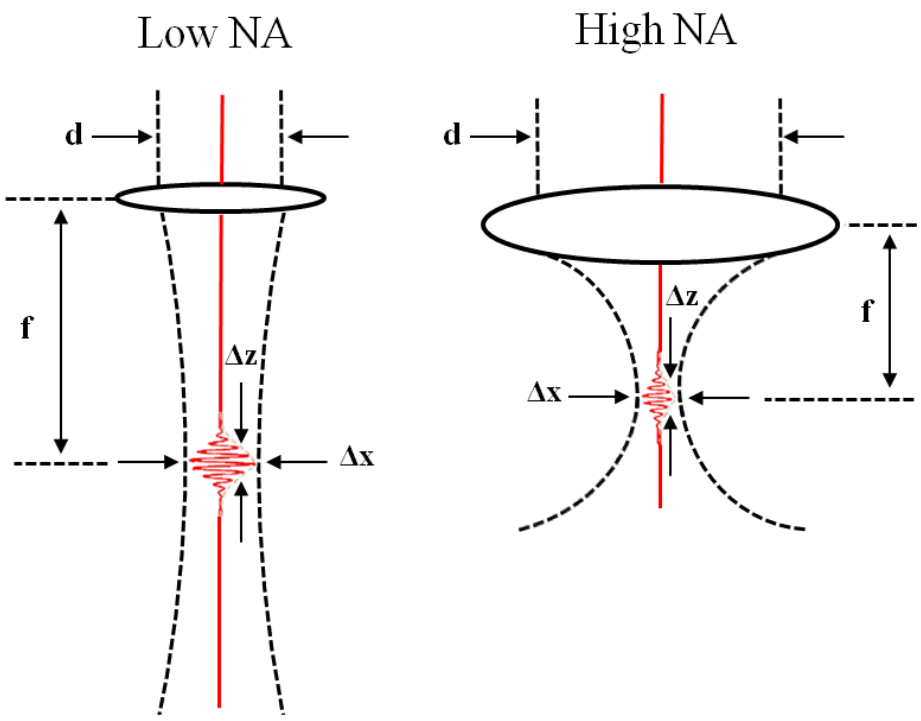

Figure 12. Focusing gate and the effect on transverse resolution. Low NA focusing achieves lower transverse resolution but longer depth of focus. High NA focusing offers the inverse, high transverse resolution but shorter depth of focus. The axial resolution is represented by Δz and the transverse resolution by Δx. For OCT, the axial resolution is dependent on the coherence length of the light source alone and is not affected by the NA of the focusing lens.

The theoretical transverse resolution (Δx) of an objective lens can be approximated according to Eq. (2):

$$\Delta x = \frac{4 \cdot \lambda_0 \cdot f}{\pi \cdot d} \tag{2}$$

where λ_0 is the center wavelength of the light source bandwidth, f is the focal distance (working distance), and d is the diameter of the objective lens. However, a more precise calculation of the transverse resolution is given according to Eq. (3):

$$\Delta x = \frac{0.44 \cdot \lambda_0}{n \cdot \sin\theta} \tag{3}$$

where λ_0 is the wavelength of the light source, n is the refractive index, and θ is half the maximum angle for the possible light that can enter/exit the objective lens.[28] Wider diameter lenses and shorter focal distances increase the transverse resolution but at the expense of depth of focus in the axial (vertical) dimension. For example, with a 10x (NA=0.25) objective lens and 1310 nm wavelength light source, the upper limit of the transverse resolution is equal to 2.28 μm. This calculation, however, does not account for the beam profile (size) or dispersion effects inherent in the optics. Experimentally, using the 1951 USAF resolution chart the upper limit of the transverse resolution for our OCT

microscope with 10x objective was determined to be ~2-3 μm (see Figure 13A). But, the resolutions of the X and Y (horizontal and vertical) dimension are not exactly equivalent because the scan sizes are slightly different between the two dimensions. The transverse resolution can be estimated by determining the separation distance between elements at a contrast intensity (C) of ~26% (see Figure 13C).[28] C is calculated according to Equation 4:

$$C = \frac{I_P - I_V}{I_P + I_V} \tag{4}$$

where I_p is the peak intensity value of the elements in the group and I_V is the valley intensity between the group elements. Using this method, the transverse resolution is determined to be ~2.7 μm. Another way to determine the transverse resolution is using the edge spread function (ESF) by finding the distance it takes to change from 10% (background intensity) to 90% (object intensity) at the edge of a flat object (i.e. vertical knife-edge).[29] According to this method, the transverse resolution was determined to be ~3.15μm, which is a little higher than the value obtained with the first method. This might be due to some error inherent in the edge spread function. If the scan size is increased but the sampling density is kept the same, the transverse resolution will decrease proportionally with the increase in scanning distance. Because different system designs and optics change the transverse resolution, the transverse resolution of the specific system used in each study will be described in each Materials and Methods section.

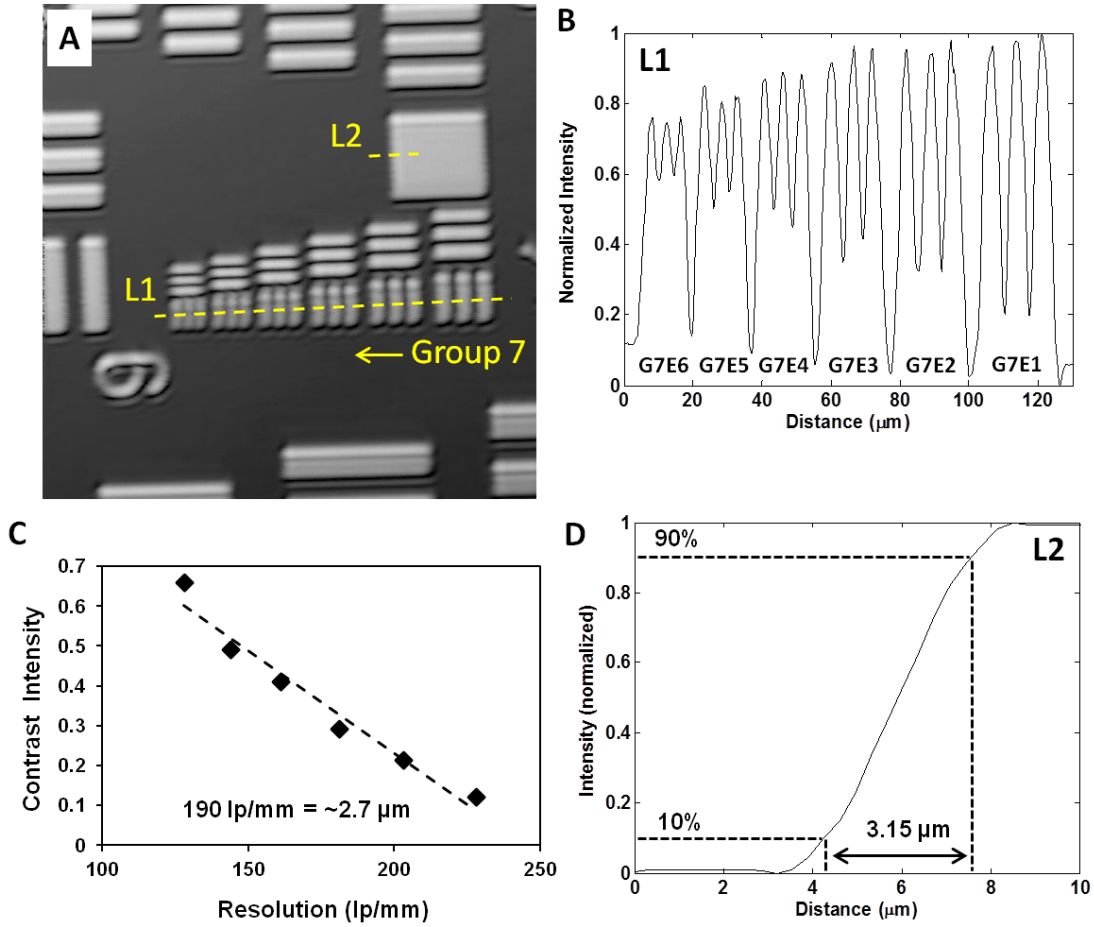

Figure 13. Transverse resolution determined by 1951 USAF resolution chart. (A) 1×1 mm *en face* image of resolution chart. The lowest resolvable element according to contrast is Group 7, Element 4 (G7E4). Group 7 is labeled and Element 1(G7E1) is located above the label on the right side of the image with descending sizes to Element 6 next to the L1 label on the left side of the image. (B) Line plot of L1 line in (A) across all Group 7 (G7) elements. (C) Contrast transfer function (CTF) of Group 7 elements in (A). (D) Line plot of L2 depicting edge spread function (ESF). Distance between normalized intensity at 90% and 10% is identified (arrow).

1.3.4. Sensitivity

Sensitivity is defined as the signal range above the noise level that is detectable. This can be discerned by determining the minimum reflection from a planar surface (e.g.

mirror) that gives rise to a signal matching the noise level. The sensitivity can be referred to as the signal-to-noise ratio (SNR) and can reach values exceeding 100 dB, which is measured on a logarithmic scale. Therefore, it is possible to detect reflected photons from the sample that consist of $1 \cdot 10^{-10}$ of the incident light. The OCT system used in the studies has sensitivity between 92-95 dB.

1.3.5. Phase Stability

Light that interacts with moving reflectors (e.g. red blood cells) undergoes a shift in phase according to the Doppler Effect, much like the siren of a passing ambulance. Detecting phase shifted light depends on the phase stability of the light source and optics. Calibrating the lower limit phase shift can reveal the smallest increment of discernible difference in signal for moving particles. Using a stationary mirror, the fluctuations in phase of back-reflected light can provide a means to approximate the phase stability of the OCT system (see Figure 14). However, fluctuations in phase should be recorded with a scanning beam because the jitter and induced-phase shift from the galvanometer mirrors can affect the phase stability of the light in the sample arm.

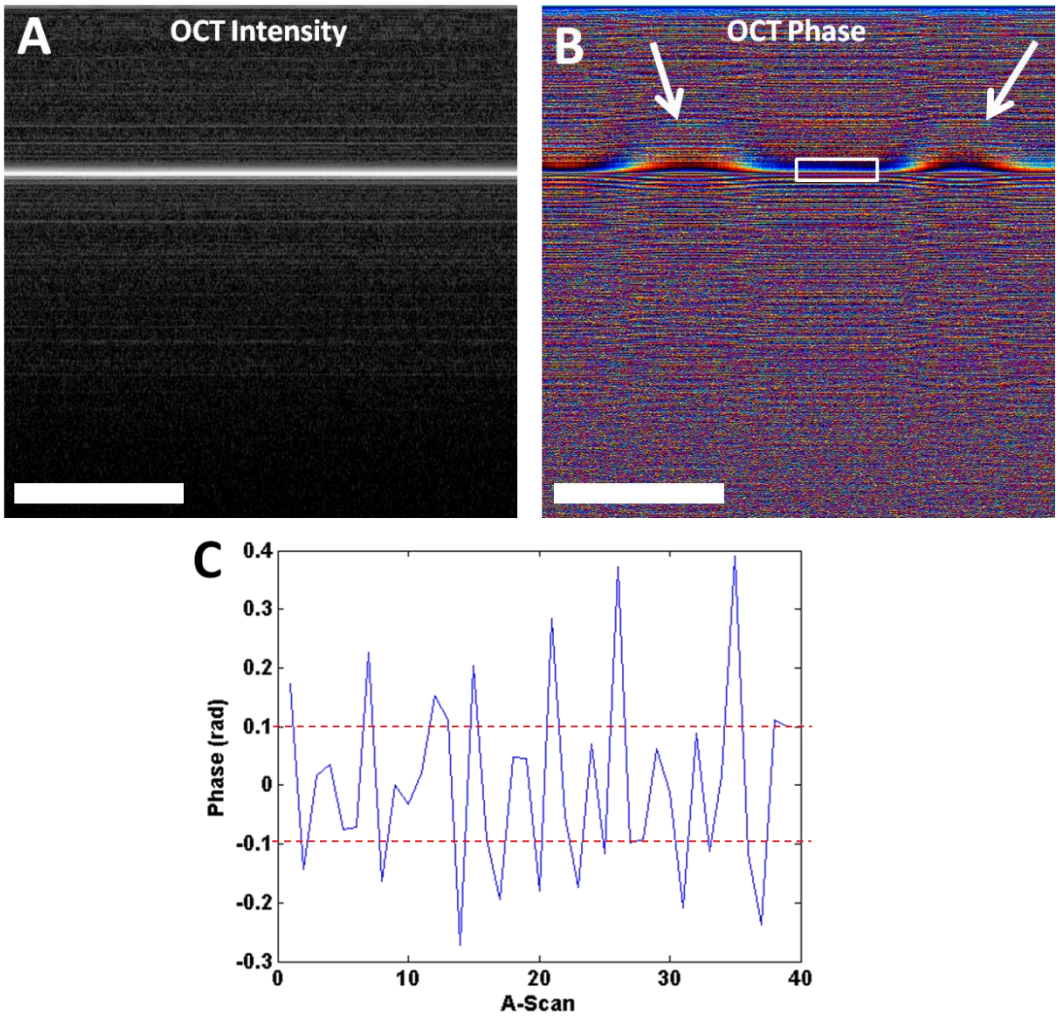

Figure 14. OCT phase stability. (A) OCT intensity and (B) corresponding phase images. Arrows in (B) indicate phase fluctuations that are not displayed in the OCT intensity image (A). (C) Plot of the phase taken from within the region indicated by the white box in (B). Red dashed lines indicate standard error of phase noise. Scale bar = 1 mm.

According to our experimental calibration, the minimum detectable phase shift is ~0.1 rad which corresponds to ~100 μm/s axial velocity (shown in Figure 14C). Improved velocity sensitivity can be attained by using an axial scan gate window (convolution). Using a 5 axial scan window, the minimum detectable phase decreases to ~0.07 rad which corresponds to ~60 μm/s. The gate window and ensemble length

(number of depth points to include in 2D convolution), is inversely proportional to the detectable phase shift. Thus, the larger the gate window and ensemble length is the smaller the phase shift that can be detected.

1.3.6. Advantages of OCT

Technical advantages of OCT as an imaging technology:

1) Reduced radiation exposure compared to alternative imaging with similar scale resolution (e.g. μCT)
2) Relatively low cost, durable, robust, and transportable
3) Higher resolution than US and deeper penetration and faster 3D imaging speeds than confocal microscopy

In clinical medicine, the attractiveness of OCT is encapsulated in the "optical biopsy" which it can provide *in situ*. To be able to visualize biological tissue *in situ* without contact and without tissue excision is something not achievable with other imaging modalities and especially not with conventional core biopsy.

Clinical advantages of OCT as an imaging technology:

1) Image tissue *in situ* where core biopsy is not an option
2) Image tissue in hollow organs using miniaturized, fiber-optic probes
3) Image locations deep within solid organs that are not easily accessible
4) Image in real-time

The backscattered light collected by OCT offers more than only qualitative visualization of tissue structure based on the amplitude of the light; the phase and

polarization of light provides a means to perform quantitative analysis of the light for simultaneous functional imaging. For example, shifts in the polarization state can determine properties of the tissue such as birefringence,[30, 31] and shifts in the phase can reveal blood flow.[32, 33]

1.3.7. Clinical Potential of OCT

Minimally-invasive techniques, such as laparoscopic surgery, have been evolving into a standard of care for urologic surgery by having the benefits of decreased morbidity, shortened hospitalization time, and quicker recovery to full activity compared to open surgery.[34-37] With the positive impact of minimally-invasive procedures, minimally-invasive optical imaging, especially OCT, is expected to play more important roles in clinical kidney imaging. OCT can be readily interfaced with fiber-optic catheters, endoscopes, laparoscopes, and needle imaging probes to image inside the body.[38-41] Minimally-invasive OCT imaging has been demonstrated in the human cardiovascular system,[42] gastrointestinal (GI) tract,[43-46] pulmonary tract,[47] urinary tract,[48] and others, and minimally-invasive Doppler OCT (DOCT) imaging has been demonstrated in the human GI tract,[49, 50] eye,[51-54] and others. Medical imaging technologies, such as US and MRI, have been developed to aid in the diagnosis of acute kidney injury;[55] however, the resolutions of these standard medical imaging systems are limited for they are not able to resolve the fine structures within the kidney nephron (e.g., glomeruli, tubules, vessels). The depth of OCT is shallow compared to other clinical imaging modalities, but the image resolution of OCT is 10 to 100 times greater than conventional US, MRI, or CT. In addition, the imaging depth of OCT is comparable to that typically sampled by core

biopsy and is therefore potentially able to non-invasively evaluate kidney status. Furthermore, OCT is low cost, portable, and ideally suited for surgical suites. Compared to core biopsy, OCT is non-invasive with minimal risk of infection and trauma to the kidney (such as hemorrhage). Also, multiple regions can be surveyed in real time to obtain an overall measure of the kidney's status. Therefore, minimally-invasive OCT holds great potential for diagnosis and management of renal diseases and is the defining motivation for the continuation of research as a biomedical imaging modality.

1.4.Doppler Optical Coherence Tomography

Another advantage of OCT, that is paralleled in ultrasonography, is the ability to detect motion in tissue by analyzing the Doppler phenomenon to calculate velocity.[49, 56, 57] Doppler OCT (DOCT) is a functional extension of OCT that can sense moving scatterers thereby enabling real-time imaging of blood flow in tissue by combining the high spatial resolution of OCT with the high sensitivity of the Doppler effect.[50, 58-62] Velocity information obtained from DOCT has been used to measure microvascular blood flow velocities non-invasively in the human retina,[63-67] skin,[58, 68, 69] brain,[62, 70] and gastrointestinal tract,[50, 71] among others. Moving reflectors within the tissue induce a Doppler frequency shift in the backscattered light, which when combined with the reference beam, is detected as a complex signal, denoting signal magnitude and phase. A change in the complex signal from the interference pattern indicates a phase shift from the sample signal. Positive phase shifts and negative phase shifts can be color-coded in order to identify the direction of motion with respect to the scanning beam. Color-coded DOCT images can then be overlaid on the OCT structural images to provide a powerful

visualization imaging modality of moving scatterers in real time, such as red blood cells *in vivo*.

1.4.1. Principle and Calculation of Doppler Velocity

OCT fringe data contains both magnitude and phase information from the interference pattern created by the combination of the backscattered light from the sample arm with the reference arm. Using the phase information contained in the complex portion of the OCT signal, the Doppler frequency shift at each depth position can be computed. Given that the OCT complex signal (S) can be expressed as:

$$S = I + jQ \tag{5}$$

where I is the real component and Q is the imaginary component. Acquired 2D OCT images can then be stored as complex arrays $I_{m,n}$ and $Q_{m,n}$ with m and n denoting the indices in the depth and lateral dimensions, respectively. OCT intensity images concern only the magnitude of the backscattered light at each particular pixel. The magnitude of the light reflectivity at any particular pixel can be calculated as:

$$\left\langle S^2 \right\rangle = \frac{1}{MN} \sum_{m=1}^{M} \sum_{n=1}^{N} \left[I_{m,n}^2 + Q_{m,n}^2 \right] \tag{6}$$

Where M and N define a specified averaging window. M is the depth of the window (also known as the gate length), and N is the number of axial scans to include (also called the ensemble length). The averaging window performs a type of convolution of the image improving the signal-to-noise ratio but also lowering the resolution. Since OCT intensity images contain a large dynamic range, the logarithm of the intensity of the

backscattered light is used to display OCT structural images.

The Doppler frequency shift associated with the structural OCT image can be computed from the corresponding complex component of the signal at each pixel according to the Kasai autocorrelation equation[72]:

$$\langle v \rangle = \frac{\lambda_0 f_D}{2 n_t \cos(\theta)} \tag{7}$$

$$f_D = \frac{f_a}{2\pi} \left\{ \frac{\frac{1}{M(N-1)} \sum_{m=1}^{M} \sum_{n=1}^{N-1} \left(I_{m,n+1} Q_{m,n} - I_{m,n} Q_{m,n+1} \right)}{\frac{1}{M(N-1)} \sum_{m=1}^{M} \sum_{n=1}^{N-1} \left(Q_{m,n+1} Q_{m,n} - I_{m,n+1} I_{m,n} \right)} \right\} \tag{8}$$

where v is the mean velocity, λ_0 is the center wavelength of the light source, f_D is the Doppler frequency shift, n_t is the tissue index of refraction (~1.33), θ is the direction angle of the moving scatterer, f_a is the axial scanning frequency of the beam. Computing the mean shift between adjacent axial scans using the arctangent function means that the Doppler frequency shift (f_D) is defined in all four quadrants but has output values only ranging from $-\pi$ to $+\pi$. The value of M and N for DOCT are typically not the same as for OCT. Increasing the averaging window size can help improve the signal-to-noise ratio but at the consequence of lower resolution. But, if high noise levels are present in the DOCT images, increasing the averaging window can smooth out minor artifacts.

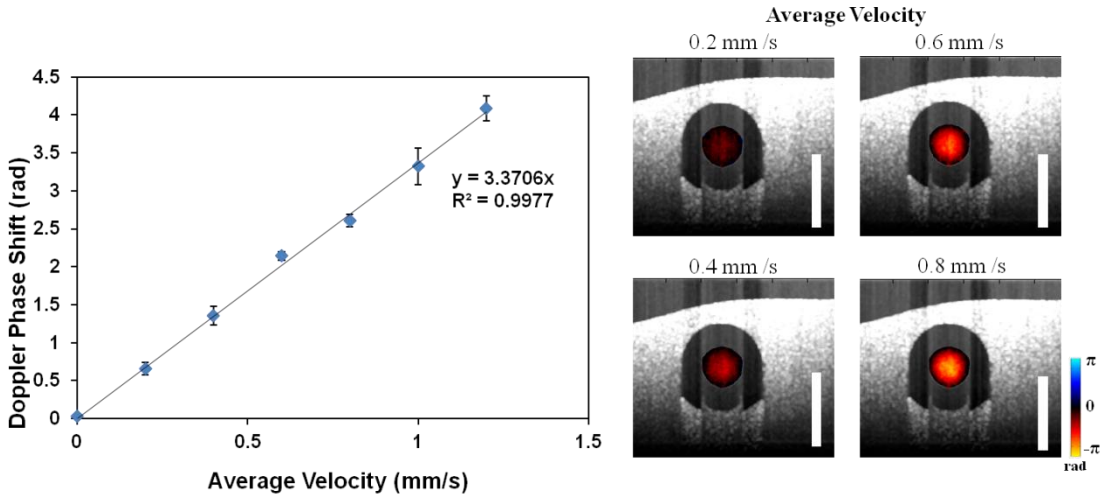

Figure 15. DOCT calibration using tube phantoms with intralipid (IL). IL was pumped through capillary tube at defined velocity intervals using syringe pump. Scale bar = 1 mm.

1.4.2. Detection Limits of DOCT

The detectable Doppler velocity range is defined according to the minimum and maximum non-aliased velocities that are dependent upon the scanning beam frequency and the phase stability of the interferometer and optoelectronics. The maximum DOCT velocity range is defined as:

$$V_{\max} = \frac{\lambda_0 f_a}{2n_t} \tag{9}$$

with λ_0 = 1310 nm, f_a equal to 8.0 kHz, and n_t equal to 1.33 for tissue, the maximum non-aliased velocity achievable with our system is 3.91 mm/s. Velocities exceeding this value will be aliased from discontinuities in accordance with the limits of the arctangent function. In principle, higher velocities can be achieved by "unwrapping" the aliased discontinuities in the phase, but it become increasingly challenging in the presence of

noise. However, there is an upper limit to phase unwrapping techniques since the velocity estimation accuracy of the phase-resolved method diminishes with increasing flow velocity.

The minimum detectable velocity is dependent on the phase stability of the system, which forms a basement noise level. The minimum velocity value is defined as:

$$V_{\min} = \frac{\lambda_0 f_a}{2n_t} \cdot \frac{\Delta\phi}{2\pi} \qquad (10)$$

with λ_0 = 1310 nm, f_a equal to 8.0 kHz, n_t equal to 1.33 for tissue, and $\Delta\varphi$ equal to 0.9 rad (see Figure 14C, standard error value), the minimum detectable velocity with our system is ±53 μm/s. This agrees with published values of the phase noise for our OCT system.[73] The minimum detectable velocity is relatively fixed according to the performance of the system's hardware (optic and electronic components). Improving the stability of the laser source could be a way to lower the minimum detectable velocity of the system.

1.4.3. Determination of Flow with DOCT

In order to quantify blood flow, several algorithms have been published but most are dependent upon the angle between the directional flow vector and the scanning beam.[54, 74] Recently, however, an algorithm quantifying flow rate independent of the velocity vector orientation was published which demonstrated the ability to integrate the velocity profile of a bisected vessel in order to obtain its total flow rate.[75] Flow can be calculated by integrating over the *en face* (lateral plane) image to eliminate the angle dependence of the Doppler phase shift (see Figure 16).

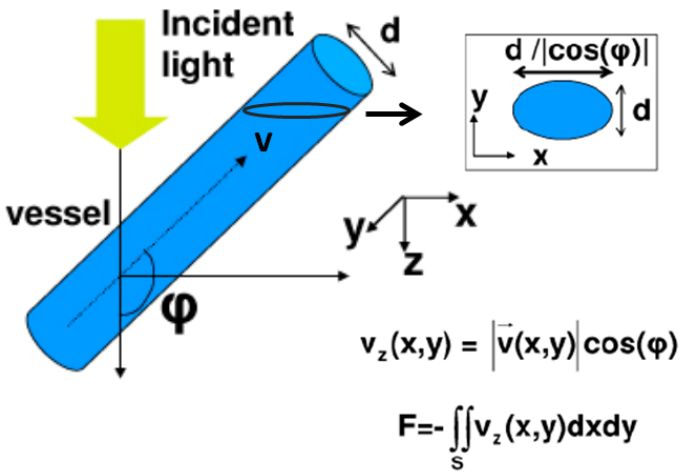

Figure 16. Calculation of flow from DOCT velocity. Integrating over the *en face* lateral cross-section cancels the cosine angle dependence of the vertical velocity measurement. Diagram from Srinivasan, et al. Opt. Express, 18, 2010.[75]

Therefore, to validate our DOCT imaging system we quantified the flow rate in several tube phantoms. By performing 3D DOCT imaging on the tube phantoms with a constant (known) flow rate, the measured flow rate from the DOCT images was compared with the specified flow rate value. Figure 17A displays the results of these comparisons. The set flow rate in the tube phantom was 0.1702 μl/s and the value obtained from integrating over the lumen of the tube phantom in three separate trials was 0.1728 ± 0.0031 μl/s. Figure 17B,C,D display *en face* images of the capillary tube at varying angles (with respect to the vertical axis). Different vertical angles will change the vertical component of the fluid velocity in the tube thereby yielding different DOCT phase shifts. The vertical velocity represented by the intensity of the red/yellow color shows decreasing intensity (Figure 17B compared to Figure 17C,D) when increasing the angle away from the vertical axis (i.e. making the tube direction more horizontal). But by integrating over the *en face* lateral cross-section of the tube, the flow calculation is not

dependent on the tube orientation direction.

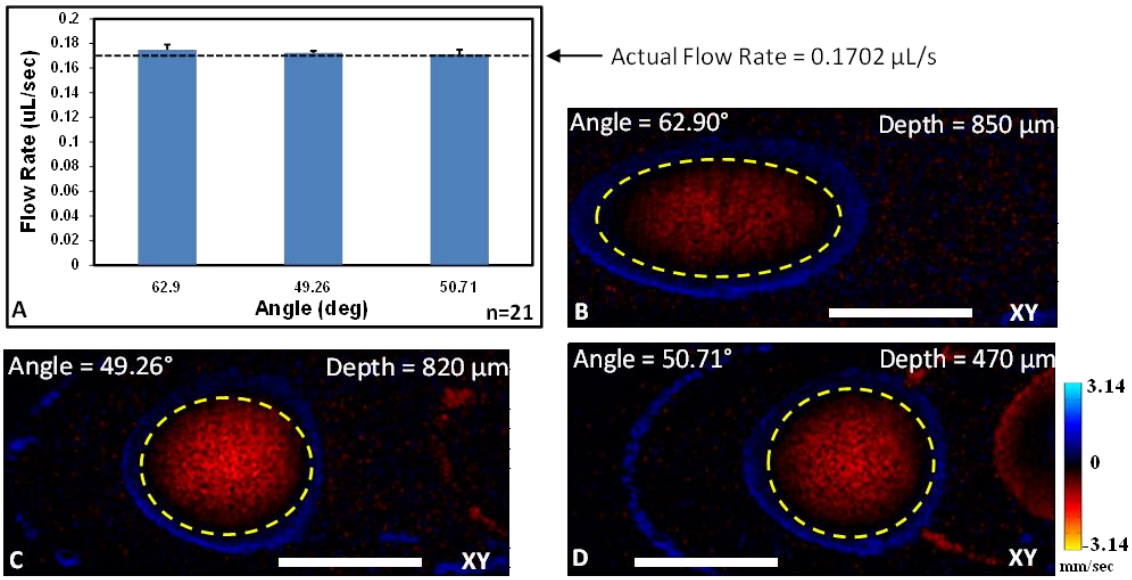

Figure 17. DOCT flow rate calibration using capillary tubes and scattering media. (A) Flow rate computed from DOCT *en face* velocity map images. Actual flow rate indicated by horizontal dashed line. (B-D) DOCT *en face* velocity map images with specified tube angle and depth. The flow rate presented in (A) was obtained from (B-D) by integrating the velocity within lumen of tube phantom (enclosed by yellow dashed line). DOCT colormap indicates positive vertical velocity (red/yellow) and negative vertical velocity (blue/cyan). Scale bar = 500 µm.

Examples of the *en face* lateral cross-section velocity profile can be seen in Figure 17B-D which shows the vertical velocity map across the plane of the tube at a specific depth. Our calibration results agree closely with the set flow rate in the tubes demonstrating the accuracy of calculating flow from 3D DOCT *en face* images.

2. Background on the Clinical Application

2.1.The Renal System

Metabolic waste is a natural by-product of cellular function and must be efficiently excreted in order to not retain toxic compounds in the body. Waste products of primary importance are urea and uric acid, which are waste molecules from protein metabolism and nucleic acid breakdown. But, just as significant as the need to rid the body of urea and uric acid is the need to maintain electrolytic homeostasis by regulating the body's water and inorganic salt content. A deficiency in the body's general ability to excrete waste products results in life-threatening conditions, such as metabolic acidosis, hyperkalemia (elevated blood potassium levels), and uremia (elevated blood urea levels). In addition to filtering and excreting metabolic waste products and balancing the body's internal environment, the renal system also functions to control blood pressure, intravascular volume, and stimulate the production of red blood cells in the bone marrow by secreting the hormone erythropoietin.[76, 77]

Waste products produced within the body are transported to the renal system via the blood through the circulatory system. The kidney is the organ in the renal system that performs the filtration of the blood and collection of urine, which it then simply passes to the urinary bladder for storage through the ureter.

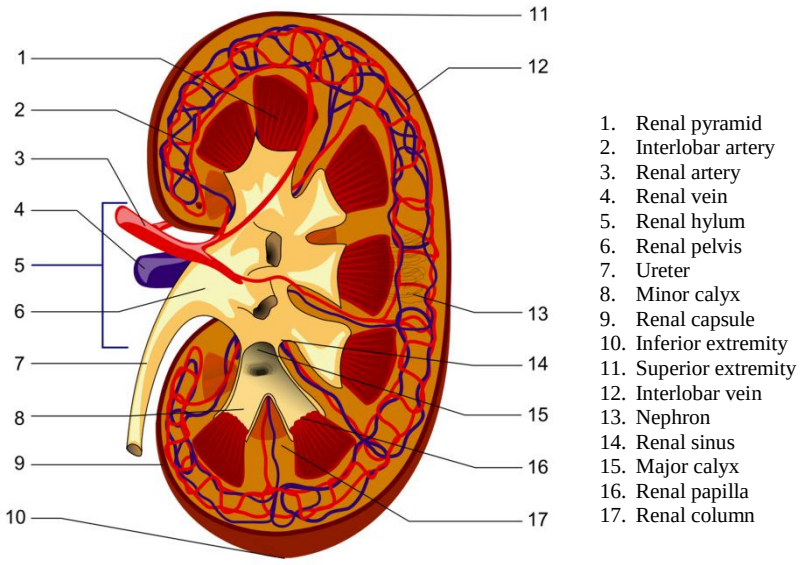

Figure 18. Frontal section of the human kidney. Major structures such as the medulla, cortex, and major calyx can be seen as well as the overall anatomy of the organ. Used by permission.[78]

Figure 18 shows the gross anatomy of the kidney with the major anatomical features labeled. However, the disposal of waste products in the blood takes place on the microscopic level in subunits of the kidney called nephrons (see Figure 19).

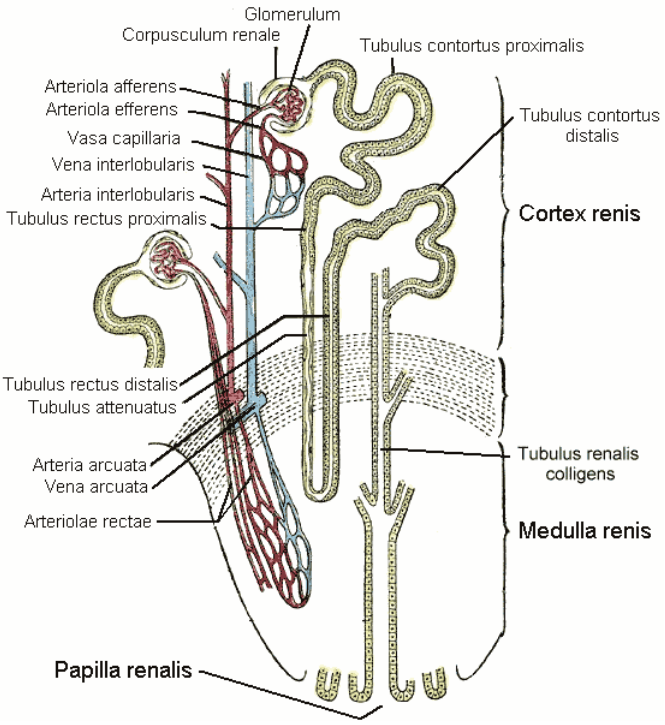

Figure 19. Kidney nephron. Major components are identified with the numbered labels that correspond to the list on the right. Used by permission.[79]

The component of the nephron that does the actual filtering of the blood, though, is the glomerulus (#6 in Figure 19), which contains a bed of fenestrated capillaries allowing the rapid transport of water and other small solutes out of the blood and into the Bowman's space (see Figure 20).[80]

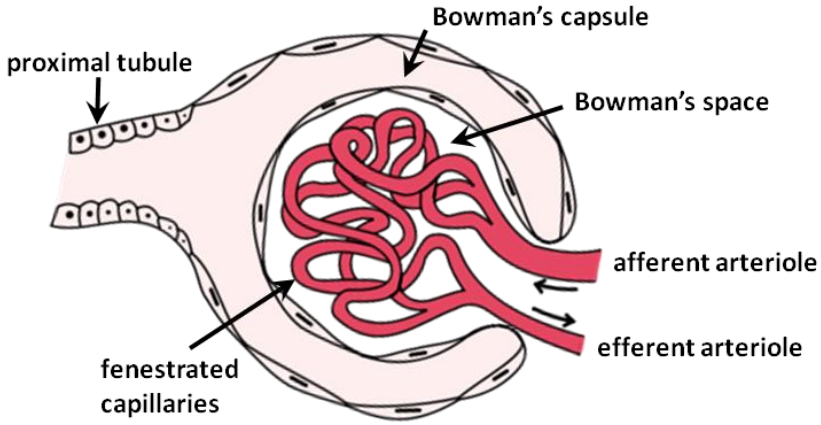

Figure 20. Kidney glomerulus (filtering component in the nephron). Glomeruli consist of a ball ("tuft") of intertwined capillaries that seep plasma, ions, small proteins, and waste molecules out of the blood into the Bowman's space, which is subsequently drained into the proximal tubule. Used by permission.[79]

Of paramount importance in the ability of the kidney to perform proper filtration is the amount of blood flowing to the glomerulus and the rate at which waste products are filtered out of the blood by the glomerulus. Any substantial decline in either of these parameters would directly impair the ability of the kidney to effectively filter the blood.

Several disease states can result in altered renal blood flow (RBF) and changes in shape and size of kidney microstructures. For example, during renal surgery, injury to the kidney can result from ischemia (deprivation of blood/oxygen), which then, in turn, can result in some degree of renal dysfunction, or during kidney transplantation, if the transplanted kidney experiences reperfusion injury, this can result in altered blood and subsequently delayed graft function of the donor kidney. Also, in the transition from normal parenchyma (kidney tissue) to cancerous tissue, renal tissue undergoes

architectural changes that affect the shape, size, density, and general constituents of the tissue. For example, renal cancer disrupts the homogenous renal parenchyma that is observed in health, normal renal tissue (see Figure 21). Uriniferous tubules are regularly dispersed (small circular, dark spots beneath bright surface layer) but in the tumor region, aberrant tissue architecture (heterogeneous tissue patterns) is seen and highly disorganized tubular networks (erratic dark tubes and spots beneath the surface).

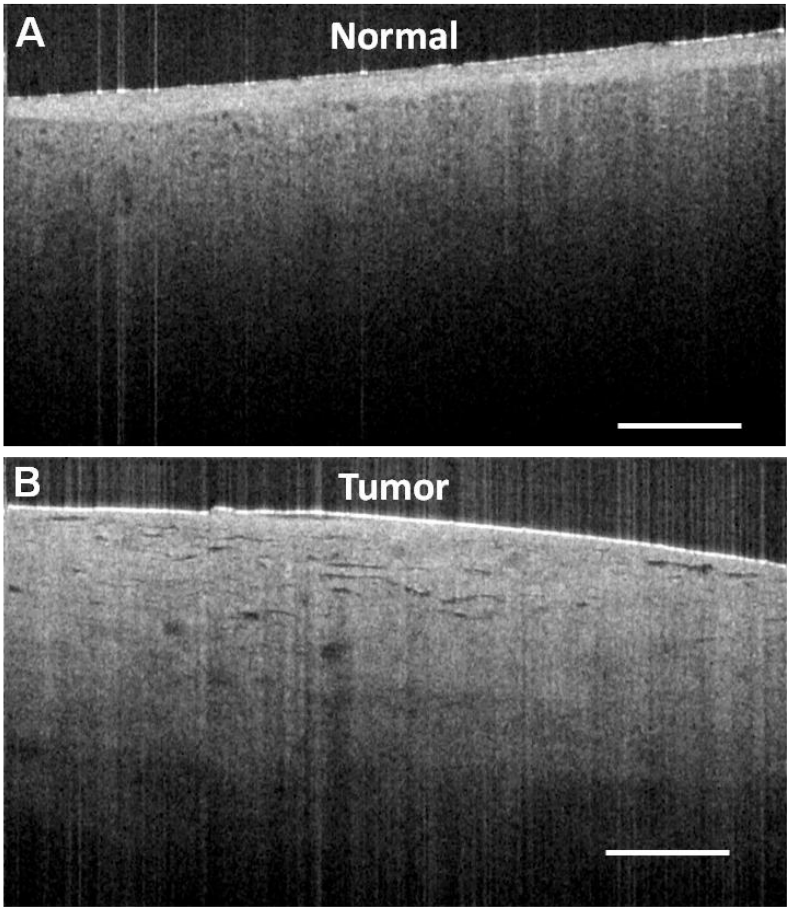

Figure 21. Normal versus cancerous *ex vivo* kidney tissue. (A) Normal tissue exhibits clear capsule and relatively uniform parenchyma with densely packed uriniferous tubules (small dark circles). (B) Renal cancer tissue exhibits generally disorganized tissue architecture with aberrant tubular structures unevenly distributed throughout with no discernible capsule on the kidney surface. Scale bar = 500 μm.

Therefore, in order to identify injury caused by renal ischemia and minimize the risk of delayed graft function, or to distinguish cancerous tissue from normal renal tissue, imaging of kidney microstructure and blood flow can provide critical parameters that can gauge the status and function of the kidney and identify cancer regions, which is vital to know in order to provide optimal patient treatment during renal surgery.

3. Rat Kidney Blood Flow Imaging

3.1.Introduction

Intrarenal hemodynamic abnormalities are thought to be a primary factor associated with the onset and progression of acute injury,[81] and other various nephropathies like diabetic nephropathy,[82, 83] and focal segmental glomerulosclerosis.[84] Real-time assessment of renal morphological and hemodynamic changes could help to evaluate the kidney condition and offer valuable information to predict the prognosis of injury or disease lending to the development of patient-specific management strategies. Currently, though, there is no sensitive and objective tool for direct monitoring of renal microcirculatory changes in the clinic. The ability to monitor alterations in renal microcirculation due to vascular or glomerular disease may improve diagnostic and therapeutic interventions for renal health care.

Renal blood flow (RBF) has been monitored using a number of different imaging modalities including positron emission tomography (PET),[85-90] and magnetic resonance angiography,[91-94] Doppler ultrasound (US),[95-98] and contrast-enhanced (CE) US.[99, 100] While these techniques allow for non-invasive, wide field-of-view imaging, they do not have sufficient resolution to detect changes in renal microcirculation (glomerular). Regarding kidney transplantation, studies have suggested that blood perfusion within glomerular capillaries may be correlated with intermediate and long-term graft function.[101, 102] Therefore, immediate detection of microcirculatory changes could provide decisive criteria for therapeutic interventions promoting graft salvage and long-term

function.[102-104]

Optical imaging techniques, though, that have higher resolutions and greater sensitivities could be a more feasible method for monitoring and evaluating microcirculatory changes, especially in an intra-operative setting. Several optical imaging techniques have been employed to study RBF. Studies using confocal[105-107] and multi-photon microscopy[108-110] have demonstrated the ability to image kidney microstructure and function (blood flow and filtration rate) on animal models, but the penetration depth has been limited to several hundreds of microns,[111] and they require the need to administer contrast agents to determine flow. Therefore, using these imaging modalities for human studies poses certain challenges due to the capsule surrounding the human kidney, which can be several hundred microns thick, and the need to inject contrast agents into the patient.

Optical coherence tomography (OCT)[23] and its functional extension Doppler OCT (DOCT)[68] are emerging imaging technologies that have the capacity to provide real-time images (i.e., immediate imaging) of tissue in a non-invasive fashion (i.e., a non-destructively) with high-resolution near that of conventional histopathological images. Previous studies by us have demonstrated the ability of OCT to resolve the renal corpuscle and uriniferous tubules[112] and evaluate the real-time morphological changes in these structures associated with ischemia-reperfusion injury *in vivo*.[113] Also, we have previously demonstrated that OCT can penetrate the kidney capsule surrounding human kidneys thereby enabling the characterization of renal tubules, glomeruli, and cortical blood vessels in fixed human kidneys.[114, 115] OCT represents a laser echo microscopy and

has the potential to become a powerful tool for functional renal evaluation in the near future.[116]

High-speed, Fourier-domain DOCT can be used to visualize blood flow non-invasively by measuring Doppler frequency shifts in the OCT interference signal caused by moving scatterers that are label-free, such as red blood cells.[117] DOCT has been used to image and quantify blood flow *in vivo* for multiple clinical applications including retina,[51, 118-120] skin,[121-123] and gastrointestinal tract,[124] among others. Thus, DOCT imaging of kidney blood flow has demonstrated translational potential.

In the present study, our objective was to demonstrate the feasibility of using Doppler OCT (DOCT) to observe microcirculation within the living kidney in real time and quantitatively compare physiologically induced changes.

3.2.Material and Methods

3.2.1. Optical Coherence Tomography (OCT) and Doppler OCT

A high-speed, high-resolution OCT system was used in this study. The details of the OCT system have been previously described.[114] Briefly, a Fourier-domain OCT system consisting of a swept-source laser with 100 nm bandwidth at 1310 nm center wavelength yielding an axial resolution of ~12 μm in tissue was used. A 10x objective (Olympus Plan N, NA=0.25) was used in the sample arm to achieve a lateral resolution of ~2-3 μm determined by USAF resolution target. The laser source operated at a sweep rate of 16 kHz allowing a series of 2D cross-sectional images to be captured in real time to form a 3D data set (Voxel size: 1024 [X] by 256 [Y] by 512 [Z]; Dimension: 0.280 mm

[X] by 0.325 mm [Y] by 1.90 mm [Z]; acquisition time <20 sec). OCT fringe data was acquired to obtain both amplitude and phase information after Fourier transform, and Doppler OCT signals were computed using standard phased-resolved algorithm.[117]

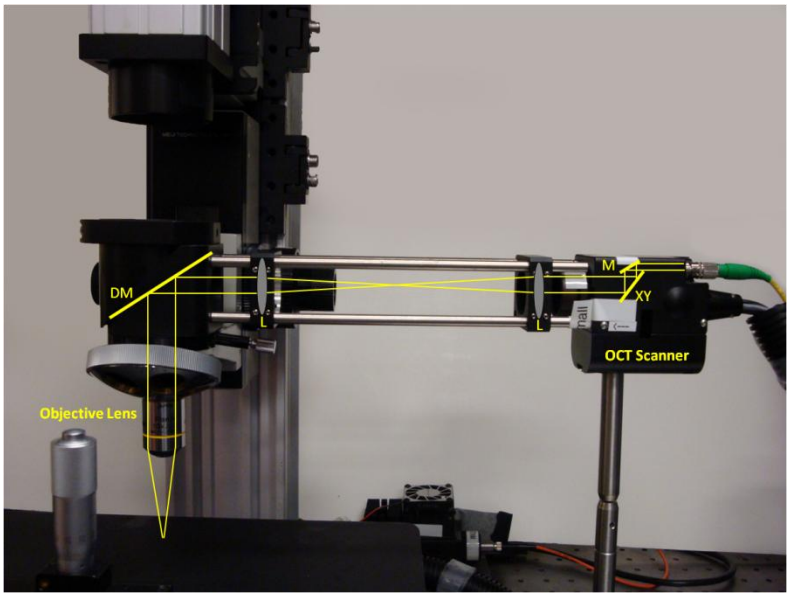

Figure 22. OCT/DOCT Microscope Setup. Abbreviations: XY: galvonometer; M: mirror; DM: dichroic mirror; L: lens.

3.2.2. Animal Model and Experimental Setup

The animal protocol has been approved by the committees on animal care and use in both the University of Maryland and Georgetown University. Male Munich-Wistar rats (n=3, ~400 g) were used in this study. This strain of rat has numerous superficial glomeruli in the outer cortex that are accessible for observation.[125] Rats were regularly fed normal rat chow with free access to water at all times. During the study, rats were anesthetized by intraperitoneal injection of pentobarbital sodium (100 mg/kg body weight) and monitored routinely by tactile stimulation with supplemental anesthetic added as needed to maintain initial depth of anesthesia. After being secured on a portable

surgical apparatus, the left kidney was exposed through laparotomy of the left flank region and the kidney was securely placed in a lucite holder. The right femoral vein was then cannulated with polyethylene tubing for administration of pharmacologic agents. Rats were then placed beneath the DOCT microscope for *in vivo* imaging. To induce alterations in renal blood flow, 0.1-0.2 ml mannitol (250 mg/ml), which increases renal blood flow,[126-128] and 200ng/kg body weight angiotensin II,[129] which decreases renal blood flow,[130-133] were administered by a bolus injection into the femoral vein. Three injections of mannitol at ~45 min intervals were performed followed by DOCT imaging after each injection and then a final injection of angiotensin II was given 10 min after the third mannitol injection and then followed by DOCT imaging. DOCT imaging was also performed approximately 15-20 min after each infusion of mannitol when the physiologic effects of the drug were diminishing. Data taken during this period is labeled "recover" to distinguish it from the data taken immediately after each mannitol injection. At each stage, multiple glomeruli ($n \geq 3$) from different locations were imaged. Thus, the same glomeruli were not re-imaged at each stage due to the fact that multiple glomeruli were located and imaged at each stage by surveying different regions of the kidney cortex.

3.2.3. OCT/DOCT Image Processing and Quantification

Glomeruli were located by scanning the surface of the cortex, and 3D data sets, including the fringe data for Doppler analysis, were acquired for each glomerulus (total n=44). OCT intensity images as well as DOCT images were computed from the fringe data for each frame in the 3D data sets.[134] DOCT images were computed using a 5×5 binning window (gate length = 5, ensemble length = 5). To display the spatial correlation

between the OCT and DOCT images, OCT/DOCT fused images were constructed where the DOCT color images were overlaid on the grayscale OCT intensity images using a transparency mask based on a DOCT threshold that eliminated the background leaving only the higher DOCT signals opaque. Quantification of single glomerular microcirculation parameters was performed offline using a custom image analysis program written in Matlab (Mathworks Inc., Natick, MA, USA) by our lab. Algorithm for quantification parameter is given after explanation (see Figure 24).

The glomerular volume (GV) was computed from the OCT intensity image according to the equation:

$$GV = \frac{2}{3} S_A h \tag{11}$$

where S_A is the surface area through the mid-section of the glomerulus and h is the height of the glomerulus. The surface area and height of each glomerulus was manually selected by encircling the perimeter of the glomerulus in cross-sectional and *en face* images passing through the center of glomerulus. The *2/3* scaling factor converts the cylindrical geometry, which is initially computed from the height and radius of the glomerular boundary that is manually selected for each data set, to the more realistic elliptical or spherical geometry of glomeruli.

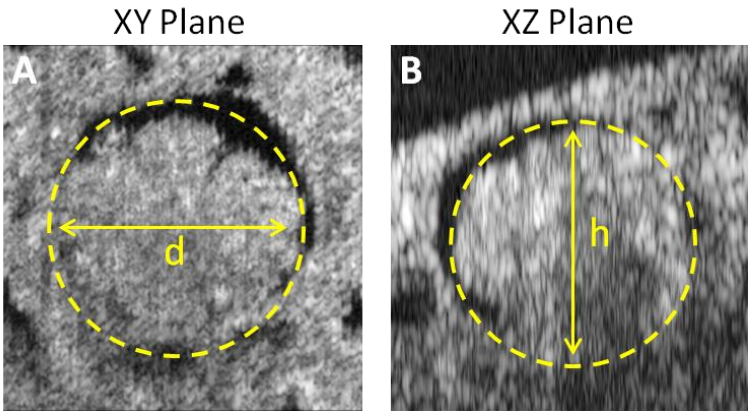

Figure 23. Manual selection of glomerular boundary. (A) XY plane (*en face*) image showing top-down view of glomerulus transverse mid-section. Diameter (d) is defined as indicated by arrow. Lateral cross-section surface area is subsequently computed from the diameter. (B) XZ plane image showing side-view of glomerulus vertical cross-section. Height of glomerulus is defined as indicated by arrow. Image size: 294 × 278 μm.

All 3D DOCT data were subsequently analyzed by computing cumulative Doppler volume and Doppler flow range parameters. The cumulative Doppler volume (CDV) was calculated by summing together the volume of segmented voxels within the glomerular volume containing DOCT signals that were above the background threshold as defined below in Equation 12, where *V(x,y,z)* is individual voxel volume.

$$\mathrm{CDV} = \sum_{xyz} \mathrm{V(x,\ y,z)} \qquad (12)$$

The threshold value ($|v_z|$ = 0.05 mm/s) for computing CDV was set to slightly above the average DOCT signal from regions of static tissue. The CDV is not equivalent to "Blood Volume" as DOCT is only sensitive to scatterers (red blood cells). Therefore, the CDV we measured is expected to be smaller than actual "Blood Volume" and is coupled with the level of hematocrit.

Doppler flow range (DFR) was defined as the flow rate at 90% area under the curve (AUC) of the 3D flow histogram. The omission of the last 10% was to reduce variability from outliers in the histogram that would significantly alter the flow range determination. 3D flow histograms were calculated by integrating the DOCT signal over the lateral cross-section (*en face*) area of the segmented capillaries within the glomerular volume at each depth position (XY frame) for a single glomerulus and then sorting them according to a consistent bin size. Integration over the *en face* plane eliminates the angle-dependent uncertainty of the Doppler velocity therefore providing an accurate quantitation of flow as defined in Equation 13 below.[75] Doppler flow calculations were performed in *en face* images according to Equation 13, where $v_z(x,y,z)$ is the segmented DOCT velocity according to a threshold of 0.05 mm/s integrated over the *xy* segmented DOCT area.

$$\text{Flow} = \iint_{xy} \mathrm{v}_z(x, y, z)\,dxdy \tag{13}$$

A graphical representation of the cumulative Doppler volume and Doppler flow calculations is depicted below in Figure 24.

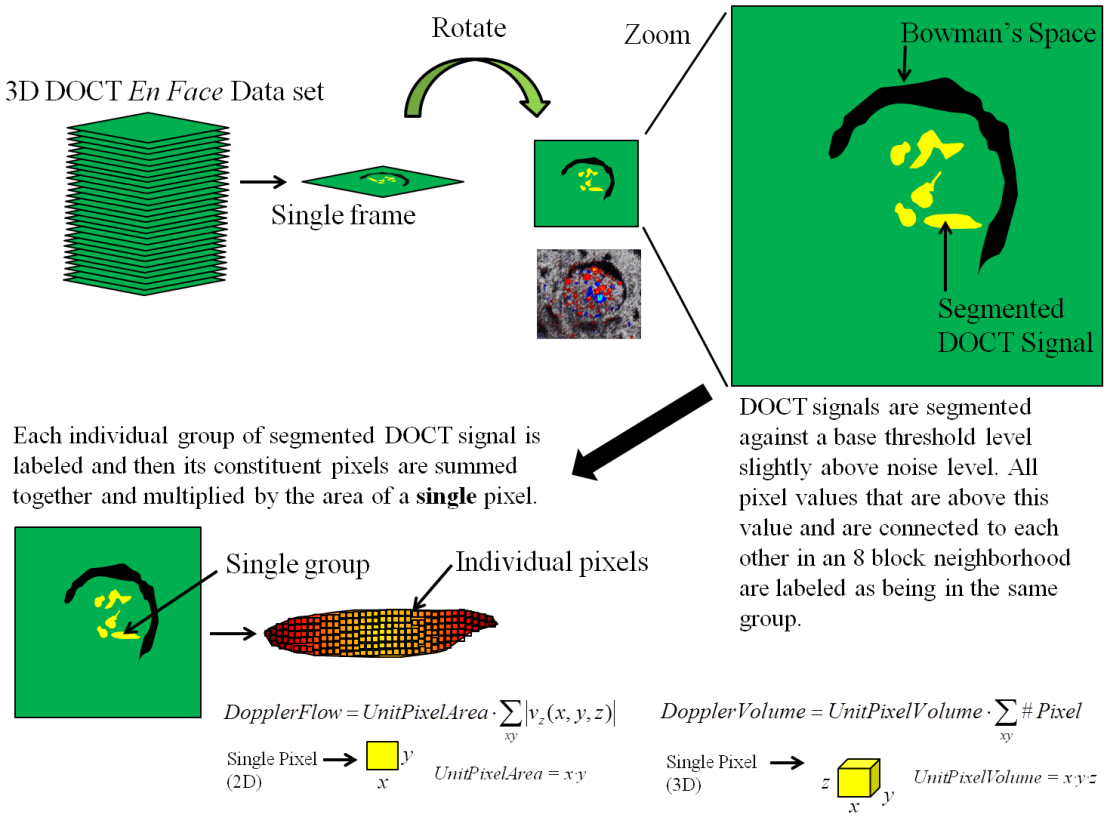

Figure 24. Flow chart describing CDV and Doppler flow calculations.

The illustration in Figure 24 depicts selecting only one *en face* frame and details the quantitative computations for only a single group within that frame. However, in the data analysis, cumulative Doppler volume (CDV) and Doppler flow range (DFR) calculations were performed on all segmented groups in all frames that were within the glomerular volume. The glomerular volume region is defined as the space surrounded by the capsule of Bowman, which was manually selected for each data set in the lateral (xy) and cross-sectional (xz) dimensions.

3.2.4. Statistical Analysis

Data is given as mean ± standard deviation. One-way ANOVA test was

performed to evaluate sampling variance followed by Tukey's multiple comparison test with respect to the "baseline" values to determine statistical significance ($p < 0.05$ were considered significant). All histograms were computed using consistent bin size of 5×10^{-6} µl/s and minimum threshold equal to 0.05 mm/s.

3.3.Results

After the rat left kidney was exposed beneath the microscope, several glomeruli were located by scanning the beam across the surface of the kidney. 3D data sets of glomeruli were acquired and stored for subsequent analysis. With PIP (picture-in-picture) mode enabling simultaneous OCT/DOCT on-screen viewing, we were able to see blood flow in each glomerulus in real time while scanning the surface of the kidney. OCT/DOCT fused images were constructed offline to verify the spatial correlation of the captured DOCT signal. OCT/DOCT imaging of kidney glomerulus revealed intra-glomerular blood flow from the internal capillary network.

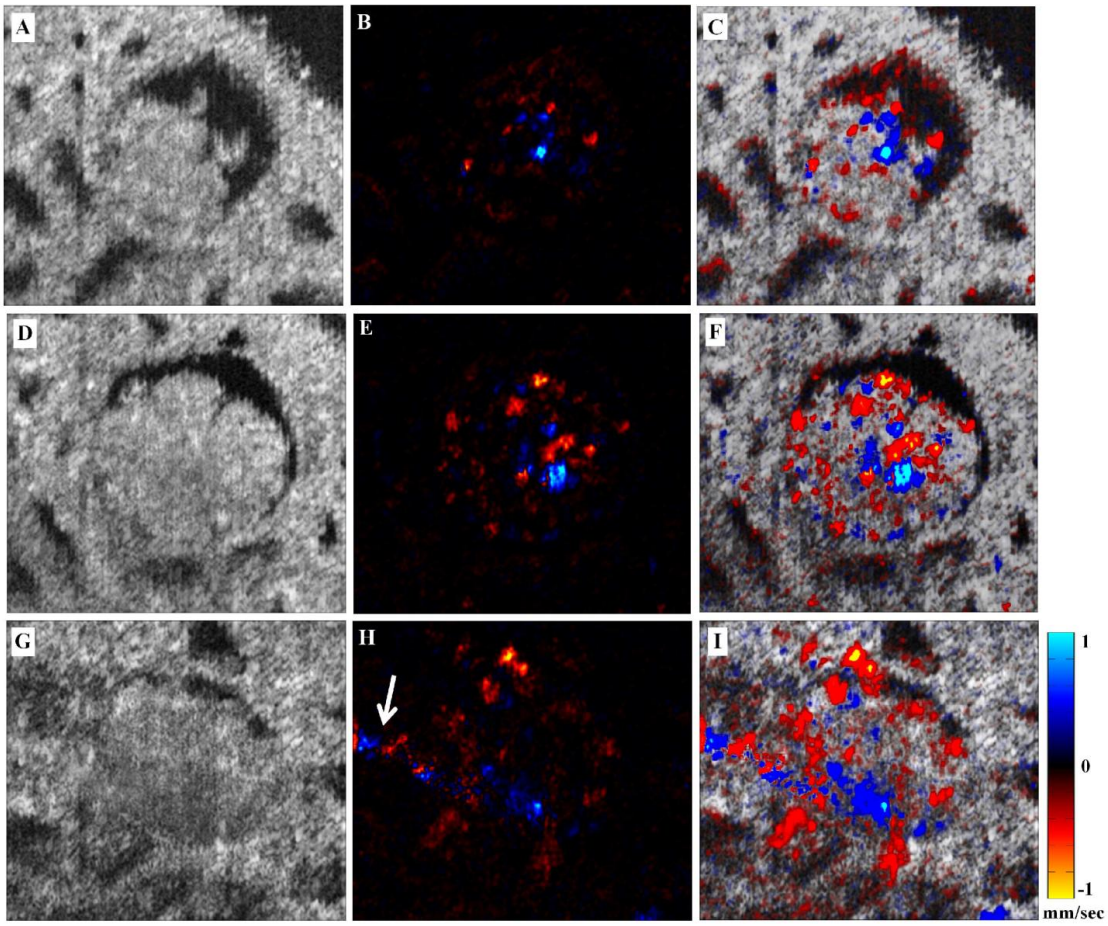

Figure 25. OCT and DOCT imaging of rat glomerulus. (A,D,G) OCT *en face* view of single glomerulus. (B,E,H) DOCT *en face* view of the same glomerulus. (C,F,I) Fused OCT/DOCT image showing spatial agreement between the OCT image and the corresponding DOCT image. The three images in each row correspond to the same imaging plane in depth. Depth (A-C) = 440 μm; (B-F) = 470 μm; (G-I) = 545 μm. Arrow in (H) identifies arteriole extending away from glomerular body. Image size: 325 × 278 μm.

Figure 25 shows images of three *en face* planes at different depths in a representative glomerulus: the top row is the upper region (A-C), the middle row is the middle region (B-F), and the bottom row is the lower region (G-I). Figure 25A,D,G show OCT intensity images revealing the kidney microstructure. Numerous uriniferous tubules (dark, pill-shaped features) can be seen surrounding the glomerulus, which is the circular

structure in the middle of the image surrounded by the dark, crescent shaped capsular space of Bowman. Figure 25B,E,H show corresponding DOCT images from the same plane depicting red blood cell velocity in numerous glomerular capillaries. As indicated by the colormap scale, red to yellow represents increasing velocity of blood flow in one direction while blue to cyan represents increasing velocity of blood flow in the opposite direction. Therefore, the mixture of these colors seen in the DOCT images demonstrates the varying velocities as well as the convoluted nature of blood flow through the glomerular capillaries. Figure 25C,F,I are the fused OCT/DOCT images demonstrating the spatial correlation of the DOCT signal within the glomerulus seen in the OCT images. Three-dimensional (3D) *en face* OCT/DOCT images sectioning through the entire glomerular volume can demonstrate the interwoven and tortuous nature of the glomerular capillary bed. DOCT is also able to reveal the vascular pole (where the blood enters/leaves the glomerulus) showing the afferent or efferent arteriole (Figure 25H, arrow). Note that this imaging information is not readily apparent in the corresponding OCT structure image. Figure 26A shows a top-down view of the complete 3D DOCT signal captured from the glomerulus in Figure 25 where the vascular pole with an arteriole connecting to the glomerular capillaries can be identified (arrow). Figure 26B offers a 3D perspective of the OCT/DOCT signal from the same glomerulus. The grayscale colormap represents the segmented OCT structural image showing the renal tubules and Bowman's space, and the red/blue colormap represents the DOCT signal. Beneath the broad, gray, umbrella-like structure (Bowman's space) is the glomerulus interior where numerous DOCT signals nest together representing the blood flow in capillary tufts.

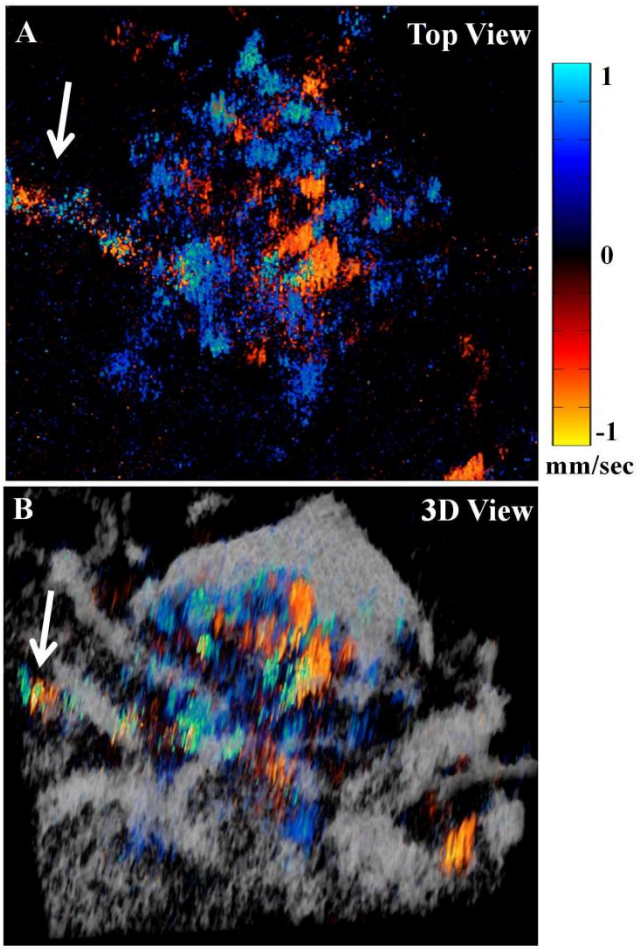

Figure 26. (A) Top-down (vertical projection) view showing numerous clustered DOCT signals within the glomerulus representing red blood cell velocities. Image size: 325 × 278 μm. (B) Three-dimensional (3D) rendering of the 3D OCT/DOCT data set of the glomerulus in Figure 25 reconstructed from a series of cross-sectional images. Grayscale colormap represents segmented kidney microstructures from OCT and red-blue colormap represents bi-directional blood velocity from DOCT. Volume size: 325 × 278 × 580 μm.

In vivo DOCT imaging was performed during three separate physiological states: baseline, following injection of mannitol, and following injection of angiotensin II. Figure 27 shows representative glomeruli imaged under each condition. Baseline DOCT is depicted in Figure 27B with mannitol and angiotensin II in Figure 27D and Figure 27F,

respectively. The increase and decrease of the DOCT signal is readily visible following administration of mannitol and angiotensin II. Corresponding OCT images are presented in Figure 27A,C,E for identification of glomerular region in the DOCT images. These images represent three different glomeruli due to the fact that multiple glomeruli were scanned for each physiologic condition and it was not readily feasible to return to the same exact glomerulus following injection of each agent.

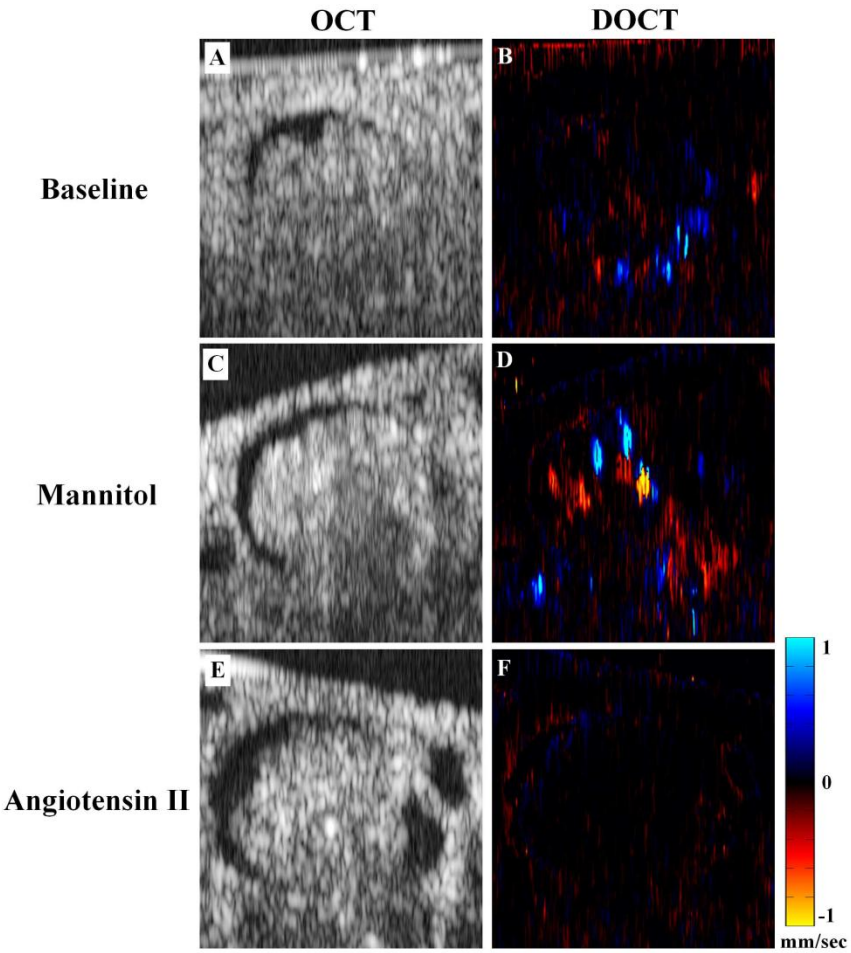

Figure 27. Representative OCT and DOCT images (XZ) from 3 different physiological states. A-B) baseline, C-D) after mannitol, and E-F) after angiotensin II. Comparison among the images shows differences in the observed DOCT signal in different glomeruli under altered blood flow conditions. Image size: 294 × 278 μm.

Analyzing the 3D data sets enabled quantitative evaluation of the DOCT signal within the glomerular region. By segmenting the DOCT velocity signal at each depth position (*en face* plane) according to a minimum background threshold ($|v_z|$ = 0.05 mm/s) and multiplying by the cross-sectional area of the segmented signal (as described in Figure 24), blood flow histograms of the 3D DOCT data sets were obtained. Figure 28A shows a representative baseline blood flow histogram from the 3D DOCT imaging with Figure 28B showing close up view of histogram base (region below dashed line). Similarly, Figure 28C-D shows a representative blood flow histogram after injection of mannitol solution and Figure 28E-F after injection of angiotensin II. Positive flow rates represent flow with a positive axial vector component (i.e. flowing upward) and negative flow rates represent flow with a negative axial vector component (i.e. flowing downward).

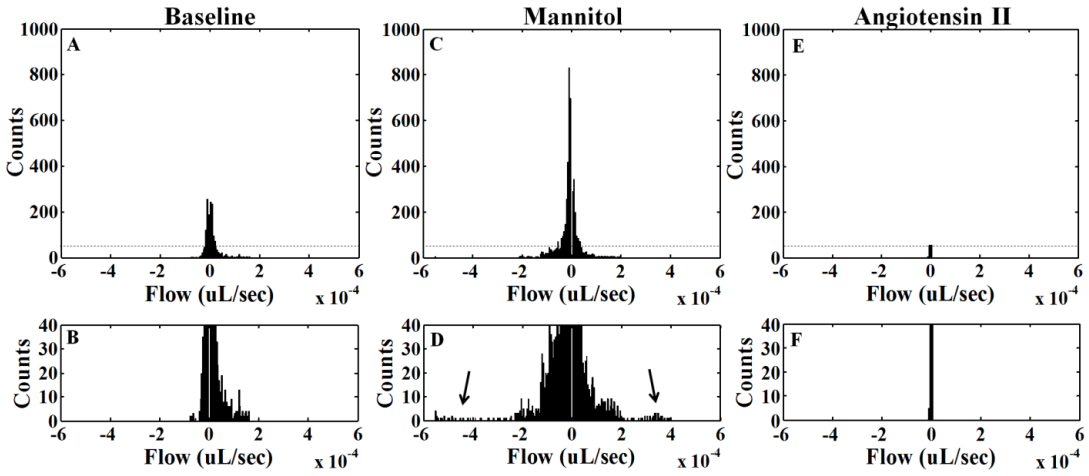

Figure 28. Blood flow histogram comparison. (A-B) Baseline blood flow histogram. (C-D) Blood flow histogram following injection of mannitol. (E-F) Blood flow histogram following injection of angiotensinII. Each histogram represents a compilation of the segmented DOCT signal at every *en face* plane through the depth of the glomerulus. Plots on the lower row are close-up versions at the base of the histograms (below the dashed line) in the upper row. Each group (A-B), (C-D), and (E-F) represents different glomeruli imaged in the same rat.

Following injection of mannitol, the histogram peak increased to 3 times higher than the baseline histogram peak. This histogram represents the observed changes in one glomerulus (not same glomerulus as baseline) depicting a significant increase in cumulative Doppler volume after administering mannitol (a mild vasodilator), but also, the maximum blood flow rate increased as noted by the wider range of flow rates (both positive and negative) as seen in Figure 28D (arrows) that are absent in the baseline histogram. Blood flow resulting after injection of angiotensin II (a vasoconstrictor) was also significantly affected. Figure 28E-F show flow rates only within one or two of the lowest histogram bins depicting a noticeable decrease of overall blood flow. While these three histograms demonstrate blood flow in three different glomeruli, the results reflect the overall type of changes observed in all the glomeruli imaged under each condition.

Three-dimensional (3D) analysis of OCT and DOCT data sets was performed to extract the total glomerular volume (GV), Doppler flow range (DFR), and cumulative Doppler volume (CDV) for each glomeruli imaged. Figure 29 shows the computed GV, DFR, and CDV from one representative rat kidney. Figure 29A shows the glomerular volume from each of the 7 physiological states induced during the experiment. Even though slight increases and decreases in glomerular volume were noticed throughout the different physiological states, no significant change in glomerular volume was observed

during all data sets collected. Figure 29B-C shows the DFR and CDV values from the 7 different physiological states in the same rat. For each state, an average of 3-4 glomeruli were analyzed. For each quantitative parameter, values for all glomeruli imaged during that physiological state were averaged and plotted with standard deviation.

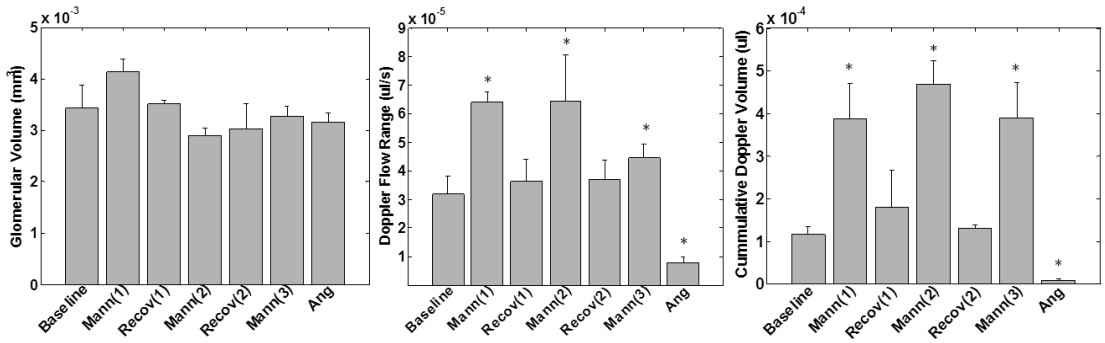

Figure 29. Analysis of in vivo DOCT imaging of rat glomeruli. (A) Glomerular Volume. (B) Doppler Flow Range. (C) Cumulative Doppler Volume. Each of these parameters was measured in multiple glomeruli under 7 separate conditions: baseline (n=3), following IV injection of mannitol (n=3), after the effects of mannitol diminished (n=4), following a second IV injection of mannitol (n=3), after the effects of mannitol diminished (n=3), following a third IV injection of mannitol (n=3), and finally following an IV injection of angiotensis II (n=6). Asterisk (*) indicates $p < 0.05$ compared to "baseline." Labels: Mann=mannitol; Recov=recovery; Ang=angiotensin II.

It is interesting to note that after both the first and second mannitol injection, the DFR and CDV values returned to near-baseline levels during the "recover" period indicating that the effects of the mannitol were wearing off (~15-20 minutes elapsed since injection). Shortly after administering the third mannitol injection to increase blood flow (10 min), angiotensin II was injected. This injection of angiotensin II reduced both DFR and CDV dramatically, well below the baseline level, even against the opposing effects of mannitol.

3.4.Discussion

Optical imaging using DOCT, a functional extension of OCT, is able to reveal single glomerular blood flow *in vivo*. It is important to note that all the observations were performed without introducing artifacts otherwise associated with penetrating the kidney (i.e., performed in a non-invasive fashion). Furthermore, DOCT requires no exogenous contrast agents like multi-photon fluorescence microscopy[108, 109, 135] and confocal laser scanning microscopy[136] and offers deeper tissue penetration than most optical microscopy techniques. Although DOCT can penetrate to a depth of about ~1-2 mm, monitoring renal microcirculation less than 500 μm below the kidney surface following renal transplantation has been reported to yield a promising predictive marker for post-transplant graft function.[137] An additional advantage of DOCT is that it can acquire numerous cross-sectional images in rapid succession yielding comprehensive 3D volumes of tissue. Such images can be used to determine the size, shape, and blood flow through glomeruli, thereby providing pathological information regarding glomerular disease. Fast imaging speed[138] and also the ability to be incorporated into needle[40, 139] and laparoscopic[140] devices for imaging blood flow in various orientations and even deeper in solid tissue or in not easily assessable locations allows DOCT to perform quick, repetitive 3D scans that can provide vital information for kidney evaluation. These unique aspects of DOCT might make this imaging technology useful in clinical settings.

In our study, we demonstrated the ability of DOCT to quantitatively image glomerular blood flow *in vivo*. Blood cell velocities (between ±1 mm/s) obtained with DOCT agree well with previous optical imaging studies[101, 136] as well as capillary blood

flow (~1-4×10^{-4} μl/sec) as compared with values reported in the rat cerebral cortex.[75] However, DOCT quantifies velocity by detecting phase difference and therefore has an inherent phase-wrapping effect (since phase detection is limited by ±π). The maximum detectable velocity (without phase-wrapping) is determined by the axial scan speed[141] and the minimum is based on the inherent phase noise present from the laser. In our system, 16 kHz axial scan rate yields our upper detection limit of ~±3.90 mm/s with minimum limit of ~±0.05 mm/s, which encompasses reported values of intra-glomerular blood flow. However, when imaging blood flow in arterioles, phase wrapping effect might be present (see Figure 25H). Future studies using higher-speed laser sources would solve this limitation.[138, 141]

One limitation involved in the DOCT signal segmentation is the fact that the intra-glomerular capillaries are at or below the axial resolution of our system and therefore speckle noise could be a significant factor that might affect quantification of the DOCT signal. Since the segmented DOCT signal is composed of numerous small DOCT clusters representing the small vessels within the glomerulus, a large number of the voxels are boundary voxels and thus may only represent partially filled voxels. Some of the partial voxel effects might be alleviated by de-speckling but all the values we reported were calculated directly from the raw segmented DOCT signal prior to any image processing. We did not pursue any correction method for the possible error accrued from incomplete voxels.

Furthermore, if the vascular pattern is of more interest, other techniques such as Doppler variance imaging,[118] speckle variance imaging,[142] optical coherence

angiography,[143] and optical microangiography (OMAG)[144] can be applied. Future studies are also needed to cross-validate the blood flow measured by DOCT with confocal or two-photon microscopy by using multi-modal optical systems.[145-148]

Characterization of the captured 3D Doppler signal within the glomerular volume by the CDV and DFR metrics can relate the Doppler magnitude and spatial volume observed in each glomerulus. While these two parameters are not sensitive to the same criteria, changes in capillary size/quantity and in flow speed will be detected by employing both in data analysis. For example, if the flow were to double while the capillaries remained the same size, the DFR would change accordingly but the CDV would remain constant. Likewise, if the number or size of the capillaries would change but the DFR did not, the CDV would indicate this change. By using both DFR and CDV metrics, alterations in the distribution (height or width) of the flow histogram can be detected and monitored for the 3D DOCT signal in each glomerulus.

While the Munich-Wistar rat model provides superficial glomeruli that can be readily observed, the capability of DOCT to detect glomerular blood flow in the human kidney has yet to be demonstrated. Previous studies show the ability of OCT to image glomeruli in the intact human kidney ex vivo [114, 115] and several of the studies mentioned above report using optical imaging methods at depths much shallower than DOCT to monitor renal circulation in animal models and transplant patients. Therefore, future studies using DOCT to quantify microcirculation changes compared with immediate and long-term transplant outcome and compared with renal disease progression would provide needed insights regarding possible future clinical applications of DOCT.

However, the sensitivity of DOCT to detect subtle changes that can be associated with disease states (such as diabetes or renal artery stenosis) or with abnormal states (such as anemia or partial/full nephrectomy) has not yet been demonstrated.[149] Thus, further studies are needed to evaluate native blood flow responses to renal disease in animal models and human patients in order to better understand the capability of OCT/DOCT to provide quantitative measurements of the kidney.

3.5.Conclusion

In these studies, using an OCT/DOCT system with ~12 μm axial resolution, ~2 μm transverse resolution, and 16 kHz axial scan rate we have demonstrated three-dimensional (3D), label-free imaging of microcirculation in the rat glomerulus *in vivo* under differing physiological conditions. After injection of mannitol, DFR increased to approximately 2 times baseline value and CDV increased to approximately 4 times baseline value. Then, after injection of angiotensin II, DFR and CDV decreased to less than 30% of baseline value. If larger bandwidth light sources are used, the axial resolution can be improved significantly and possibly resolving individual glomerular capillaries. Some studies report axial resolutions of ~2.5 μm[150] and even down to 1 μm.[151]

The ability of DOCT to visualize hemodynamic changes *in vivo* could provide a direct method for clinicians to evaluate kidney perfusion and response to therapy in real time. Furthermore, intraoperative visualization and analysis of alterations in renal perfusion associated with injury or disease may help improve renal health care in the future.

4. OCT/DOCT Imaging of Human Kidney Transplant

4.1.Introduction

4.1.1. Kidney Injury

Acute kidney injury (AKI) is a life threatening disease with a persistently high mortality and morbidity rate despite the advances in supportive care. AKI generally refers to an abrupt and sustained decrease of renal function resulting in retention of nitrogenous waste (urea and creatinine) in the blood and disrupted fluid and electrolyte homeostasis.[152-154] It has been estimated that the incidence of intrinsic AKI is approximately 115,000 cases/year.[155] AKI is typically diagnosed by observing rises in blood urea nitrogen (BUN) and serum creatinine (SCr).[55, 156, 157] However, BUN-to-SCr ratio is a suboptimal indicator of renal function during AKI,[157] and does not accurately reflect the degree of dysfunction until reaching a steady-state after several days.[158, 159]

A majority of AKI (50%) is caused by ischemic injury to the kidney.[157] Ischemia-reperfusion injury is involved in both cadaver and live donor kidney transplantation procedures. AKI, due to ischemia-reperfusion, is known to occur frequently after kidney transplantation and often leads to varying degrees of early renal dysfunction.[160] It is also known that 10-30% of AKI is caused by renal disorders.[156]

Considering renal causes in terms of anatomic compartments is helpful for the differential diagnosis of AKI.[156] AKI has distinct changes in both morphology (including loss of glomerular volume and tubular necrosis[161]) and function (including reduced blood flow and glomerular filtration rate[55, 156]). However, no objective tool currently exists in

clinics to rapidly detect the degree and extent of AKI, and consequently, therapeutic interventions are not able to be implemented effectively.

Since the timing of interventions is critical to the potential success and outcome of a therapy, the capability of early diagnosis of AKI, quantification of disease extent and severity, and evaluation of the response to early treatments is of great importance for a successful therapy. Therefore, there is a critical need to develop new diagnostic tools to assess the extent of disease, quantify the physiological parameters of disease, and evaluate disease progression or response to therapy *in vivo* and in real time. Such a technology would have a significant impact on the clinical diagnosis and prognosis of AKI patients.

4.1.2. Renal Blood Flow Imaging Modalities

Renal blood flow (RBF) is able to be imaged *in vivo* by several different imaging modalities. One commonly performed imaging modality for measuring RBF in the clinic is a renogram also known as a nuclear medicine scan. In this imaging procedure, the patient is injected with a radioactive isotope, such as technetium-99m linked to mercaptocetyltriglycine (^{99m}Tc-MAG3)[162, 163] or technetium-99m linked to d*iethylene triamine pentaacetic acid* (^{99m}Tc-DTPA),[164, 165] and then continuously imaged by a gamma camera to obtain a time series of the isotope as it is filtered out of the blood in the kidney. This type of scan is performed for an extensive amount of time, usually ranging from 30 minutes to 1 hour. However, interpreting the results of the scan is rather straightforward. A longer residency time of the isotope in the kidney, which is measured as a stronger signal than lower residency times, is indicative of reduced renal blood flow

due to the extended collection of emitted radiation coming from the kidney. However, the drawback of this imaging procedure is the need to inject, not only an exogenous contrast agent, but one that releases ionizing radiation. This can pose serious health risks to the patient from prolonged exposure times that are dependent upon the ability of the patient to filter and excrete the isotope from their body. Also, the low resolution of this imaging procedure is really only able to quantify RBF on a whole organ scale, or perhaps regionally at best.

A second imaging modality that can be used to measure RBF in the clinic but at a significantly higher cost is positron emission tomography (PET). RBF is measured by administering an IV injection of a radiotracer while the patient is in the PET imaging scanner. PET imaging of RBF is similar in principle to the nuclear medicine scan in that it captures a times series of the tracer as it is filtered out of the blood in the kidney. Like with nuclear medicine scans, PET imaging detects gamma rays, which result from positron emissions during the nuclear transformation of the tracer. Some of the predominant radioactive tracers that provide the contrast in PET imaging are O-15 labeled water ($H_2{}^{15}O$), Rubidium-82 (^{82}Rb), N-13 ammonia ($^{13}NH_3$), and Cu-62 pyruvaldehyde bis (n-4-methylthiosemicarbazone) (^{62}Cu-PTSM).[85] Studies have demonstrated the ability of PET to quantify RBF in animal models[166-168] as well as in humans.[86-90] The resolution of PET imaging (~5 mm) is better than the performance of the nuclear medicine scan, allowing for more localized quantification of RBF. But, the use of an exogenous radioactive contrast agent still poses similar health risks to the patient as the nuclear medicine scan.

Thirdly, magnetic resonance imaging (MRI) is another imaging modality that has the capability to image RBF in two different ways. One way is dynamic contrast enhancement (DCE) MRI and the other is by arterial spin labeling (ASL) MRI. DCE MRI follows a similar regime as PET imaging described above where a bolus injection of a contrast agent is administered and a time series of the tracer is imaged as it is filtered out of the body in the kidney. Some contrast agents used in DCE MRI are Gd-DTPA, polyamidoamine dendrimers, and gadoteridol.[169, 170] Studies have shown that using these contrast agents quantitative RBF measurements in animals[171-173] as well as in humans[91-93] can be obtained.

The other way to image RBF using MRI is through arterial spin-labeling (ASL). ASL MRI does not require an exogenous contrast agent in order to detect blood flow. By altering the magnetization of arterial blood water at a particular longitudinal plane compared to the magnetization of the surrounding tissue, ASL MRI can detects the magnetic decay of the arterial blood water with T1 against that of the surrounding tissue thereby utilizing an endogenous contrast agent rather than an exogenous one.[174] RBF has been quantified using ASL MRI in animal[175, 176] and in human[94] studies. However, in order to accurately determine the perfusion rate of the magnetically labeled blood, the blood and tissue magnetic field values must be known or assumed, along with the labeling efficiency, and the arterial transit time. Two detriments in ASL MRI come about from the need to use high-magnetic fields: 1) RF pulses at 3.0 T have a wavelength that approaches the size of the human head presenting the risk for standing electrical waves where concentrated RF energy can cause hot spots to generate in the brain, and 2) the homogeneity of the main magnetic field is much lower at 3.0 T than at 1.5 T because the

higher field strength gives rise to banding in the image acquisition and labeling of slices.[177] ASL also has the challenge of dealing with low signal-to-noise ratios and the complexity of flow quantification.[178, 179]

Lastly, RBF can also be measured using ultrasound (US) imaging in two ways, just like MRI. The first method is by using contrast-enhancement (CE) US and the second is by using Doppler US. US generates cross-sectional, depth-resolved images by propagating high-frequency sound waves through tissue and then measuring the echo delay of those waves with a transducer that must be in contact with the surface. This time delay corresponds to the acoustic impedance of the medium and along with the intensity of the echoes, US can compute 3D characterizations of the sample medium. Measuring RBF using CE US is performed by giving a bolus injection of microbubbles and then destroying the microbubbles with high intensity pulses and then measuring the rate at which the microbubble contrast agent replenishes the imaged region. Studies using CE US to quantify RBF have been performed in animal models[180-182] as well as in humans.[99, 100] Even though CE US uses microbubbles as a contrast agent, they are short lived (on the order of minutes). However, the microbubbles naturally degrade in the body without any toxic effects, which is a positive characteristic over other exogenous contrast agents. But, the necessity of using repetitive high mechanical index pulses to completely disrupt all the microbubbles currently residing in the kidney vasculature is likely to be poorly tolerated by some patients (who are often acutely unwell to begin with). This procedure is mildly complicated too by requiring successful destruction of the microbubbles followed by the capture of a time intensity curve to determine perfusion rate. In some of the

reported studies, completely destroying the microbubbles was sometimes challenging.

The second way to image RBF using US is by using Doppler US. Doppler US functions by detecting the frequency shift in the ultrasound waves due to moving reflectors in the imaged medium. The moving reflectors which Doppler US measures in tissue are red blood cells passing beneath the surface through the vasculature. Blood velocity can be determined by comparing the incident ultrasound frequency with the reflected ultrasound frequency, which can then provide an indirect measure of blood flow. Doppler US can also detect whether the blood is moving toward or away from the pulse beam depending on whether the reflected wavelength is compressed or expanded. Using this technique, studies have been performed to quantify RBF in humans to monitor various forms of renal disease and renal hemodynamics.[95-98] However, a recent study was performed comparing the accuracy of Doppler US with implanted laser Doppler flow probes, which are well-established devices to accurately measure blood flow invasively. The authors concluded that there are large variations in Doppler US agreement, and overall, according to the poor correlation with the measurements obtained from the flow probes, it has low accuracy with significant bias in quantifying RBF.[183]

The advantage of all the aforementioned imaging modalities is their ability to non-invasively image RBF with a wide field-of-view, allowing entire single- or dual-kidney monitoring and evaluation. However, the previous imaging modalities (excluding US) are really limited by their cost, widespread availability, and difficulty to be used at the bedside or during surgery. CE US, though, is receiving significant attention in recent years as a possible post-operation imaging modality to monitor kidney perfusion non-

invasively following renal procedures, such as transplantation. But, the drawback of exogenous contrast agents and the complexity of the imaging procedure, still make employing CE US in quantifying RBF a challenging feat for clinicians. Optical imaging techniques, though, that have higher resolutions and greater sensitivities could be a more feasible method for monitoring and evaluating RBF, especially in an intra-operative setting.

4.1.3. Optical Imaging Techniques for Renal Monitoring and Evaluation

Several optical imaging techniques have been employed to study the kidney. Studies using confocal[105-107] and multi-photon microscopy[108-110] have demonstrated the ability to image kidney structure and function on animal models, but the penetration depth has been limited to several hundreds of microns,[111] and therefore, using these imaging modalities is difficult for human studies due to the capsule surrounding the human kidney which can be several hundred microns thick. Nevertheless, optical imaging techniques have higher resolution than other imaging modalities and therefore are able to image the kidney on the cellular level to provide a direct measurement of RBF and GFR, which other imaging modalities are limited by their resolution capability. A relatively new optical imaging modality that can provide cellular level imaging but with deeper penetration than confocal or multi-photon microscopy is optical coherence tomography (OCT). OCT can provide subsurface imaging of biological tissues with deeper penetration depth (1-2 mm), and therefore, it can function as an "optical biopsy" to image kidney structure and function with a field-of-view (FOV) comparable to that of standard excisional biopsy and histology.[23, 184, 185] Subsurface imaging with OCT is similar to

ultrasound but has significantly higher resolution (5-10 times) than clinical US, providing depth-resolved imaging of tissue microstructure with micron-level resolution near that of histology. The advantage is that OCT imaging can be performed in real time without the removal of a tissue specimen for staining and subsequent histological analysis. OCT has already been successfully translated to various clinical applications including ophthalmology,[186] cardiology,[42] gastroenterology,[43-46] urology,[48, 187] and gynecology,[188] among others. However, clinical OCT imaging of the kidney is a new and under-explored area with strong translational potential.

In addition, OCT can detect blood flow *in vivo* using the Doppler effect just like US. Studies have shown the feasibility of quantifying blood flow *in vivo* in the human retina,[54, 63-67, 74] skin,[58, 68, 69] brain,[62, 70] and gastrointestinal tract,[50, 71] as well as other locations. Doppler OCT (DOCT) combines the ability of OCT to captured high-resolution structural images with corresponding Doppler velocity maps that can be merged together to identify regions with moving reflectors, indicating blood flow. Thus, OCT/DOCT is a powerful tool that combines structural and functional imaging which could be used to evaluate kidney status *in vivo* and in real time following surgical procedures.

4.2.Material and Methods

4.2.1. OCT System Setup and Design

A custom-built OCT system with a fiber-optic, hand-held probe was used in this study, enabling real-time, intra-operative OCT imaging during kidney transplant

procedures (see

Figure **30**). Briefly, the details of the OCT system used in this study consisted of a Fourier-domain OCT system with swept-source laser operating at 1310 nm center wavelength and 100 nm bandwidth with ~90 dB sensitivity. The OCT axial resolution was ~12 μm, and using a 4x objective (Thorlabs, NA=0.1) in the sample arm, a transverse resolution of ~15 μm was achieved as determined by resolution chart. Laser scanning (axial) frequency was 16 kHz enabling real-time 2D imaging. But, due to significant motion artifacts that naturally arise from using a hand-held scanner, *in vivo* 3D imaging data sets were not able to be captured during the surgery. OCT image pixel dimensions were as follows: 1024 [X] by 512 [Z], and associated 2D image scan dimensions were 3.75 mm [X] by 2.0 mm [Z].

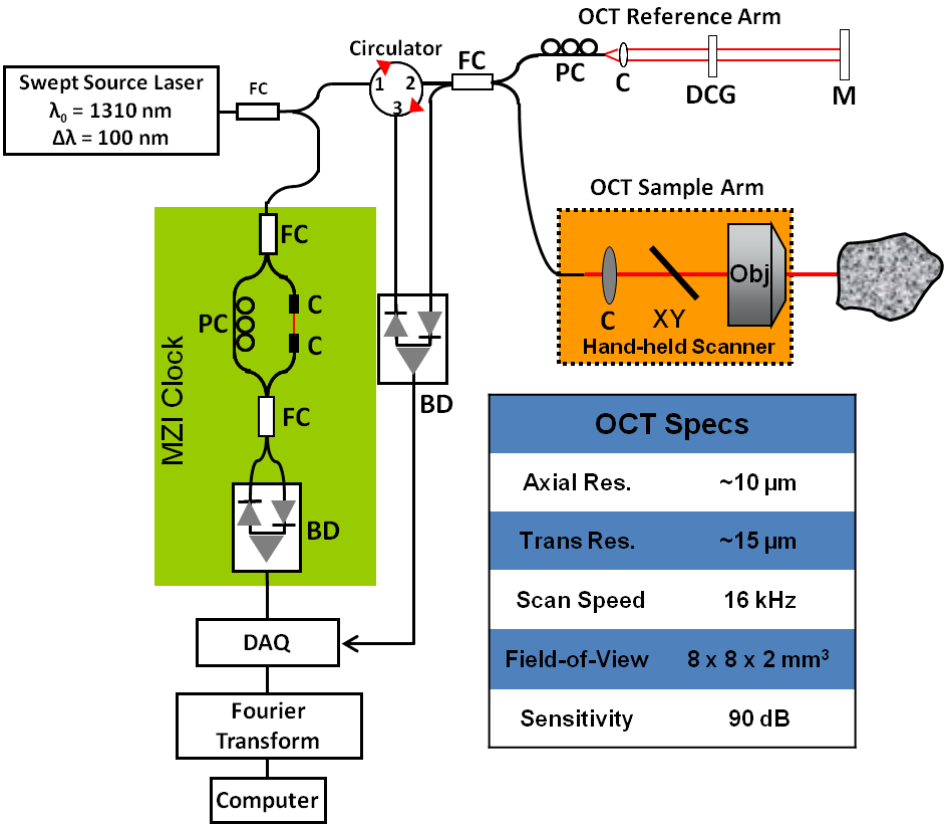

Figure 30. Schematic of hand-held OCT imaging probe for intra-operative kidney imaging. Axial and transverse resolution, imaging speed, field-of-view, and sensitivity parameters are listed in the inset table on the bottom right. OCT system schematic abbreviations, FC: fiber coupler, PC: polarization controller, C: collimator, MZI: Mach-Zehnder interferometer (frequency clock), M: mirror, BD: balanced detector, DAQ: data acquisition board, DCG: dispersion compensating glasses, OBJ: objective, XY: galvanometer mirrors.

Figure 31 shows a demonstration of the hand-held OCT imaging probe with a formalin-fixed human kidney *ex vivo*. The probe is gently placed on the surface of the kidney as depicted in Figure 31B. Applying only light pressure ensures that the subsurface kidney structure and blood flow are not significantly distorted or disrupted

during the imaging process.

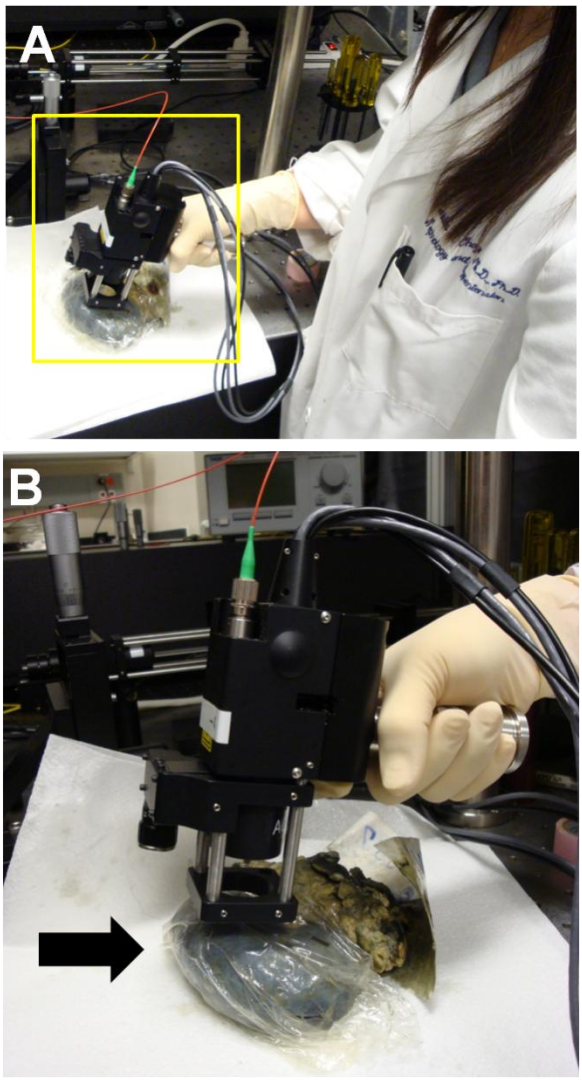

Figure 31. Demonstration of OCT handheld probe used in ex vivo and in vivo kidney transplant imaging. (A) Handheld probe is placed gently on the surface of an ex vivo fixed human kidney to reveal subsurface renal microstructures. (B) Close-up of the yellow box outlined in (A) showing further details of the OCT imaging with the handheld probe. Arrow indicates the imaging position of the hand-held probe on the surface of the kidney.

The hand-held OCT imaging device was assembled on a portable cart that can be easily wheeled into and out of the operating room during kidney transplantation

procedures. Figure 32 shows the portable imaging system on the three-level utility cart that was used to house and transport the system in this study. The imaging system was equipped with two output monitors facing opposing directions. One monitor enabled us to visualize and record the data while the second monitor let the physicians visualize the imaging, which aided in helping situate the probe at the optimal focusing position. This is further exemplified below in Figure 33 that shows the operation of the hand-held imaging probe by the physician during the transplant procedure.

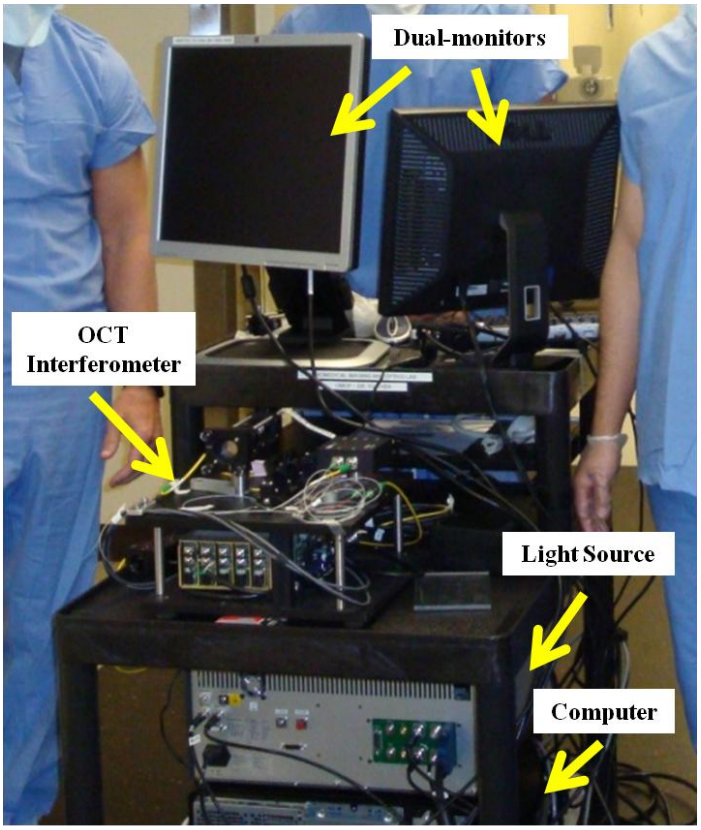

Figure 32. Portable hand-held OCT imaging system setup for clinical imaging during kidney transplantation. Dual-monitor output allows for simultaneous viewing by the physicians for evaluation and probe positioning and for our team for data collection.

4.2.2. Transplant Patients and Data Collection

Prior to engaging in this research, the protocol was approved by the Institutional Review Boards at both Georgetown University and the University of Maryland College Park. Patients scheduled to receive kidney transplant at Georgetown University Medical Center (Georgetown, Washington D.C.) were enrolled in this study between February and September 2011. Informed consent was obtained from all patients prior to imaging. A total of 8 patients enrolled in this study (2 female, mean donor age 53.67±8.76 yrs), and for each patient we imaged the kidney *ex vivo* prior to transplant and also following reperfusion *in vivo*. However, we were not able to collect data from the kidney *ex vivo* and *in vivo* in all patients due to technical complications. In total, we collected data from 7 *ex vivo* kidneys and 7 *in vivo* kidneys. From this data bank, we compared 4 patients' *in vivo* imaging data with measurements from standard clinical biomarker serum creatinine, which is a conventional indicator for post-graft renal function.

Following extraction of the kidney from the donor patient, the kidney was transferred to an ice bath solution prior to transferring it into the recipient. If adipose tissue was surrounding the kidney, the adipose was cut away from the kidney surface (part of the normal transplant procedure) exposing the kidney cortex. Next, the handheld OCT imaging probe was guided into a sterile sleeve and the sterilized lens and probe tip were secured onto the end of the probe by the physician's assistant.

After properly assembling the OCT imaging probe, several regions of the *ex vivo* kidney surface were then scanned using the handheld imaging probe. The handheld imaging probe used in this study is shown above in Figure 31. Since there is no blood

flowing through the *ex vivo* kidney, only OCT structure images were recorded for the *ex vivo* portion of the transplant procedures. After macroscopically surveying the cortex of the *ex vivo* kidney, the sterile imaging probe was placed on the surgical instrument table for imaging after the transplant. When the kidney was re-perfused in the patient after grafting, the transplanted kidney was imaged again *in vivo*. While gently stabilizing the kidney against the patient's abdominal wall, the physician imaged the cortex of the transplanted kidney at numerous locations on the surface. For *in vivo* kidney imaging, the fringe data (the complex OCT signal including both magnitude and phase information) was recorded to enable DOCT processing and analysis. Figure **33** illustrates the OCT imaging system position next to the surgical table in the operating room and the utilization of the hand-held imaging probe by the physicians to visualize the kidney *in vivo* immediately following reperfusion.

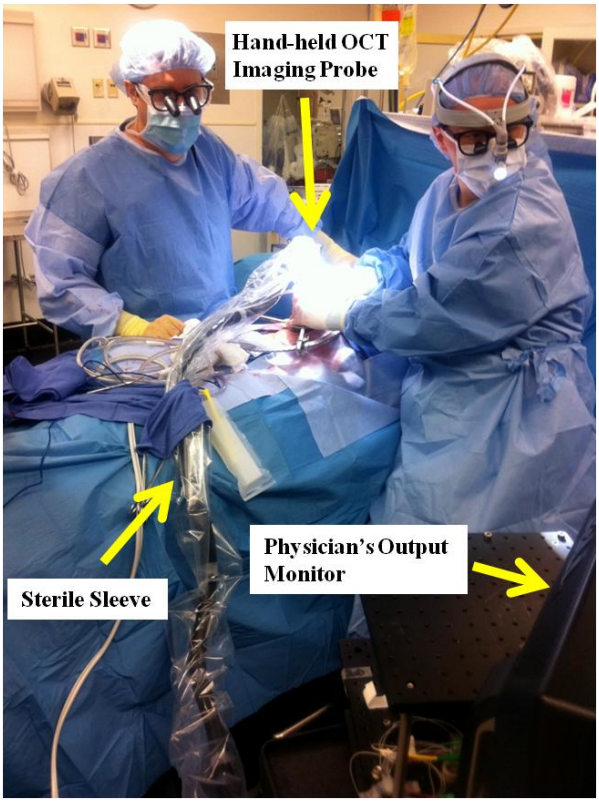

Figure 33. Intra-operative OCT/DOCT imaging of kidney post-reperfusion. The imaging system is kept several feet away from the operating table and only the handheld probe draped with a sterile sleeve is permitted to come into contact with bed and the patient.

For both *ex vivo* and *in vivo* kidney imaging, OCT images were taken at random locations across the kidney cortex totaling several hundred cross-sectional images that were stored on computer to be analyzed offline after the procedure. As mentioned above, during both *ex vivo* and *in vivo* kidney imaging occasions, a separate monitor was provided for the physician to visualize the real-time OCT imaging of the kidney they were performing during the surgery while allowing us to be able to observe and record the data using an auxiliary monitor.

4.2.3. Image Analysis

A subset of the recorded OCT/DOCT images that were in focus and free from significant motion artifacts (i.e. did not contain blurring from rapidly moving the probe) were exported from each patient for the *in vivo* portions of the transplantation procedure following reperfusion. A semi-quantitative analysis of the OCT/DOCT images was performed to evaluate the size/shape, density/uniformity, and blood flow observed.[189] Each category was scored according to the criteria listed below in Table 2. Scored values for the two tubule categories (tubule size/shape and tubule density/uniformity) were averaged and then the averaged value was added to the blood flow score for each patient to obtain an index value representing the overall status of the kidney. Thus, equal weight is given to the tubule and blood flow criteria in the scoring of the images. Example images of the tubule morphology for both the size/shape and the density/uniformity are provided in Figure 34. These images illustrate the visual appearance represented by the various scoring values and can be used as a training data set for standardizing the scoring system across multiple users.

Table 2. Scoring System for Semi-Quantitative Image Analysis

Rating	Tubule Size/Shape	Tubule Density/Uniformity	Blood Flow
N/A	Data is insufficient to rank parameter	Data is insufficient to rank parameter	Data is insufficient to rank parameter
1 (poor)	Tubules are closed	Very sparse tubules or no tubules are visible	Little to no blood flow was observed
2 (moderate)	Tubules are visible but with slightly deformed shape or smaller size	Tubule presence is heterogeneous or not consistently visible	Only couple vessels with blood flow were observed
3 (good)	Tubules are visible, open, and round	Uniform tubules are visible throughout all regions imaged	Numerous (>3) vessels with blood flow were observed

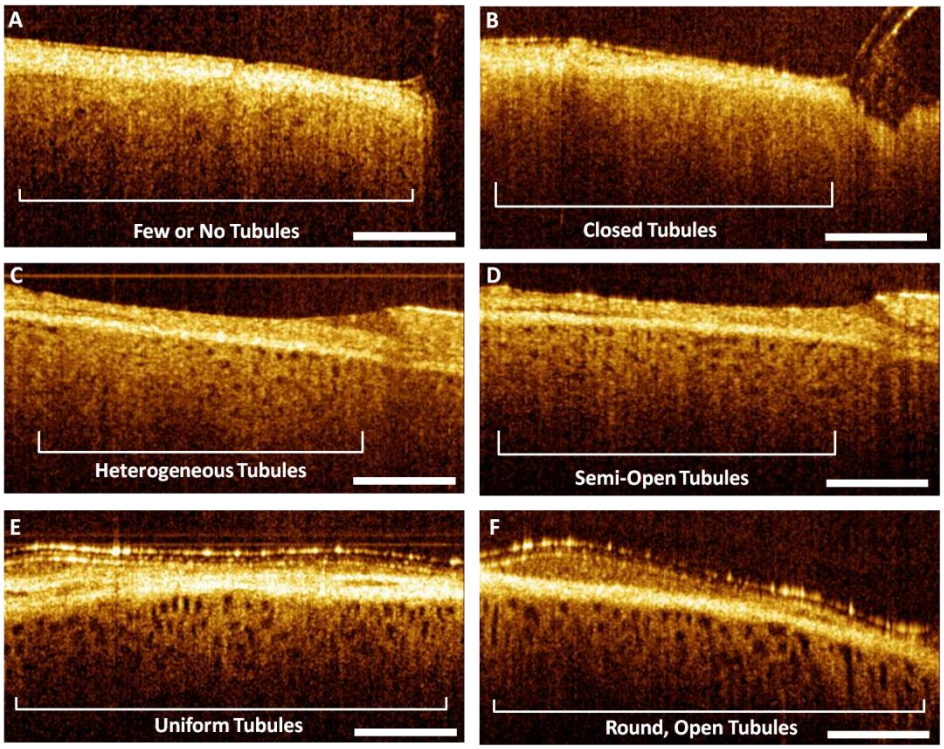

Figure 34. Examples of *in vivo* OCT images of human kidney depicting the scoring descriptions in Table 2 for tubule size/shape and tubule density/uniformity. Tubule size/shape: (A) poor (B) moderate (C) good. Tubule density/uniformity: (A) poor (B) moderate (C) good. Scale bar = 500 μm.

The image scoring results were then correlated with conventional biomarker measurements related to post-graft renal function. Image analysis results represent only a snap-shot of the kidney structure and function during the transplant procedure shortly after reperfusion.

4.2.4. Evaluation of Post-Graft Function

Post-operatively, serum creatinine (SCr) measurements were obtained daily for the first week after transplantation from Georgetown University Medical Center and were analyzed with standard clinical assays. SCr is a clinical "gold standard" parameter for evaluating renal graft function.[190] SCr plots were constructed for patients with post-transplant blood lab and *in vivo* imaging results. Comparison with pre-transplant SCr values was performed by plotting the relative change in SCr beginning on the day of the transplant. To compare post-transplant SCr with image analysis results, SCr at days 1 and 8 were plotted against the index value for each patient.

4.3.*Results*

4.3.1. Ex Vivo Kidney Imaging

OCT imaging was performed on donor kidneys while in ice bath prior to transplanting into the recipient. Excess perirenal fat was cut away as part of the normal procedure exposing the kidney surface for imaging. The donor kidney surface was

surveyed while soaking in the ice bath to globally assess the renal microstructures (tubules, vessels, and glomeruli). Figure 35 shows representative OCT structural imaging of the *ex vivo* kidney before transplantation. The kidney capsule is visible along with the renal parenchyma but, in general, the renal microstructures (e.g. renal tubules) were not visible. Occasionally a tubule, vessel, or glomerulus appeared but most of the *ex vivo* imaging data is similar to the example shown in Figure 35.

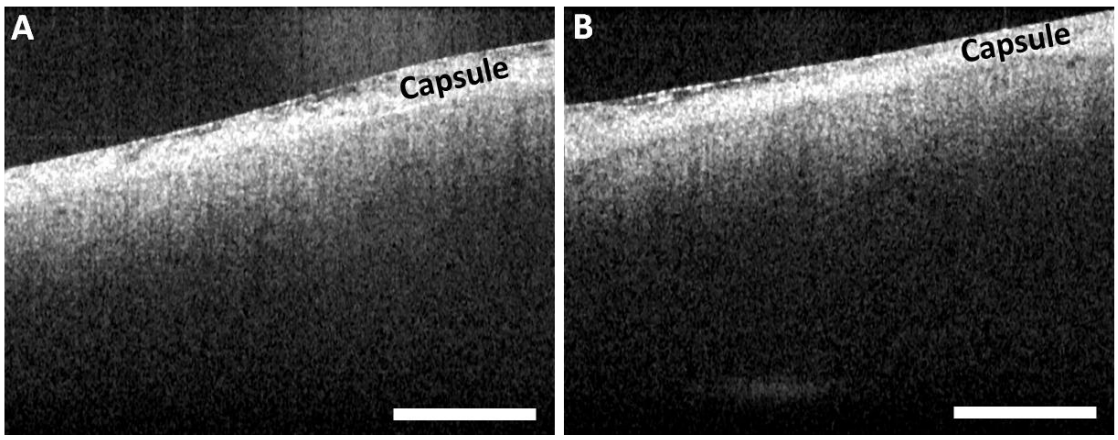

Figure 35. *Ex vivo* OCT imaging of human donor kidney. Very few renal structures were visible below the capsule prior to transplantation. Data from patient #7. Scale bar = 500 μm.

4.3.2. In Vivo Kidney Imaging

Immediately following grafting of the donor kidney into the recipient and unclamping of the renal vessels, we performed OCT/DOCT imaging of the transplanted kidney within the abdominal cavity of the patient as illustrated above in Figure **33**. Real time OCT structural imaging revealed numerous uriniferous tubules below the renal capsule as depicted in Figure 36 and Figure 37, which represent data from two different patients.

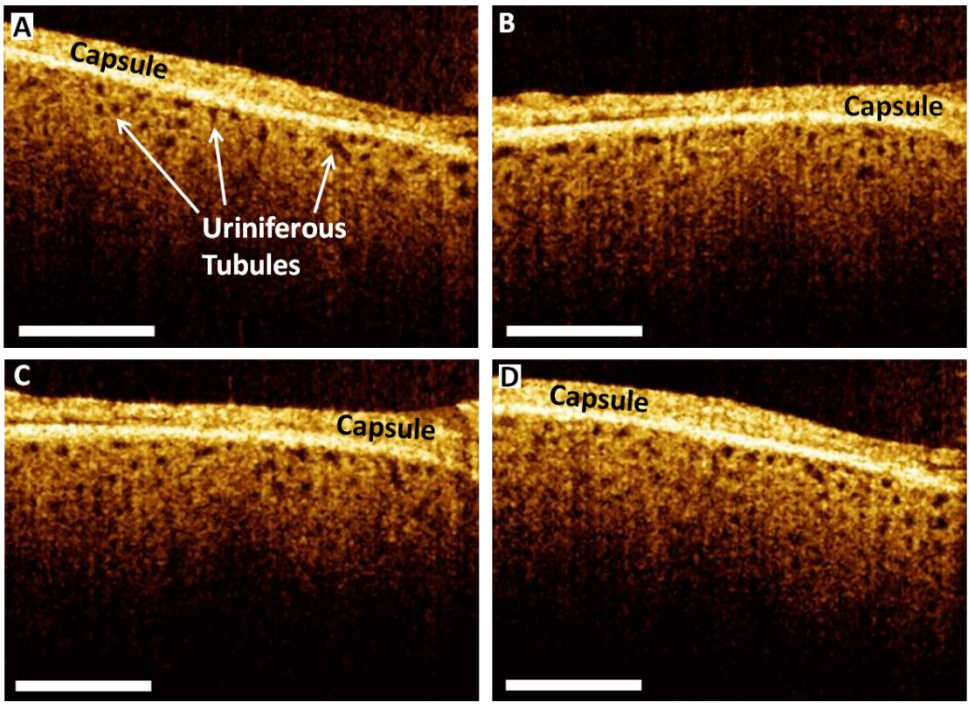

Figure 36. OCT imaging of *in vivo* human kidney showing open uriniferous tubules below the renal capsule. Tubules appear to be fairly open and round with some degree of homogeneity throughout the images. Data from patient #2. Scale bar = 500 μm.

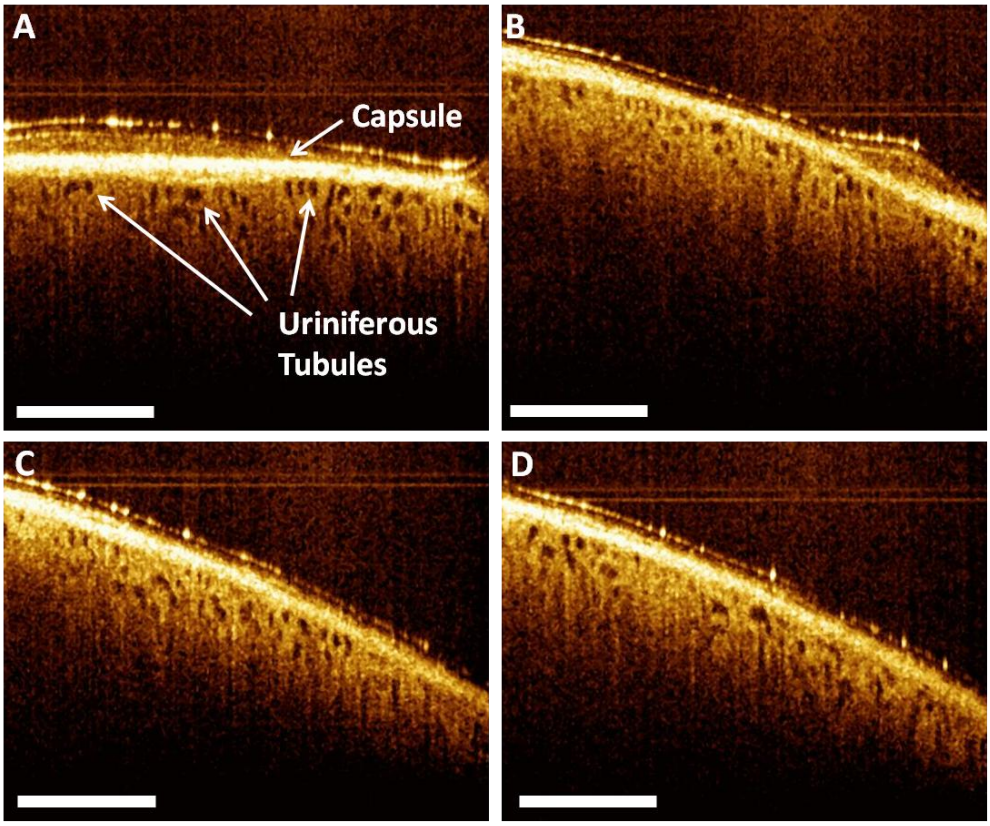

Figure 37. OCT imaging of *in vivo* human kidney showing uriniferous tubules below the renal capsule. Tubules appear to be very open and mostly round in shape and homogeneous throughout the images. Data from from patient #6. Scale bar = 500 μm.

OCT fringe data was also recorded during *in vivo* imaging to enable DOCT imaging for visualizing blood flow in real time. Figure 38 demonstrates OCT/DOCT imaging of the transplant kidney *in vivo*. OCT is displayed in grayscale and DOCT is overlaid with a colormap. Blue-cyan represents blood flow in one direction while red-yellow represent blood flow in the opposite direction. While several vessels are noticed in Figure 38A-D, no open tubules are observed around the vessels. Closed tubules indicate no glomerular filtration and thus a lack of renal function.

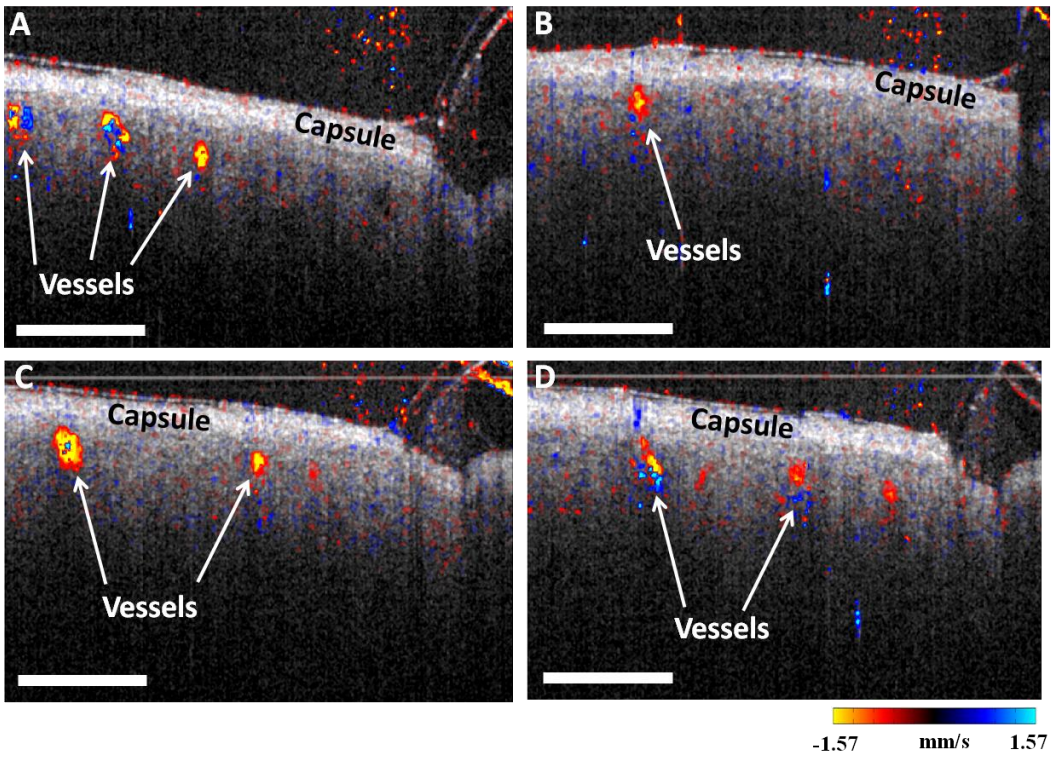

Figure 38. OCT/DOCT imaging of *in vivo* kidney. Blood flow is seen in numerous cortical vessels but uriniferous tubules appear to be closed and not visible in adjacent image regions. Patient #5. Scale bar = 500 μm.

While surveying the kidney surface of patient #5 *in vivo*, several regions had closed tubules as noted above in Figure 38. However, as the hand-held imaging probe was moved to other parts of the kidney open tubules were readily visible. An example of the difference between regions with closed tubules and open tubules is shown below in Figure 39. Other regions of the kidney imaged in patient #5 showed visible open tubules distributed throughout the parenchyma (see Figure 40).

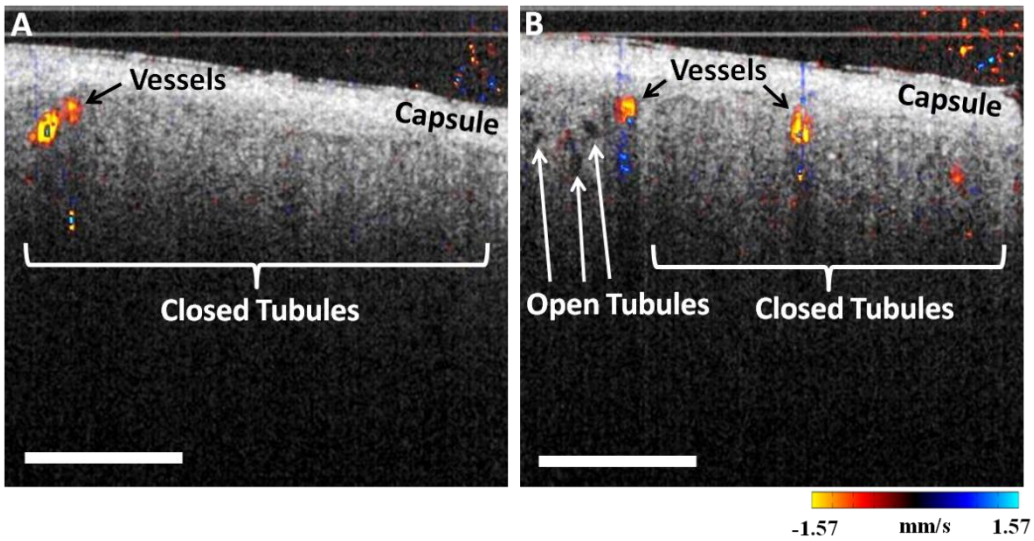

Figure 39. OCT/DOCT imaging of *in vivo* human kidney showing regional variations in the openness of uriniferous tubules. (A) Tubules are closed and thus not visible, suggesting impaired renal function in this region. (B) Right side of image shows closed tubules again but left side reveals region with open tubules. Data from patient #5. Scale bar = 500 μm.

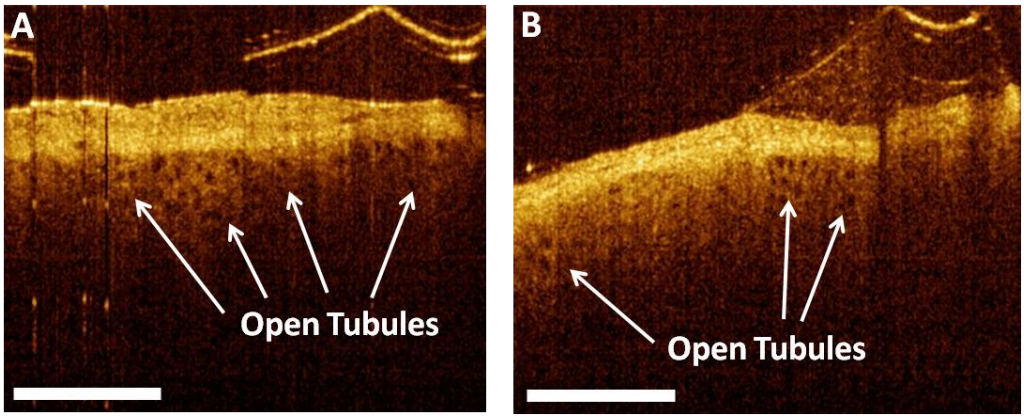

Figure 40. Additional OCT/DOCT imaging of *in vivo* human kidney showing regional variations in the openness of uriniferous tubules. (A) Open tubules can be seen below capsule. (B) Some regions display open tubules while others do not have open tubules. Data from patient #5. Scale bar = 500 μm.

Figure 41 shows the combination of morphological imaging with OCT and

functional imaging with DOCT for one patient that displayed good tubular morphology and blood flow. Fairly densely packed uriniferous tubules are observed with several cortical blood vessels indicating perfusion.

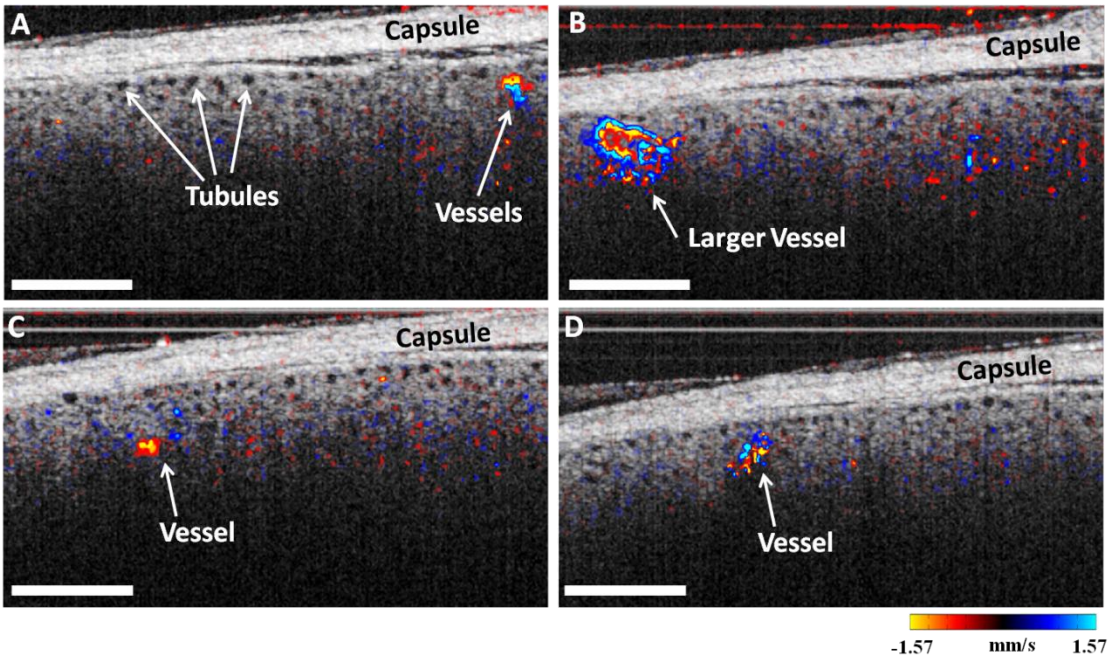

Figure 41. *In vivo* human kidney showing open tubules and cortical blood flow. Open tubules appear round and relatively uniform across all images. Also, a larger blood vessel is seen in (B) against some smaller vessels observed in (A,C,&D). Data from patient #3. Scale bar = 500 μm.

The combination of OCT and DOCT for visualizing renal microstructures and blood flow can enable the assessment of renal function and possibly predict graft outcome. Based on these morphological and functional criteria, a semi-quantitative analysis was performed on six of the eight patients (two patients did not have sufficient *in vivo* data for the analysis). The results are summarized below in Table 3. Scoring values for tubule size/shape, density/uniformity, and observed blood flow in all *in vivo*

OCT/DOCT data sets are based on the defined criteria listed above in Table 2.

Table 3. Human Kidney Transplant Semi-Quantitative Image Analysis

Patient #	Donor	Tubule Size/Shape	Tubule Density/Uniformity	Blood Flow	Index
1	Living	N/A			N/A
2	Living	2	2	2	4
3	Living	3	3	2	5
4	Living	N/A			N/A
5	Living	2	2	3	5
6	Living	3	3	1	4
7	Living	2	2	1	2
8	Living	2	2	1	2

Lab results for daily creatinine levels from patients #2, #3, #5, & #6 (patients #1 & #4 had insufficient imaging data and we currently do not have lab results for patients #7 & #8) are shown below in Figure 42. As a clinical parameter measuring post-graft renal function, serum creatinine is used to indicate the acceptance of the donor kidney and its capacity to filter the blood in the recipient.

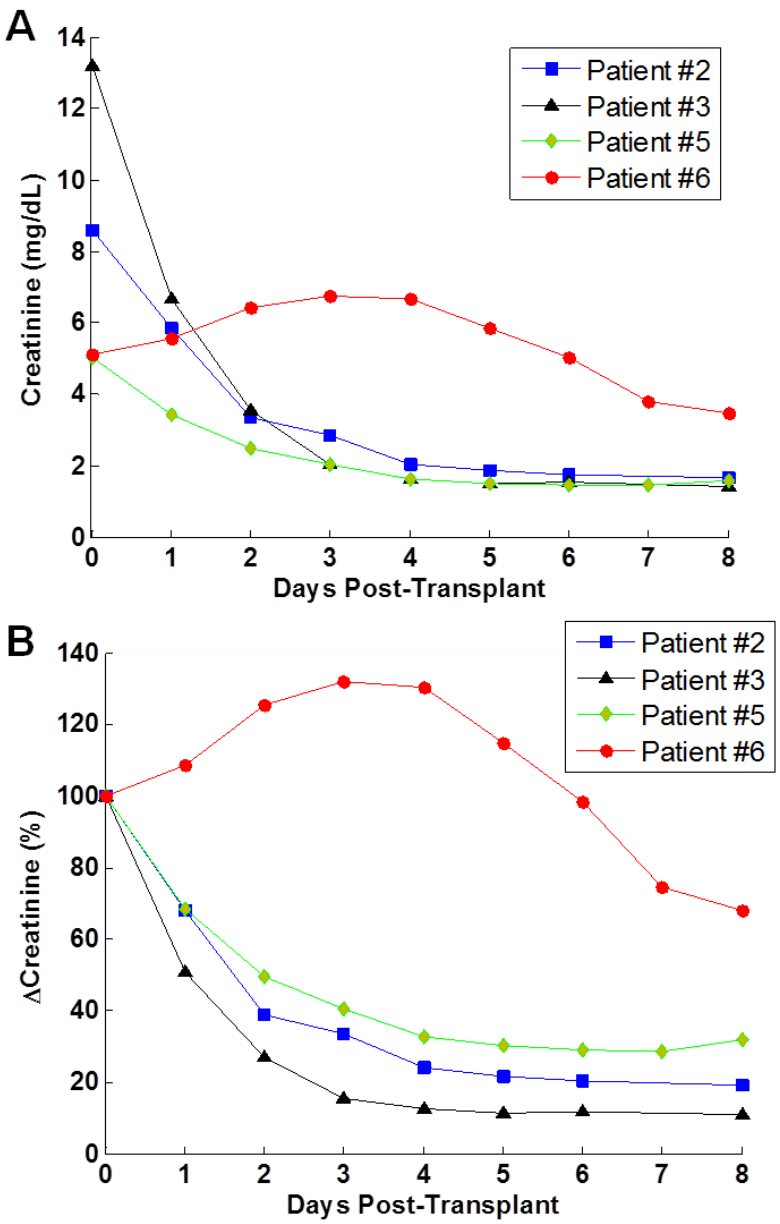

Figure 42. Summary of serum creatinine values for the first post-operative week. (A) Serum creatinine values are plotted for 4 patients with OCT/DOCT *in vivo* imaging data (patients #2, #3, #5, & #6). (B) Percent change in serum creatinine from day 0. Measurements were taken daily for each patient for the first week following transplantation (excluding day 7 for patients #2 and #3). For the remainder of the patients, the cause is due to either: 1) insufficient *in vivo* imaging data to correlate with biomarkers, or 2) lack of lab data from the Medical Center patient database.

The post-operative serum creatinine levels for the first week following transplant for patients #2, #3, #5, & #6 were then compared to the scoring results from the semi-quantitative analysis in Table 3. Figure 43 shows the results of the correlation on post-operative days 1 and 8. It can be noted that by day 8, 3 of 4 patients had reached near-normal creatinine levels (horizontal dashed line). The outlier in Figure 43B is patient #6 which displayed an increase in creatinine several days post-operatively before beginning to decrease on days 4-5 (see Figure 42).

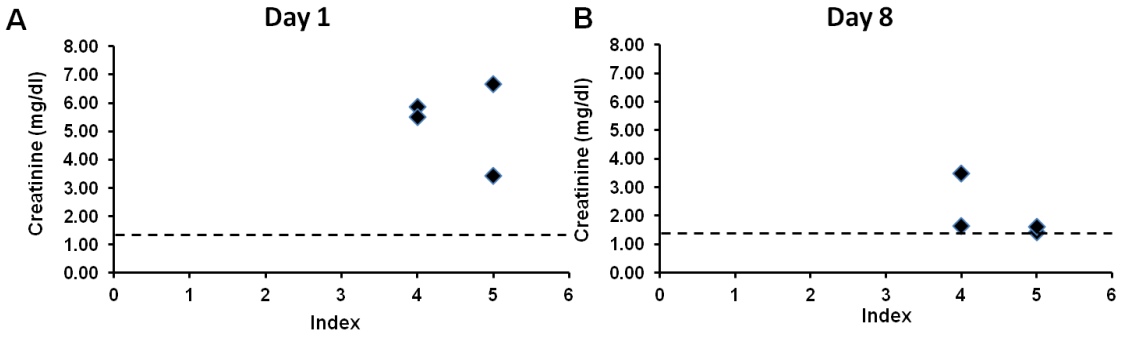

Figure 43. Correlation between serum creatinine at day 1 and day 8 post-operative and the OCT/DOCT image scoring index. Horizontal dashed line indicates upper-limit of normal creatinine levels (~1.3 mg/dl). Data from patients #2, #3, #5, & #6.

4.4.Discussion

During transplantation every kidney undergoes a period of ischemic injury and then reperfusion due to the nature of transferring the kidney from the donor to the recipient. However, in light of this detriment, no pharmacologic interventions have been found that protect the kidney from this injury. Ischemia-reperfusion injury is known to cause tubular obstruction that decreases glomerular filtration rate and arteriolar vasoconstriction that disturbs glomerular blood flow.[191] Tubular morphology has been

shown to be correlated with ischemia time in rabbit kidney transplant studies,[106, 192] and also a recent study has demonstrated that renal microcirculation changes might be able to predict early renal graft dysfunction induced by ischemia-reperfusion injury.[137]

This study demonstrates the feasibility of OCT/DOCT imaging of the human kidney during kidney transplantation. OCT/DOCT imaging results were scored according to morphological and functional characteristics as a diagnostic parameter to predict post-graft renal function. The scoring index from the semi-quantitative imaging analysis was then compared with standard biomarker (serum creatinine) measurements that reflect post-graft renal function. However, this study is only an initial pilot study and has too few patient numbers to draw any definitive correlation between the imaging results and kidney graft function. The preliminary results of this study suggest that OCT/DOCT may be a useful tool in intra-operative monitoring and evaluation of the transplant kidney for predicting post-graft function after ischemia-reperfusion injury.

One patient (#6) displayed a slight rise in serum creatinine (SCr) level following transplant until approximately day 4 when it began to decrease. This abnormal behavior could have been due to several causes. First, the transplanted kidney might have experienced some ischemia-reperfusion injury causing a brief delay in its functioning after transplant. However, this seems unlikely as the ischemia time for the living donor kidney is quite short (~1-2 hours). Second, acute rejection of the kidney sometimes results in delayed functioning of the kidney. Thirdly, certain medications (e.g. certain antibiotics) administered to the patient can cause elevated SCr even with a fully functioning kidney. However, the cause for the abnormal SCr of patient #6 has not yet

been established. Imaging results from patient #6 appeared to be quite good and were ranked as such in the semi-quantitative scoring analysis. Further background information on the post-transplant evaluation of the patient and any medical interventions are necessary in order to identify the cause for the delay in renal function.

4.4.1. Critique of Methods

We acknowledge that there are several limitations in this study. First, as already mentioned, the lack of patient numbers makes it challenging to determine the correlation between our optical imaging results and the post-graft function of the kidney. Higher patient numbers are necessary to determine the accuracy of using OCT/DOCT to predict post-graft outcome. Secondly, the semi-quantitative image analysis is not the most objective method for analyzing the imaging data. Computing the average tubular diameter and tubular volume ratio (ratio of tubular volume per volume of parenchyma) would be more objective measures to rank the morphological parameters of the OCT data. Performing 3D OCT/DOCT imaging would allow for more versatile metrics to be employed to quantify the image results, such as quantifying blood flow. However, image motion from the hand-held probe presently precludes 3D imaging. Better stabilization of the kidney within the patient's abdomen and securing the imaging probe to an articulating mechanical arm could dramatically reduce motion artifacts during *in vivo* imaging that would allow for 3D image volumes to be recorded.

4.4.2. Future Direction

Recent studies have shown a dramatic difference in renal microvascular blood flow (blood cell velocities) between grafts from deceased donors versus living donors.[191,

[193] Since ischemic injury duration has already been correlated with post-graft function in rabbit studies using OCT, a clinical trial that investigates this technique in humans for living donors versus deceased donors would yield likely promising insights into the correlation between the duration of ischemic injury and post-graft function. The present study focused solely on living donors that had a relatively short duration of ischemic injury. We have demonstrated the ability of OCT to imaging living donor kidneys, therefore, the results suggest that it is a suitable image modality to investigate the longer ischemic times associated with deceased donors as well.

Because deceased donor kidneys experience a longer duration of ischemia leading to varying degrees of delayed-graft function, they are at a higher risk for subsequent failure or rejection. Due to the shortage of kidneys for transplantation in relation to the large number of patients with terminal renal failure, there is an increase in the number of marginal kidneys that are being transplanted.[190] At this time there is no objective tool to assess the status of donor kidneys or to predict the post-graft outcome of a donor kidney in the recipient. OCT's ability to reveal the subsurface renal microstructure could be used to assess donor kidney status and thereby predict the post-graft function of the kidney in the recipient. Pre-transplant assessment of donor kidney status is of benefit because it might indicate potential increased risk in marginal donor kidneys where the recipient could profit from additional interventions or treatment. However, further work is required to investigate the potential markers and correlation of renal microstructure with graft outcomes. And, in addition, further work is necessary to establish the efficacy of therapeutic maneuvers in cases with donor kidneys that might potentially present delay-

graft function or other post-operative complications.

4.5.Conclusion

OCT is a powerful medical imaging technology that can reveal microstructure and blood flow in biological tissue in real time. Our preliminary results demonstrate the feasibility of using OCT to assess kidney status immediately following reperfusion by examining tubular morphology and density and renal blood flow *in vivo*.

With ~12 μm axial and ~15 μm transverse resolution and 16 kHz axial scan rate, our OCT system revealed renal tubules and cortical blood vessels in real-time during transplantation procedures. Due to significant motion from the hand-held scanner, 3D OCT imaging was not able to be performed with our current image acquisition speed. However, this limitation could be solved by using faster laser sources with higher scanning rates. One study reported using an OCT system with axial scan rate of 370 kHz yielding sub-second 3D volume data set acquisition (~0.7 s).[194] Furthermore, using novel laser sources, some studies report being able to perform scan rates reaching even 5 MHz.[195, 196] At this scan rate it would take only 52 ms to perform a 3D scan consisting of 262144 axial scans (XY: 512×512). Higher scanning rates would decrease motion artifacts during image acquisition and also enable faster blood velocities to be detected with DOCT.

Furthermore, by comparing a scoring index consisting of multiple imaging parameters with post-graft function, the diagnostic potential of OCT was investigated for the first time. All *in vivo* data sets yielded good quantitative results that correlated well with patient creatinine levels after 1 week post-transplant. However, our study requires

additional patient numbers to definitively identify any correlation with graft-outcome. In addition, improved diagnostic parameters with 3D imaging could better assist in determining the capacity of OCT to predict post-graft renal function.

5. OCT Imaging of Renal Cancer in Humans

5.1.Introduction

5.1.1. Renal Cancer

Renal cancer is the 7th leading malignant condition among men and 12th among women in the United States and accounts for 3.8% of all cancers.[197] The American Cancer Society estimates that approximately 60,920 (37,120 in men and 23,800 in women) new cases of renal cancer will present and 13,120 (8,270 men and 4,850 women) patients will die from this disease in the United States alone in 2011.[198] Approximately 1 in 67 people (1.49%) will develop renal cancer (prevalence) with the highest incidence in people over 55 years of age.[198] The most common form of renal cancer is renal cell carcinoma (RCC) that arises from the epithelial lining of the uriniferous tubules and collecting ducts (~90%).[199] The age-adjusted incidence of RCC has increased over the past 30 years at an annual rate of approximately 3%.[200, 201] RCC consists of numerous subtypes of cancer including: clear cell, papillary, chromophobe, collecting duct, and unclassified. Other renal cancer types are: transitional cell, Wilms tumor, and renal sarcoma. However, there are also benign tumor types that arise such as renal adenoma, oncocytoma, and angiomyolipoma. Renal cancer displays distinct morphological changes on the microscopic level and eventually dramatic tissue re-organization on the macroscopic level allowing it to be stratified into various cell types and stages.[199]

About 20-30% of newly diagnosed renal cancers have been found to be benign,[202-206] and it is difficult to pre-operatively distinguish benign versus malignant

masses. Pre-operative biopsy and diagnosis of solid renal masses from radiographic images is variable due to inaccurate sampling, and permanent needle biopsy and CT have been reported to have 20% and 31% non-diagnostic rates, respectively.[202, 204, 207] Therefore, there is a need for an objective method that would improve the capability of differentiating benign from malignant renal tumors, thereby preventing unnecessary and potentially morbid surgical procedures.

In addition, the incidence of renal cancer has increased with the identification of smaller renal masses (<4 cm) due to the advancement of pre-operative abdominal imaging modalities, such as computed tomography (CT) and magnetic resonance imaging.[204, 208]

5.1.2. Renal Cancer Treatment

For solid renal masses, nephron sparing procedures have been developed as an alternative to radial nephrectomy.[36] Although highly effective, open surgery can be deleterious in elderly patients with multiple co-morbidities and increased surgical risks. Radical nephrectomy is not always necessary for small lesions, and thus, nephron sparing procedures such as partial nephrectomy and renal ablation are growing in popularity.[206] However, achieving a negative tumor margin is critical to ensuring the best oncological efficacy.

Nephron sparing surgery is now established as the standard of care for small localized renal tumors[209, 210] with excellent long-term survival reported using open surgery[211] and laparoscopic techniques[212]. Tumor resectioning or ablation therapy (including cryo-ablation and radio-frequency ablation) have emerged as promising

treatment modalities for small renal tumors with encouraging short-term follow-up results.[213-216] However, a main challenge of these minimally-invasive therapies is to accurately identify the tumor margin to preclude tumor recurrence. Currently, the standard of practice during nephron sparing procedures is to incorporate prior knowledge from radiographic images, ultrasound, and experience to determine the tumor area to ablate or resection. Therefore, an objective means of identifying a negative tumor margin still remains needed to assist the physician in determining the tissue margin surrounding the mass. The ability to accurately assess tumor morphology in real time to differentiate tumor from normal tissue and aid in optimal tumor treatment requires high-resolution imaging techniques where currently employed large field-of-view modalities and intraoperative ultrasound are insufficient.

Over the last decade significant progress has been made in the area of non-invasive or minimally-invasive imaging that has increased the sensitivity and specificity of renal cancer diagnosis. The reliable diagnosis of patients with renal neoplasms can provide physicians with the ability to develop patient-specific treatment options based on the malignant potential of the mass. Optical imaging techniques are suitable candidates that could improve diagnostic and therapeutic evaluation of renal masses intra-operatively.

5.1.3. OCT Imaging

Optical imaging technologies have the potential to provide real-time, high-resolution imaging of human tissue *in vivo* with resolutions near that of histopathology; therefore, it may significantly improve the clinicians' capability to accurately guide

biopsies and correctly identify tumor margins intra-operatively. Confocal microscopy has been demonstrated to image kidney structure and function,[105-107] but the penetration depth has been limited to several hundreds of microns. Optical coherence tomography (OCT) is another emerging biomedical imaging technology that can provide subsurface imaging of biological tissues, similar to ultrasound images, but with significantly higher resolution (5-10 times).[23, 184, 217] OCT has deeper penetration depth than confocal microscopy (~1-2 mm) and can function as a type of "optical biopsy" to enable visualization of tissue microstructure that can be performed repeatedly in real time and without the removal of tissue.[111]

OCT can be readily interfaced with fiber-optic catheters, endoscopes, laparoscopes, and needle imaging probes to image inside the body.[38-40] Endoscopic/laparoscopic OCT has been demonstrated in the human cardiovascular system,[42] gastrointestinal tract,[43-46] pulmonary tract,[47] urinary tract,[48] among others. These previous endoscopic studies demonstrated that OCT imaging could be readily integrated with standard endoscopic/laparoscopic procedures and provide valuable diagnostic information in situ and in real time. OCT guided biopsy has the potential to reduce sampling errors and improving surgical outcomes by accurately identifying tumor margins. The capability of OCT to visualize and quantify kidney structures in situ would be promising for differentiate the normal, benign, and malignant tissues.

5.1.4. Previous Studies

Pathologically, renal cancers exhibit distinct morphological differences compared to normal tissue, including architectural changes in the tubular diameter, volume, density,

and basic tissue organization and cell type. Standard histology can confirm cellular changes in tissue organization and cell type with resolutions at the single micron level. OCT has resolutions near that of histopathology but relies only on backscattered light for contrast. One previous study using an 890 nm OCT system investigated the ability of OCT to distinguish the appearance of normal and neoplastic (tumor) renal tissue *ex vivo* in human patients. By qualitatively comparing OCT images to that of conventional histology, differences in certain types of neoplastic tissues were able to be discerned while others were not able to be successfully differentiated. The authors concluded that transition cell carcinoma (TCC) and angiomyolipoma (AML) displayed unique identifiable features from normal parenchyma, but oncocytomas and other renal carcinoma subtypes (papillary and chromophobe) differed only subtly from normal renal parenchyma in the OCT images.[218] Therefore, due to a general heterogenous appearance in the OCT images of normal parenchyma and most renal cancer types (excluding TCC and AML), reliable differentiation was limited.

It is also known that malignant renal tissues exhibit larger and irregularly shaped nuclei compared to that of normal tissue lending to an increase in the nuclear-to-cytoplasm ratio.[219-221] Changes in nuclei/cytoplasm ratio will affect the optical properties of the tissue by the index of refraction mismatch. This cellular transformation in malignant tissue suggests that there may be a discernable difference in the optical signature from normal versus tumor tissue. Previous studies using optical reflectance spectroscopy have established that there are different light scattering properties between tumor and normal renal tissue and even between malignant and benign tumor tissue.[222-224] Based on diffuse reflectance measurements, the spectra between normal and tumor renal

tissue diverges continuously with respect to wavelength between 600-900 nm. These studies indicate that there is a discernible difference in optical signatures that can be detected between normal renal tissue and tumor tissue.

Tissue optical properties can also be estimated from the OCT axial profile (A-scan).[225] Recently, one group performed a study using OCT A-scans of human renal tissue *ex vivo* to extract the attenuation coefficient (μ_t = scattering, μ_s + absorption, μ_a) of normal and malignant renal tissue to quantitatively measure tissue optical properties. While an overall comparison of all their data yielded a significant difference between normal parenchyma and RCC tissue, a significant difference was not observed comparing each patient individually.[226] Our results build off of this study by including addition patient data with improved imaging penetration. We hypothesize that there will be a significant difference in the attenuation coefficient measured with OCT between normal and tumor renal tissue.

5.2.Materials and Methods

5.2.1. Renal Specimen

The protocol used in this study was approved by the Institutional Review Boards at both University of Maryland Baltimore campus as well as University of Maryland College Park campus. Patients that were scheduled for removal of suspicious renal mass underwent partial or complete nephrectomy at the University of Maryland Baltimore Medical Center (Baltimore, MD) were enrolled in this study between June and November 2011. Informed consent was obtained from all patients prior to imaging. A total of 9 patients participated in this study (4 laparoscopic partial nephrectomies and 5 radical

nephrectomies). One patient included in this study had cancer arising from the collecting duct (urothelium) instead of from renal cell. In total, we collected data from 17 specimens (8 normal parenchyma and 9 tumors). For one patient, no normal parenchyma could be identified apart from the invasive tumor that nearly constituted the entire kidney. Therefore, only a tumor specimen was retrieved and imaged for that patient. When the imaging was completed after the surgery, each specimen was then stored in a clean container and sent to pathology for evaluation.

5.2.2. Sample Preparation

Immediately after surgical excision of the renal mass, the specimen was placed in holder and placed on separate examination table. If adipose tissue was surrounding the kidney, the adipose was gently cut away and a portion of the kidney cortex at the tumor site and at a normal region was exposed for imaging. Upon finishing exposing the kidney surface, a random macroscopic region (~1 cm^2) representative of the renal mass was selected upon visual inspection by the surgeon followed by the selection of a random macroscopic region (~1 cm^2) representative of normal parenchyma. Residual blood was rinsed away from the surface with saline solution and the specimen was then placed beneath the OCT microscope with the selected regions positioned appropriately for capturing 3D imaging of the site. No alteration or cutting of the specimen was performed after removal from the patient.

5.2.3. Data Collection

The details of the OCT system used in this study have been described previously.[114] Briefly, a Fourier-domain OCT system with swept-source laser operating at

1310 nm center wavelength and 100 nm bandwidth was used in this study. The OCT axial resolution was ~12 μm, and using a 4x objective (Thorlabs, Inc., NA=0.1) in the sample arm, a transverse resolution of ~15 μm was achieved as determined by USAF resolution chart. Laser sweep rate was 16 kHz enabling rapid 2D and 3D imaging. 3D data set voxel sizes were as follows: 1024 [X] by 512 [Y] by 512 [Z]; associated 3D data set dimensions were 8 mm [X] by 9 mm [Y] by 2 mm [Z].

Images were taken at 2 standard locations per specimen *in situ* (see Figure 44 for partial and radical nephrectomy diagrams). 3D data sets were recorded for each representative location totaling several hundred cross-sectional 2D OCT images that were stored on computer to be analyzed offline at a later date. Some specimens allowed for more than or fewer than 3 samples per tissue type, but overall, an average of 6 samples were taken from normal and tumor tissue (3 from each type) in all patients (excluding 1 that had entirely tumor tissue).

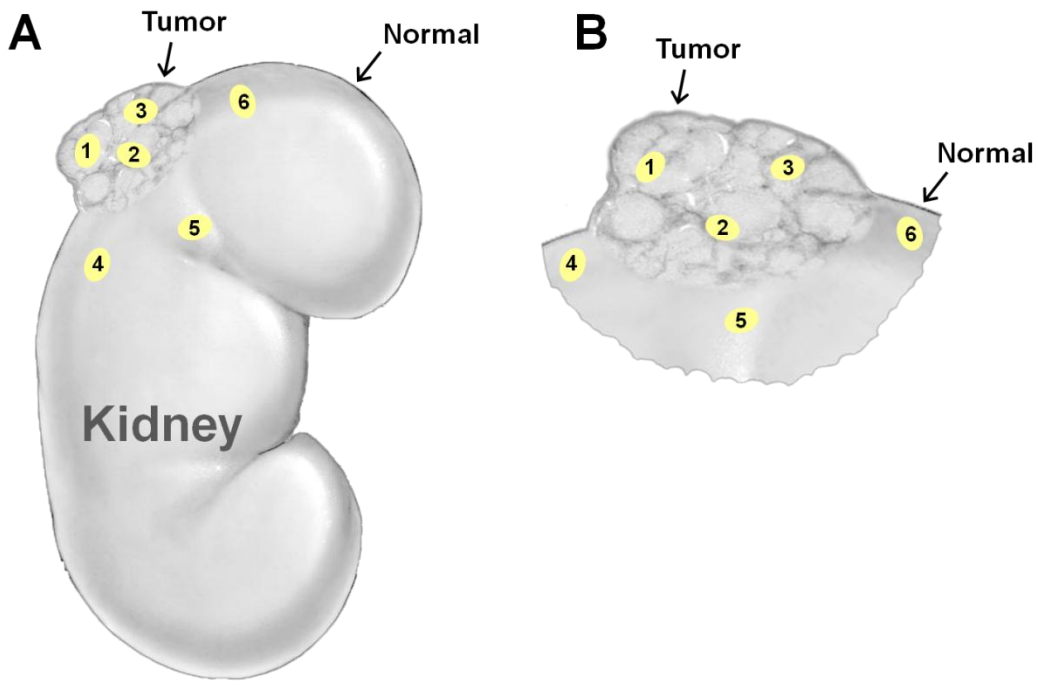

Figure 44. Location of OCT imaging during both (A) radical and (B) partial nephrectomy. Sites #1 – #3 are on the surface of the tumor while sites #4 – #6 are on the surface of normal parenchyma in regions where there is no peritumoral adipose tissue covering the capsule.

5.2.4. Image Analysis

A subset of raw OCT intensity images were exported from each patient for both tumor and normal tissue and analyzed using custom image analysis software written in Matlab (Mathworks, Natick, MA, USA). OCT images were selected based on minimal surface reflection to decrease the incident of image artifacts from detector saturation. Within selected images, axial scans free of artifacts, large vessels or other structures, and excessive shadowing were chosen for analysis. The backscattered-light intensity attenuation coefficient (μ_t) of each axial scan was determined using a modified-single scattering model that takes into account the confocal gate and the point spread

function.[227] The attenuation coefficient can be calculated from the modified-single scattering model function by solving for μ_t in Eq. (1):

$$i(z) = \frac{1}{\left(\frac{z - z_{cf}}{z_R}\right)^2 + 1} \cdot e^{-2\mu_t z} \tag{14}$$

where *i* is the axial OCT signal, *z* is the depth position, z_{cf} is the confocal gate focal position, z_R is the 'apparent' Rayleigh length used to characterize the point spread function (PSF). If a renal capsule was present in the OCT image, the attenuation coefficient was measured beginning below the capsule. Also, areas with low surface reflection and detector saturation artifacts were selected for calculating the attenuation coefficient of the tissue.

5.2.5. Pathological Evaluation

Standard pathological report was considered to be the gold standard for verifying tumor and normal tissue from kidney specimens. A summary of the pathological diagnosis of each patient is displayed in Table 4.

Table 4. Patient demographical and pathological data.

Number of patients	9
Mean patient age (years)	52.1
Male:female	6:3
Patients with tumor and normal kidney tissue	8
Patients with only tumor tissue	1
Pathology diagnosis:	
RCC, clear cell	4
MF RCC, papillary + clear cell	1
Papillary	1
Transitional cell	1
Angiomyolipoma	1
Oncocytoma	1

*RCC = renal cell carcinoma
*MF = multifocal

5.2.6. Statistical Analysis

Comparisons were made among the patient diagnoses in cooperation with a certified pathologist that was blinded to the selected regions of the kidney that were imaged. From the OCT data analysis, comparisons between the attenuation coefficient in tumor and normal kidney tissue were performed across all patients, treating each tissue type (normal or tumor) in each patient as a cluster of dependent observations related to each other). All attenuation coefficient (μ_t) values are reported as mean ± standard error.

All data collected were analyzed with SAS software (SAS Institute Inc., Cary, NC, USA). Data comparison across all patients was performed using a linear mixed effects model to analyze statistical significance between normal renal tissue and tumor tissue among the cohort. The linear mixed effects model takes into account data where observations are not independent and compensates for the continuous dependence of

random effects, hierarchical effects, and effects found in repeated measures. From the linear mixed effects model, a p value < 0.05 from the statistical test was considered to be significant.

5.3.Results

A total of 17 specimens (8 normal parenchyma and 9 tumors) from 9 patients were imaged with OCT during this study. One patient had renal cancer arising from the collecting duct instead of having a renal cortical mass. Both benign (oncocytomas and angiomyolipomas) and malignant tumors (all other tumor types listed in Table 4) were evaluated for their optical attenuation patterns against normal renal parenchyma. An example of normal parenchyma and tumor tissue is displayed in Figure 45 with representative axial profiles from each comparing the optical attenuation between the two tissue types. Furthermore, Figure 45 also shows an example histogram of the attenuation coefficients obtained for both normal and tumor tissue types. While a separation can be seen between the attenuation coefficient for normal versus tumor tissue, other regions in from this patient did not exhibit such a distinct difference. This pattern of inter-region variance was observed in nearly all patient data.

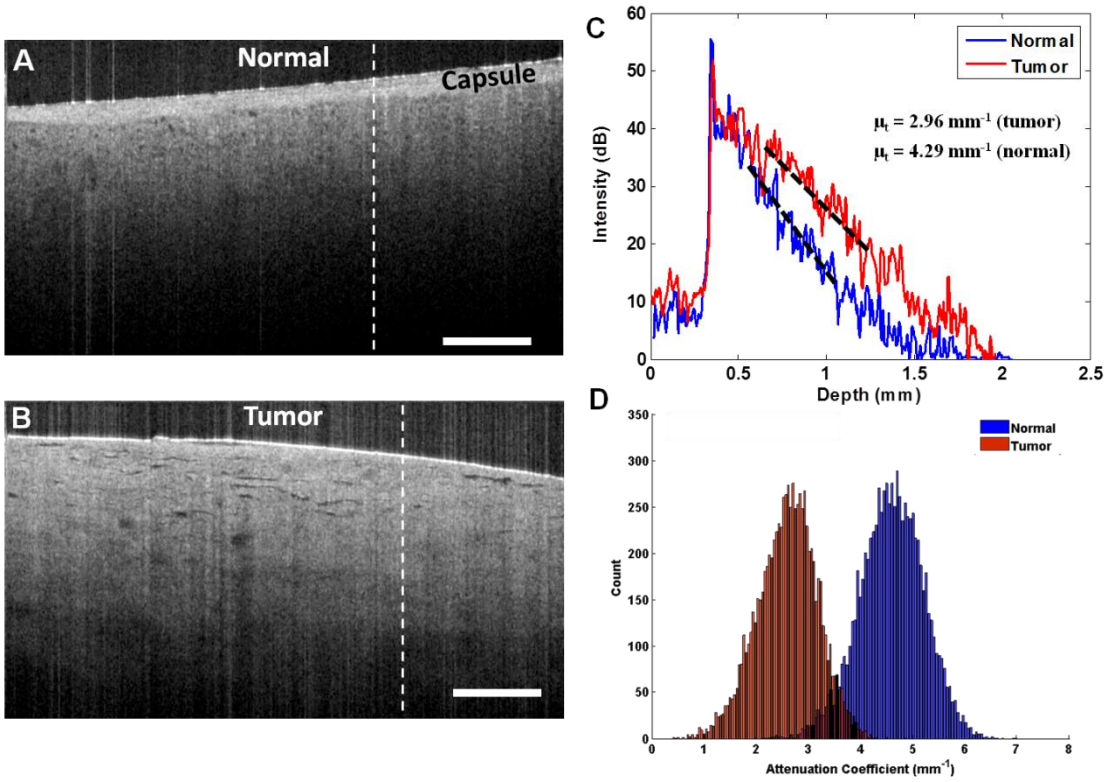

Figure 45. Representative OCT images and axial profiles for renal tissue from (A) normal and (B) tumor regions. Plot (C) displays axial profiles from the vertical dashed lines in (A) & (B) with the tissue surface positions aligned for easier comparison. The attenuation coefficients (μt) for normal and tumor tissue types using a modified single exponential decay model were 4.29 mm^{-1} and 2.96 mm^{-1}, respectively. Renal capsule is apparent in the normal tissue (A) but not in tumor tissue (B). Attenuation fitting was taken from below the capsule and at a similar depth in tumor as indicated by the dashed lines of the model fit seen in (C). (D) Attenuation coefficient histogram of normal and tumor tissue showing the distribution of the attenuation coefficient in both regions. Data from Patient #2. Scale bar = 500 μm.

Upon visual inspection of the OCT images from normal and tumor tissue in all patients, differences in tissue features and patterns can be discerned in most patients (see Figure 46). However, some patients exhibited similar tissue appearance between normal and tumor tissue types (e.g. patients #2 and #8).

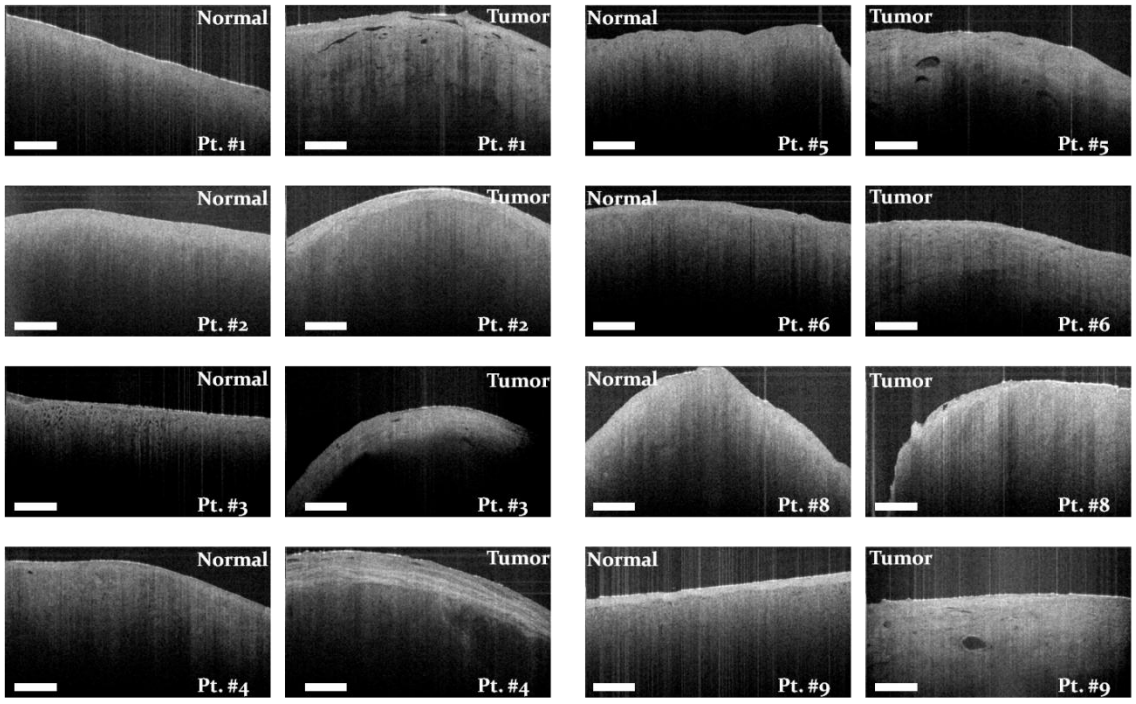

Figure 46. Representative OCT images from normal and tumor regions for all patients (excluding patient #7 with only tumor tissue). Variations between normal and tumor tissue can be observed in majority of patients. However, variations even in the normal tissue can be seen among all the patients. Scale bar = 500 μm.

Since multiple locations on normal and tumor tissue were imaged in 3D, a large amount of axial scan attenuation coefficients were computed for each patient. To accommodate for the high number of attenuation coefficients, each 3D data set was divided into ~10 sections and the attenuation coefficients were then averaged within each section. This yielded ~60 attenuation coefficients for each patient from the ~6 regions that were imaged (~2-3 normal and ~2-3 tumor). The mean attenuation coefficient (μ_t) ± standard deviation for each patient as well as the overall comparison between the two tissue types is given below in Figure 47. From 23 normal kidney regions in 8 patients yielded an average attenuation coefficient of 4.41±0.74 mm^{-1}, and from 26 tumor regions

in 9 patients yielded an average attenuation coefficient of 4.32±1.26 mm^{-1} (see Figure 47B). The corresponding patient-specific pathological diagnosis is listed in Table 5. Four patients had RCC clear cell type, one patient had transitional cell carcinoma, one had RCC papillary type, and another had multifocal RCC with combined papillary and clear cell type. Two patients had benign tumors: one angiomyolipoma and one oncocytoma.

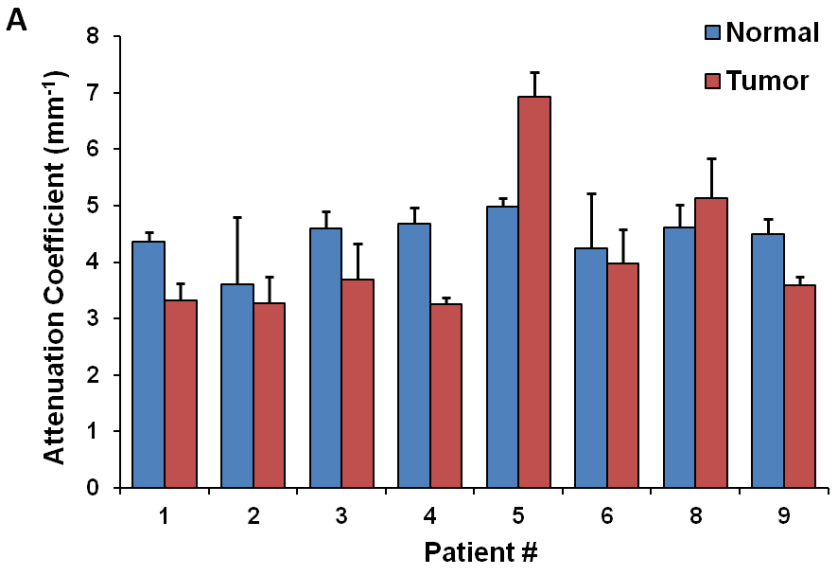

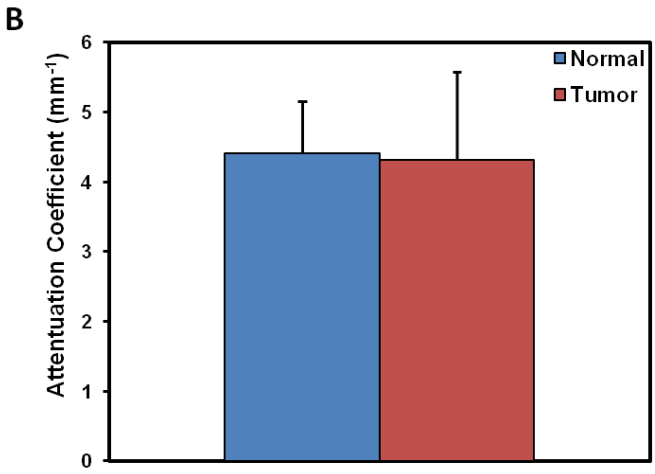

Figure 47. Quantitative OCT imaging analysis results. (A) Attenuation coefficient (μ_t) for normal and tumor tissue for each patient (excluding patient #7 which had only tumor tissue). Number of regions imaged per type of tissue for each patient is as follows (normal, tumor): patient #1 (n=2, n=2), patient #2 (n=3, n=3), patient #3 (n=4, n=5), patient #4 (n=2, n=2), patient #5 (n=1, n=2), patient #6 (n=5, n=3), patient #8 (n=2, n=2), patient #9 (n=2, n=3). (B) Overall comparison between normal and tumor tissue across all regions of each tissue type from each patient (normal, n=23; tumor, n=26).

Table 5. Patient-specific pathological diagnoses from Figure 47.

Patient #	Pathology
1	Angiomyolipoma
2	RCC, clear cell
3	RCC, clear cell
4	Oncocytoma
5	RCC, clear cell
6	Transitional cell carcinoma
7	MF RCC, papillary + clear cell
8	RCC, clear cell
9	RCC, papillary

* RCC = renal cell carcinoma
* MF = multifocal

Across all 8 patients, a linear mixed effects model analysis was performed on the attenuation measurements from the comparison between normal (n=281) and tumor (n=348) tissue. The statistical significance of the analysis was determined to be $p = 0.2718$.

5.4.Discussion

High-resolution, 3D imaging data sets of human kidney *ex vivo* were acquired using OCT for investigation of the optical properties of renal tumor tissue against normal

renal tissue. OCT is already an established medical imaging technology in ophthalmology[228] and has also demonstrated strong potential in cardiology[229, 230] and gastroenterology[231-233].

OCT provides cross-sectional images of optical backscattering with resolutions at ~12 μm that can enable non-invasive of tissue morphology. This sort of "optical biopsy" can allow repeated sampling of tissue *in situ*. In many medical fields, OCT has become a promising tool for cancer detection in the breast[234], gastrointestinal tract[235], bladder[236], skin[237], oral cavity[238], cervix[239], lung[240], and brain[241], among others. However, only two published studies to date have investigated OCT in detecting renal neoplasms.

One study focused on distinguishing renal neoplasms from normal parenchyma based on characteristic architectural features seen in histology using an 800 nm OCT system. The authors concluded that certain types of neoplasms (aniomyolipoma and transitional cell carcinoma) exhibited distinct morphologic elements allowing them to be discerned from normal tissue while identification of other neoplasms (oncocytoma and various RCC subtypes) was more unreliable.[218]

Another group investigated using the characteristic of optical attenuation in tissue from the OCT axial scan to distinguish renal cancer from normal parenchyma. The authors reported no significant difference ($p=0.069$) between normal and cancer tissue within each patient, but collectively across all patients, they found a significant difference ($p=0.03$) between renal cancer and normal parenchyma.[226] Overall, the authors observed a higher optical attenuation coefficient in renal cancer tissue than in normal tissue when

same tissue types were all grouped together.

In contrast to this, our results show, in general, a lower attenuation for renal tumor tissue compared with normal renal tissue (see Figure 47). Only two patients exhibited higher attenuation in tumor over normal tissue. However, our estimation of normal renal attenuation μ_t (~5 mm^{-1}) is agreeable with their results of normal parenchyma. While we had the same sample size (n=8) and optical attenuation model as the previous study, our study includes samples from patients with benign tumors and non-RCC tumors while the former study selective focused on comparisons between normal and RCC tissue. We also observed high variation between normal and tumor tissue across all patients but found no statistical significance between their attenuation coefficients (p=0.2718).

As seen in Figure 45, our OCT image penetration depth was ~0.8 mm for normal and ~1.2 mm for tumor. The depth of penetration improvement in tumor tissue substantiates the lower attenuation coefficients noted in Figure 47. However, these results did not match our expectation according to the larger and irregularly shaped nuclei that are known to characterize malignant renal tissue compared to normal parenchyma. These cellular changes are thought to give rise to an increase in refractive index mismatch and thus a higher attenuation coefficient.

In our study, six out of eight patients with both normal and tumor tissue showed a lower attenuation coefficient in the tumor tissue than normal parenchyma. Two patients displayed the opposite trend, i.e., higher tumor attenuation than normal. One patient with significantly higher tumor tissue attenuation was diagnosed with transitional cell carcinoma, which is a renal malignancy that arises from the urothelial cells lining in the

renal calyces, collecting duct, and ureter. With the small sample size in this study it is difficult to draw any conclusions on the observed variance in optical attenuation values. It may be that differences in architectural changes that are associated with certain renal malignancies account for such inconsistencies in optical properties. However, more specimens are needed and then comparisons within each category of tumor type might reveal optical characteristics unique to classes of renal neoplasms.

This study contains several limitations in its scope. First, all images were recorded *ex vivo* with no blood perfusion and collapsed renal microstructures like uriniferous tubules and glomeruli. Therefore, since this experimental condition is drastically different from in the living kidney, determining the attenuation coefficient *in vivo* may pose certain challenges. Primarily, the quantification of tissue attenuation from the axial profile may encounter artifacts due to the hollow tissue structures, such as renal tubules that are abundant throughout the superficial cortical layer. For accurate quantification of the attenuation coefficient from OCT images, image processing algorithms that remove the large fluctuations caused by these structures from the axial profile will need to be employed to compensate for regions of the tissue that are optically translucent. This will improve the quantification accuracy and reduce variability in fitting the attenuation model.

In addition, we are using a modified single exponential decay model that takes into account the confocal gate and beam profile to fit the optical attenuation in the tissue. The modified single scattering model is an improved model over the simple single exponential decay which has been widely used by other research groups to quantitatively

differentiate normal and abnormal breast tissues[242] and oral cancers.[243, 244] But, more complicated attenuation decay models that incorporate multiple scattering effects can also be utilized to improve the accuracy of the optical attenuation fitting.[245] Furthermore, alternative image processing and quantification algorithms can be employed to extract additional metrics from OCT images that could be used as diagnostic markers. Joint spatial frequency[246] and texture image analysis methods, which are sensitive to tissue architectural features as well as the smoothness, coarseness, and regularity of speckle patterns[247, 248], that have been shown to distinguish normal and cancerous tissues could be beneficial in detecting renal neoplasms as well. Along with additional image quantification algorithms, improved axial resolution to ~5 μm has been reported to enhance detection of upper gastrointestinal tract cancer with spatial frequency analysis and statistical texture analysis methods.[249]

While this pilot feasibility study (like the other associated reports mentioned above) needs larger samples to confirm the findings, these preliminary results suggest that OCT as a diagnostic tool for identifying tumor from normal renal tissue is unclear. With mixed conclusions among the published literature, distinguishing neoplastic changes in renal tissue using OCT may require improved image processing or quantification metrics to ultimately differentiate between tumor and normal tissue in the kidney.

If OCT is to be used in the clinic as an adjunct technology for assessing renal tumor margins intra-operatively, future studies will need to investigate the predictive value of the metric (or combination of metrics) that best establishes the cut-off values

between tumor and normal renal tissue. Also, if OCT is found to be a useful tool in the clinic during partial nephrectomy procedures, needle-based OCT probes may play an important role in aiding or replacing percutaneous needle biopsy. Imaging guidance could improve sampling error, or "optical biopsy" techniques may allow for more comprehensive assessment by not requiring tissue damage or excision.

5.5.Conclusions

With a ~12 μm axial and ~15 μm transverse resolution OCT system, we imaged multiple regions of both normal and tumor tissue from patients with renal masses. Based on the attenuation coefficients we extracted from both normal (4.41±0.74 mm^{-1}, 8 patients) and tumor (4.32±1.26 mm^{-1}, 9 patients) renal tissue in *ex vivo* specimens, we conclude that optical attenuation coefficient may not be a sensitive enough diagnostic parameter to distinguish renal neoplasms tissue from normal tissue. However, in conjunction with previous studies, a larger number of patient samples are necessary before reaching a more definitive conclusion on whether optical attenuation using OCT is a suitable diagnostic method for detecting renal neoplasms.

Furthermore, since qualitative differences can be observed between normal and tumor tissue in a majority of the patients, other quantitative parameters and image processing and analysis techniques may be able to better distinguish the two tissue types. In addition, a semi-automatic, computer-aided diagnostic algorithm may be more advantageous than a fully-automated method by allowing for physician input in determining the diagnosis of the tissue.

6. Conclusion

6.1.Summary and Impact of Work

The research described in this thesis includes one animal study and two human studies using OCT imaging technology as a diagnostic tool for medical imaging. The animal study and one human study deal with *in vivo* imaging while the second human study surveys *ex vivo* specimens only. Each component of this work will be summarized below in more detail.

The first component of this research entailed *in vivo* imaging of the living rat kidney to quantify renal blood flow. 3D OCT/DOCT imaging data sets revealed single glomerular blood flow of the capillary tufts within Bowman's space. 3D quantification parameters cumulative Doppler volume (CDV) and Doppler flow range (DFR) reflected pharmacologically-induced changes in renal blood flow for both increased and decreased flow rates. Glomerular arterioles (afferent/efferent) were visible in some data sets but absolute glomerular blood flow was not able to be determined. This work demonstrates the feasibility of quantifying glomerular blood flow *in vivo* and would be useful for studying specific renal disease models or for imaging glomerular blood flow of the human kidney during surgery. Since OCT/DOCT imaging depth is much deeper and with higher resolution than other imaging modalities, it may prove highly useful for studying disease progression longitudinally within the same animal because it can reveal subsurface structure and function significantly deeper than conventional microscopy techniques, and it can be miniaturized into small probes for minimally-invasive imaging.

The second component of this thesis is closely connected to the first in that we

translated OCT/DOCT imaging technology into the clinic to image the human kidney during transplantation procedures. Morphological and functional imaging of the human kidney *in vivo* was demonstrated using OCT/DOCT on the living human kidney following reperfusion. OCT structural imaging revealed uriniferous tubules within the renal parenchyma and DOCT revealed blood flow (both in cortical vessels and glomeruli). Imaging results were correlated with standard biomarkers (blood urea nitrogen and serum creatinine) using a semi-quantitative numerical scoring system. Ranking the OCT/DOCT imaging results and then comparing with post-graft function markers yielded insights into the usefulness of OCT/DOCT for evaluating kidney status after transplantation. With the small number of patients in this study, we demonstrated that renal tubules and blood flow can be visualized in real time immediately following reperfusion and that these parameters may help predict post-transplant renal function.

In the third section of this work we investigated the feasibility of OCT to distinguish tumor renal tissue from normal parenchyma in human kidney specimens *ex vivo*. Using a modified single exponential decay model for fitting the OCT axial scan attenuation, average attenuation coefficients of tumor and normal tissue were compared. When the two tissue types (i.e. normal versus tumor) were compared across all patients, the results were found to be not statistically significant. These results stand in contrast to a former report that found a significant difference between renal cancer tissue and normal tissue with a similar sample size. This work shows that a higher number of patient samples are required to come to a definitive conclusion about using the attenuation coefficient from OCT images as a diagnostic marker to identify tumor tissue apart from

normal tissue in the kidney.

6.2.Future Work

Given the research discussed in this thesis, several further studies and improvements can be proposed for future work. For demonstrating *in vivo* imaging of glomerular blood flow in animal models using OCT/DOCT, a full-scale study of a particular renal disease progression for patient-specific management would naturally ensue. Chronic kidney disease (CKD) is one renal disease that is known to have changes in renal morphology (tubular atrophy, glomerulosclerosis, interstitial fibrosis) and function (altered renal hemodynamics). OCT/DOCT may be a suitable technology for identifying and quantifying changes in these parameters that are associated with CKD progression. Since OCT intensity images can reveal the size, shape, and density of uriniferous tubules, and the size and shape of glomeruli, and since DOCT can reveal renal cortical and glomerular blood flow, OCT/DOCT imaging appears to be an excellent technological candidate for determining the stage of CKD and monitoring its progression.

Regarding the second component of this thesis, OCT/DOCT imaging of human kidney transplant to predict post-transplant graft function is an area of research that requires higher patient numbers to validate the sensitivity and specificity of the technique. Along with the continued *in vivo* OCT/DOCT imaging, 3D *in vivo* imaging could greatly assist in providing additional quantitative metrics for evaluating renal function. Quantitative metrics like glomerular blood flow and tubular volume ratio (tubule volume per volume of parenchyma) could prove to help physicians better understand the transplant kidney function soon after reperfusion rather than waiting hours

to days to receive urine and serum lab results that require time following the procedure to stabilize and become reliable measures.

In addition, an untapped research area associated with kidney transplantation is evaluating the status of donor kidneys, especially donor kidneys from heart beating cadavers. Unlike living donor kidneys that are transplanted into the recipient within a relatively short period of time after harvesting, cadaver kidneys are stored for multiple hours before being transplanted into the recipient. During this time the ischemic insult to the kidney eventually causes the cells to die and the organ to cease being viable for transplantation. However, at the present time there is no objective method to assess the status of these cadaver kidneys beyond judging their status based on the elapsed time since harvesting. OCT intensity imaging may provide an objective means whereby the physician can visualize the internal microstructure of the donor kidney to evaluate its status prior to its transplantation thereby replacing the need to have to rely on a highly variable criterion, such as the duration of ischemia. Knowing the status of the kidney based on its microstructure could be an avenue that opens the door for the assessment of a larger pool of donor kidneys that otherwise might not be available. OCT might also be able to help prevent kidneys that are in poor condition from being transplanted and undergo post-graft failure.

In the third component of this research, the most pressing future work appears to be the need to collect a higher number of samples to more rigidly test whether the attenuation coefficient is or is not a reliable metric for distinguishing tumor tissue from normal tissue in the kidney. With the high variability seen in our data and in other

published reports, it is possible that the attenuation coefficient may not be the best suited metric for characterizing renal neoplasms. Future work on this project could consist of developing more sensitive measures of the optical properties of renal tissue that can differentiate tumor from normal tissue. This may consist of more complicated optical attenuation models, or new optical or image analysis parameters. These options will need to be investigated before determining the ability of OCT in detecting renal neoplasms.

Also, a natural extension of the *ex vivo* tissue analysis is to conduct an *in vivo* pilot feasibility study using a laparoscopic OCT imaging probe. *In vivo* conditions of the kidney differ considerably from *ex vivo* due to changes in the tissue morphology and perfusion when removed from the body. Intra-operative OCT imaging of the kidney may encounter unforeseen challenges not incorporated in the preliminary *ex vivo* studies conducted so far. Animal studies of renal cancer would be a suitable model to test the differences that might be expected in the human kidney *in vivo*. This research will likely also need to be pursued.

6.3.Conclusions

OCT is a non-invasive imaging technology that measures backscattered light intensity on the micrometer scale allowing it to perform an "optical biopsy" of biological tissue in real time at resolutions approaching that of conventional histopathology without the need for tissue excision and processing. OCT is readily interfaced with miniature imaging devices such as endoscopes, laparoscopes, catheters, needles, and other surgical probes to address the needs of a vast array of procedures in various medical fields.

In conclusion, this research has demonstrated that OCT/DOCT can reveal

glomerular blood flow and renal microstructures *in vivo* and in real time. This was the first demonstration of 3D glomerular blood flow with OCT/DOCT technology. The tortuous and interwoven nature of the glomerular capillary bed was able to be visualized with 3D imaging. Glomerular blood flow was able to be quantified from 3D DOCT data volumes by measuring Doppler flow range (DFR) and cumulative Doppler volume (CDV) metrics. DOCT imaging detected changes in blood flow that were induced by administration of pharmacologic agents. Being able to quantify glomerular blood flow *in vivo* can be useful for studying renal disease progression, disease markers, and the effects of therapeutic interventions.

Next, OCT/DOCT imaging of the kidney intra-operatively using a hand-held probe revealed kidney tubular morphology and blood flow in the superficial cortex of the transplanted kidney immediately following blood reperfusion in the recipient. This was the first demonstration of the feasibility for using OCT to image the human transplant kidney. This technique could be useful for intra-operative monitoring and evaluation of the transplanted kidney as a prognostic and diagnostic tool for patient-specific management strategies that can enable therapeutic interventions to be administered in a timely manner. We conclude that visualizing renal microstructures and blood flow in real time with OCT/DOCT is feasible, and therefore, it is a promising technique that may be able to predict post-graft renal function sooner than other currently available methods. Imaging results were compared with standard biomarkers of renal function to investigate if morphological and functional parameters derived from OCT imaging could predict post-graft outcome. However, we currently have too few patients to evaluate these parameters as a prognostic and diagnostic marker for post-transplant renal function.

Additional patient numbers are needed in order to establish a correlation.

Finally, we performed OCT imaging of *ex vivo* renal neoplasms using OCT and analyzed the attenuation coefficient for normal and tumor tissue. We conclude that using the attenuation coefficient from the OCT axial scan requires more investigation and *in vivo* pilot studies to draw a definitive conclusion on whether it can be a reliable indicator between normal and tumor renal tissue. Furthermore, as OCT spectroscopy and image analysis techniques continue to be developed, in addition to OCT contrast agents,[250] OCT may be able to detect with greater accuracy and sensitivity pre-malignant neoplastic changes that would otherwise be undetectable *in vivo* with current technology.

OCT has been shown to be a promising tool for diagnositics in many clinical areas, and as the performance and capability of OCT continues to improve, OCT will surely become a powerful imaging modality for the diagnosis and management of many diseases. As a relatively-new, clinical imaging modality, OCT imaging speed and portability can be improved in conjunction with laser technology and electronics. New OCT delivery devices can also be developed that give rise to new applications in the medical field that are yet unexplored. OCT can be readily interfaced fiber-optically with several existing diagnostic imaging modalities for integration with instruments currently available in the clinical suite.

The utility of OCT in the clinic contains an unknown number of opportunities to be investigated. The work presented in this thesis on OCT/DOCT imaging of the kidney for studying renal diseases, for renal transplant diagnostics, and for renal cancer detection

is a step toward uncovering and defining its role in the field of nephrology.

7. References

1. Maiman, T.H., *Stimulated Optical Radiation in Ruby.* Nature, 1960. **187**(4736): p. 493-494.
2. Thompson, K.P., Ren, Q.S., and Parel, J.M., *Therapeutic and Diagnostic Application of Lasers in Ophthalmology.* Proceedings of the Ieee, 1992. **80**(6): p. 838-860.
3. Srinivasan, R., Dyer, P.E., and Braren, B., *Far-ultraviolet laser ablation of the cornea: photoacoustic studies.* Lasers Surg Med, 1987. **6**(6): p. 514-9.
4. Klyce, S.D. and Smolek, M.K., *Corneal topography of excimer laser photorefractive keratectomy.* J Cataract Refract Surg, 1993. **19 Suppl**: p. 122-30.
5. Gilmour, M.A., *Laser applications for corneal disease.* Clinical Techniques in Small Animal Practice, 2003. **18**(3): p. 199-202.
6. Dahm, J.B., *Excimer laser coronary angioplasty (ELCA) for diffuse in-stent restenosis: beneficial long-term results after sufficient debulking with a lesion-specific approach using various laser catheters.* Lasers Med Sci, 2001. **16**(2): p. 84-9.
7. Koster, R., Kahler, J., Brockhoff, C., Munzel, T., and Meinertz, T., *Laser coronary angioplasty: history, present and future.* Am J Cardiovasc Drugs, 2002. **2**(3): p. 197-207.
8. Raunest, J. and Lohnert, J., *Arthroscopic Cartilage Debridement by Excimer Laser in Chondromalacia of the Knee-Joint - a Prospective Randomized Clinical-Study.* Archives of Orthopaedic and Trauma Surgery, 1990. **109**(3): p. 155-159.
9. Jori, G. and Spikes, J.D., *Photothermal sensitizers: possible use in tumor therapy.* J Photochem Photobiol B, 1990. **6**(1-2): p. 93-101.
10. Leszczynski, D., Pitsillides, C.M., Pastila, R.K., Rox Anderson, R., and Lin, C.P., *Laser-beam-triggered microcavitation: a novel method for selective cell destruction.* Radiat Res, 2001. **156**(4): p. 399-407.
11. Pitsillides, C.M., Joe, E.K., Wei, X., Anderson, R.R., and Lin, C.P., *Selective cell targeting with light-absorbing microparticles and nanoparticles.* Biophys J, 2003. **84**(6): p. 4023-32.
12. Huang, X., Jain, P.K., El-Sayed, I.H., and El-Sayed, M.A., *Determination of the minimum temperature required for selective photothermal destruction of cancer cells with the use of immunotargeted gold nanoparticles.* Photochem Photobiol, 2006. **82**(2): p. 412-7.
13. Chen, W.R., Singhal, A.K., Liu, H., and Nordquist, R.E., *Antitumor immunity induced by laser immunotherapy and its adoptive transfer.* Cancer Res, 2001. **61**(2): p. 459-61.
14. Chen, W.R., Carubelli, R., Liu, H., and Nordquist, R.E., *Laser immunotherapy: a novel treatment modality for metastatic tumors.* Mol Biotechnol, 2003. **25**(1): p. 37-44.
15. Krueger, R.R. and Almquist, E.E., *Argon laser coagulation of blood for the anastomosis of small vessels.* Lasers Surg Med, 1985. **5**(1): p. 55-60.
16. Dolmans, D.E., Fukumura, D., and Jain, R.K., *Photodynamic therapy for cancer.* Nat Rev Cancer, 2003. **3**(5): p. 380-7.
17. Dougherty, T.J., Gomer, C.J., Henderson, B.W., Jori, G., Kessel, D., Korbelik,

M., Moan, J., and Peng, Q., *Photodynamic therapy.* J Natl Cancer Inst, 1998. **90**(12): p. 889-905.
18. Conlan, M.J., Rapley, J.W., and Cobb, C.M., *Biostimulation of wound healing by low-energy laser irradiation. A review.* J Clin Periodontol, 1996. **23**(5): p. 492-6.
19. Navratil, L. and Kymplova, J., *Contraindications in noninvasive laser therapy: truth and fiction.* J Clin Laser Med Surg, 2002. **20**(6): p. 341-3.
20. Choe, R., *Diffuse optical tomography & spectroscopy in breast cancer characterization & therapy monitoring at UPENN.* Conf Proc IEEE Eng Med Biol Soc, 2009. **2009**: p. 6335-7.
21. Corlu, A., Choe, R., Durduran, T., Rosen, M.A., Schweiger, M., Arridge, S.R., Schnall, M.D., and Yodh, A.G., *Three-dimensional in vivo fluorescence diffuse optical tomography of breast cancer in humans.* Opt Express, 2007. **15**(11): p. 6696-716.
22. Ntziachristos, V. and Chance, B., *Probing physiology and molecular function using optical imaging: applications to breast cancer.* Breast Cancer Res, 2001. **3**(1): p. 41-6.
23. Huang, D., Swanson, E.A., Lin, C.P., Schuman, J.S., Stinson, W.G., Chang, W., Hee, M.R., Flotte, T., Gregory, K., Puliafito, C.A., and Fujimoto, J.G., *Optical coherence tomography.* Science, 1991. **254**(5035): p. 1178-1181.
24. Walther, J., Gaertner, M., Cimalla, P., Burkhardt, A., Kirsten, L., Meissner, S., and Koch, E., *Optical coherence tomography in biomedical research.* Anal Bioanal Chem. **400**(9): p. 2721-43.
25. Sainter, A.W., King, T.A., and Dickinson, M.R., *Effect of target biological tissue and choice of light source on penetration depth and resolution in optical coherence tomography.* J Biomed Opt, 2004. **9**(1): p. 193-9.
26. Gambichler, T., Moussa, G., Sand, M., Sand, D., Altmeyer, P., and Hoffmann, K., *Applications of optical coherence tomography in dermatology.* J Dermatol Sci, 2005. **40**(2): p. 85-94.
27. Drexler, W., Morgner, U., Kartner, F.X., Pitris, C., Boppart, S.A., Li, X.D., Ippen, E.P., and Fujimoto, J.G., *In vivo ultrahigh-resolution optical coherence tomography.* Opt Lett, 1999. **24**(17): p. 1221-3.
28. Webb, R.H., *Confocal optical microscopy.* Reports on Progress in Physics, 1996. **59**(3): p. 427-471.
29. Wang, T.D., Mandella, M.J., Contag, C.H., and Kino, G.S., *Dual-axis confocal microscope for high-resolution in vivo imaging.* Optics Letters, 2003. **28**(6): p. 414-416.
30. de Boer, J.F., Milner, T.E., van Gemert, M.J., and Nelson, J.S., *Two-dimensional birefringence imaging in biological tissue by polarization-sensitive optical coherence tomography.* Opt Lett, 1997. **22**(12): p. 934-6.
31. Everett, M.J., Schoenenberger, K., Colston, B.W., Jr., and Da Silva, L.B., *Birefringence characterization of biological tissue by use of optical coherence tomography.* Opt Lett, 1998. **23**(3): p. 228-30.
32. Chen, Z., Milner, T.E., Srinivas, S., Wang, X., Malekafzali, A., van Gemert, M.J., and Nelson, J.S., *Noninvasive imaging of in vivo blood flow velocity using optical Doppler tomography.* Opt Lett, 1997. **22**(14): p. 1119-21.
33. Yazdanfar, S., Kulkarni, M., and Izatt, J., *High resolution imaging of in vivo*

cardiac dynamics using color Doppler optical coherence tomography. Opt Express, 1997. **1**(13): p. 424-31.
34. Best, S., Ercole, B., Lee, C., Fallon, E., Skenazy, J., and Monga, M., *Minimally invasive therapy for renal cell carcinoma: is there a new community standard?* Urology, 2004. **64**(1): p. 22-5.
35. Sengupta, S. and Zincke, H., *Lessons learned in the surgical management of renal cell carcinoma.* Urology, 2005. **66**(5 Suppl): p. 36-42.
36. Lam, J.S., Shvarts, O., and Pantuck, A.J., *Changing concepts in the surgical management of renal cell carcinoma.* Eur Urol, 2004. **45**(6): p. 692-705.
37. Zisman, A., Pantuck, A.J., Belldegrun, A.S., and Schulam, P.G., *Laparoscopic radical nephrectomy.* Semin Urol Oncol, 2001. **19**(2): p. 114-22.
38. Tearney, G.J., Brezinski, M.E., Bouma, B.E., Boppart, S.A., Pitvis, C., Southern, J.F., and Fujimoto, J.G., *In vivo endoscopic optical biopsy with optical coherence tomography.* Science, 1997. **276**(5321): p. 2037-2039.
39. Sergeev, A.M., Gelikonov, V.M., Gelikonov, G.V., Feldchtein, F.I., Kuranov, R.V., Gladkova, N.D., Shakhova, N.M., Suopova, L.B., Shakhov, A.V., Kuznetzova, I.A., Denisenko, A.N., Pochinko, V.V., Chumakov, Y.P., and Streltzova, O.S., *In vivo endoscopic OCT imaging of precancer and cancer states of human mucosa.* Optics Express, 1997. **1**(13): p. 432-440.
40. Li, X., Chudoba, C., Ko, T., Pitris, C., and Fujimoto, J.G., *Imaging needle for optical coherence tomography.* Optics Letters, 2000. **25**(20): p. 1520-2.
41. Gamelin, J., Yang, Y., Biswal, N., Chen, Y., Yan, S., Zhang, X., Karemeddini, M., Brewer, M., and Zhu, Q., *A prototype hybrid intraoperative probe for ovarian cancer detection.* Opt Express, 2009. **17**(9): p. 7245-58.
42. Jang, I.K., Bouma, B., MacNeill, B., Takano, M., Shishkov, M., Iftima, N., and Tearney, G.J., *In-vivo coronary plaque characteristics in patients with various clinical presentations using Optical Coherence Tomography.* Circulation, 2003. **108**(17): p. 373-373.
43. Bouma, B.E., Tearney, G.J., Compton, C.C., and Nishioka, N.S., *High-resolution imaging of the human esophagus and stomach in vivo using optical coherence tomography.* Gastrointestinal Endoscopy, 2000. **51**: p. 467-74.
44. Sivak, M.V., Jr., Kobayashi, K., Izatt, J.A., Rollins, A.M., Ung-Runyawee, R., Chak, A., Wong, R.C., Isenberg, G.A., and Willis, J., *High-resolution endoscopic imaging of the GI tract using optical coherence tomography.* Gastrointestinal Endoscopy, 2000. **51**: p. 474-9.
45. Li, X.D., Boppart, S.A., Van Dam, J., Mashimo, H., Mutinga, M., Drexler, W., Klein, M., Pitris, C., Krinsky, M.L., Brezinski, M.E., and Fujimoto, J.G., *Optical coherence tomography: advanced technology for the endoscopic imaging of Barrett's esophagus.* Endoscopy, 2000. **32**(12): p. 921-30.
46. Chen, Y., Aguirre, A.D., Hsiung, P.L., Desai, S., Herz, P.R., Pedrosa, M., Huang, Q., Figueiredo, M., Huang, S.W., Koski, A., Schmitt, J.M., Fujimoto, J.G., and Mashimo, H., *Ultrahigh resolution optical coherence tomography of Barrett's esophagus: preliminary descriptive clinical study correlating images with histology.* Endoscopy, 2007. **39**(7): p. 599-605.
47. Lam, S., Standish, B., Baldwin, C., McWilliams, A., leRiche, J., Gazdar, A., Vitkin, A.I., Yang, V., Ikeda, N., and MacAulay, C., *In vivo optical coherence*

tomography imaging of preinvasive bronchial lesions. Clin Cancer Res, 2008. **14**(7): p. 2006-11.
48. Wang, Z., Lee, C.S., Waltzer, W.C., Liu, J., Xie, H., Yuan, Z., and Pan, Y., *In vivo bladder imaging with microelectromechanical-systems-based endoscopic spectral domain optical coherence tomography.* J Biomed Opt, 2007. **12**(3): p. 034009.
49. Yang, V.X., Gordon, M., Tang, S.J., Marcon, N., Gardiner, G., Qi, B., Bisland, S., Seng-Yue, E., Lo, S., Pekar, J., Wilson, B., and Vitkin, I., *High speed, wide velocity dynamic range Doppler optical coherence tomography (Part III): in vivo endoscopic imaging of blood flow in the rat and human gastrointestinal tracts.* Opt Express, 2003. **11**(19): p. 2416-24.
50. Yang, V.X., Tang, S.J., Gordon, M.L., Qi, B., Gardiner, G., Cirocco, M., Kortan, P., Haber, G.B., Kandel, G., Vitkin, I.A., Wilson, B.C., and Marcon, N.E., *Endoscopic Doppler optical coherence tomography in the human GI tract: initial experience.* Gastrointest Endosc, 2005. **61**(7): p. 879-90.
51. Yazdanfar, S., Rollins, A.M., and Izatt, J.A., *Imaging and velocimetry of the human retinal circulation with color Doppler optical coherence tomography.* Opt Lett, 2000. **25**(19): p. 1448-50.
52. Yazdanfar, S., Rollins, A.M., and Izatt, J.A., *In vivo imaging of human retinal flow dynamics by color Doppler optical coherence tomography.* Arch Ophthalmol, 2003. **121**(2): p. 235-9.
53. White, B., Pierce, M., Nassif, N., Cense, B., Park, B., Tearney, G., Bouma, B., Chen, T., and de Boer, J., *In vivo dynamic human retinal blood flow imaging using ultra-high-speed spectral domain optical coherence tomography.* Opt Express, 2003. **11**(25): p. 3490-7.
54. Wang, Y., Bower, B.A., Izatt, J.A., Tan, O., and Huang, D., *In vivo total retinal blood flow measurement by Fourier domain Doppler optical coherence tomography.* J Biomed Opt, 2007. **12**(4): p. 041215.
55. Dagher, P.C., Herget-Rosenthal, S., Ruehm, S.G., Jo, S.K., Star, R.A., Agarwal, R., and Molitoris, B.A., *Newly developed techniques to study and diagnose acute renal failure.* J Am Soc Nephrol, 2003. **14**(8): p. 2188-98.
56. Yang, V., Gordon, M., Qi, B., Pekar, J., Lo, S., Seng-Yue, E., Mok, A., Wilson, B., and Vitkin, I., *High speed, wide velocity dynamic range Doppler optical coherence tomography (Part I): System design, signal processing, and performance.* Opt Express, 2003. **11**(7): p. 794-809.
57. Yang, V.X., Gordon, M., Seng-Yue, E., Lo, S., Qi, B., Pekar, J., Mok, A., Wilson, B., and Vitkin, I., *High speed, wide velocity dynamic range Doppler optical coherence tomography (Part II): Imaging in vivo cardiac dynamics of Xenopus laevis.* Opt Express, 2003. **11**(14): p. 1650-8.
58. Zhao, Y., Chen, Z., Saxer, C., Xiang, S., de Boer, J.F., and Nelson, J.S., *Phase-resolved optical coherence tomography and optical Doppler tomography for imaging blood flow in human skin with fast scanning speed and high velocity sensitivity.* Optics Letters, 2000. **25**(2): p. 114-16.
59. Rollins, A.M., Yazdanfar, S., Barton, J.K., and Izatt, J.A., *Real-time in vivo color Doppler optical coherence tomography.* Journal of Biomedical Optics, 2002. **7**(1): p. 123-9.

60. Westphal, V., Yazdanfar, S., Rollins, A.M., and Izatt, J.A., *Real-time, high velocity-resolution color Doppler optical coherence tomography.* Optics Letters, 2002. **27**(1): p. 34-6.
61. Ding, Z., Zhao, Y., Ren, H., Nelson, J.S., and Chen, Z., *Real-time phase-resolved optical coherence tomography and optical Doppler tomography.* Optics Express, 2002. **10**(5): p. 236-45.
62. Luo, Z., Wang, Z., Yuan, Z., Du, C., and Pan, Y., *Optical coherence Doppler tomography quantifies laser speckle contrast imaging for blood flow imaging in the rat cerebral cortex.* Opt Lett, 2008. **33**(10): p. 1156-8.
63. Yazdanfar, S., Rollins, A.M., and Izatt, J.A., *Imaging and velocimetry of the human retinal circulation with color Doppler optical coherence tomography.* Optics Letters, 2000. **25**(19): p. 1448-50.
64. Leitgeb, R.A., Schmetterer, L., Drexler, W., Fercher, A.F., Zawadzki, R.J., and Bajraszewski, T., *Real-time assessment of retinal blood flow with ultrafast acquisition by color Doppler Fourier domain optical coherence tomography.* Optics Express, 2003. **11**(23): p. 3116-3121.
65. White, B.R., Pierce, M.C., Nassif, N., Cense, B., Park, B.H., Tearney, G.J., Bouma, B.E., Chen, T.C., and de Boer, J.F., *In vivo dynamic human retinal blood flow imaging using ultra-high-speed spectral domain optical Doppler tomography.* Optics Express, 2003. **11**(25): p. 3490-3497.
66. Wang, Y., Lu, A., Gil-Flamer, J., Tan, O., Izatt, J.A., and Huang, D., *Measurement of total blood flow in the normal human retina using Doppler Fourier-domain optical coherence tomography.* Br J Ophthalmol, 2009. **93**(5): p. 634-7.
67. An, L. and Wang, R.K., *In vivo volumetric imaging of vascular perfusion within human retina and choroids with optical micro-angiography.* Opt Express, 2008. **16**(15): p. 11438-52.
68. Chen, Z., Milner, T.E., Srinivas, S., Wang, X., Malekafzali, A., van Gemert, M.J.C., and Nelson, J.S., *Noninvasive imaging of in vivo blood flow velocity using optical Doppler tomography.* Optics Letters, 1997. **22**(14): p. 1119-21.
69. Kehlet Barton, J., Izatt, J.A., Kulkarni, M.D., Yazdanfar, S., and Welch, A.J., *Three-dimensional reconstruction of blood vessels from in vivo color Doppler optical coherence tomography images.* Dermatology, 1999. **198**(4): p. 355-61.
70. Satomura, Y., Seki, J., Ooi, Y., Yanagida, T., and Seiyama, A., *In vivo imaging of the rat cerebral microvessels with optical coherence tomography.* Clinical Hemorheology and Microcirculation, 2004. **31**(1): p. 31-40.
71. Vakoc, B.J., Shishko, M., Yun, S.H., Oh, W.Y., Suter, M.J., Desjardins, A.E., Evans, J.A., Nishioka, N.S., Tearney, G.J., and Bouma, B.E., *Comprehensive esophageal microscopy by using optical frequency-domain imaging (with video).* Gastrointest Endosc, 2007. **65**(6): p. 898-905.
72. Yang, V.X.D., Gordon, M.L., Mok, A., Zhao, Y.H., Chen, Z.P., Cobbold, R.S.C., Wilson, B.C., and Vitkin, I.A., *Improved phase-resolved optical Doppler tomography using the Kasai velocity estimator and histogram segmentation.* Optics Communications, 2002. **208**(4-6): p. 209-214.
73. Yang, V.X.D., Gordon, M.L., Qi, B., Pekar, J., Lo, S., Seng-Yue, E., Mok, A., Wilson, B.C., and Vitkin, I.A., *High speed, wide velocity dynamic range Doppler*

optical coherence tomography (Part I): System design, signal processing, and performance. Optics Express, 2003. **11**(7): p. 794-809.
74. Michaely, R., Bachmann, A.H., Villiger, M.L., Blatter, C., Lasser, T., and Leitgeb, R.A., *Vectorial reconstruction of retinal blood flow in three dimensions measured with high resolution resonant Doppler Fourier domain optical coherence tomography.* J Biomed Opt, 2007. **12**(4): p. 041213.
75. Srinivasan, V.J., Sakadzic, S., Gorczynska, I., Ruvinskaya, S., Wu, W., Fujimoto, J.G., and Boas, D.A., *Quantitative cerebral blood flow with optical coherence tomography.* Opt Express, 2010. **18**(3): p. 2477-94.
76. Crouch, J.E., *Functional Human Anatomy*. 2 ed. 1972, Philadelphia: Lea & Febiger.
77. Porth, C.M., *Pathophysiology: Concepts of Altered Health States*. 7 ed. 2005, Philadelphia, PA: Lippincott Williams & Wilkins.
78. Jaworski, P.M. [cited; Available from: http://commons.wikimedia.org.
79. *Gray's Anatomy*. [cited; Available from: http://commons.wikimedia.org.
80. Satchell, S.C. and Braet, F., *Glomerular endothelial cell fenestrations: an integral component of the glomerular filtration barrier.* Am J Physiol Renal Physiol, 2009. **296**(5): p. F947-56.
81. Ogasawara, Y., Takehara, K., Yamamoto, T., Hashimoto, R., Nakamoto, H., and Kajiya, F., *Quantitative blood velocity mapping in glomerular capillaries by in vivo observation with an intravital videomicroscope.* Methods Inf Med, 2000. **39**(2): p. 175-8.
82. Ibrahim, H.N. and Hostetter, T.H., *Diabetic nephropathy.* J Am Soc Nephrol, 1997. **8**(3): p. 487-93.
83. O'Bryan, G.T. and Hostetter, T.H., *The renal hemodynamic basis of diabetic nephropathy.* Semin Nephrol, 1997. **17**(2): p. 93-100.
84. Ichikawa, I. and Fogo, A., *Focal segmental glomerulosclerosis.* Pediatr Nephrol, 1996. **10**(3): p. 374-91.
85. Szabo, Z., Xia, J., Mathews, W.B., and Brown, P.R., *Future direction of renal positron emission tomography.* Semin Nucl Med, 2006. **36**(1): p. 36-50.
86. Juillard, L., Janier, M.F., Fouque, D., Cinotti, L., Maakel, N., Le Bars, D., Barthez, P.Y., Pozet, N., and Laville, M., *Dynamic renal blood flow measurement by positron emission tomography in patients with CRF.* Am J Kidney Dis, 2002. **40**(5): p. 947-54.
87. Kudomi, N., Koivuviita, N., Liukko, K.E., Oikonen, V.J., Tolvanen, T., Iida, H., Tertti, R., Metsarinne, K., Iozzo, P., and Nuutila, P., *Parametric renal blood flow imaging using [15O]H2O and PET.* Eur J Nucl Med Mol Imaging, 2009. **36**(4): p. 683-91.
88. Nitzsche, E.U., Choi, Y., Killion, D., Hoh, C.K., Hawkins, R.A., Rosenthal, J.T., Buxton, D.B., Huang, S.C., Phelps, M.E., and Schelbert, H.R., *Quantification and parametric imaging of renal cortical blood flow in vivo based on Patlak graphical analysis.* Kidney Int, 1993. **44**(5): p. 985-96.
89. Middlekauff, H.R., Nitzsche, E.U., Nguyen, A.H., Hoh, C.K., and Gibbs, G.G., *Modulation of renal cortical blood flow during static exercise in humans.* Circ Res, 1997. **80**(1): p. 62-8.
90. Alpert, N.M., Rabito, C.A., Correia, D.J., Babich, J.W., Littman, B.H., Tompkins,

R.G., Rubin, N.T., Rubin, R.H., and Fischman, A.J., *Mapping of local renal blood flow with PET and H(2)(15)O.* J Nucl Med, 2002. **43**(4): p. 470-5.
91. Michoux, N., Montet, X., Pechere, A., Ivancevic, M.K., Martin, P.Y., Keller, A., Didier, D., Terrier, F., and Vallee, J.P., *Parametric and quantitative analysis of MR renographic curves for assessing the functional behaviour of the kidney.* Eur J Radiol, 2005. **54**(1): p. 124-35.
92. Vallee, J.P., Lazeyras, F., Khan, H.G., and Terrier, F., *Absolute renal blood flow quantification by dynamic MRI and Gd-DTPA.* Eur Radiol, 2000. **10**(8): p. 1245-52.
93. Bokacheva, L., Rusinek, H., Zhang, J.L., and Lee, V.S., *Assessment of renal function with dynamic contrast-enhanced MR imaging.* Magn Reson Imaging Clin N Am, 2008. **16**(4): p. 597-611, viii.
94. De Bazelaire, C., Rofsky, N.M., Duhamel, G., Michaelson, M.D., George, D., and Alsop, D.C., *Arterial spin labeling blood flow magnetic resonance imaging for the characterization of metastatic renal cell carcinoma(1).* Acad Radiol, 2005. **12**(3): p. 347-57.
95. Akinbi, H., Abbasi, S., Hilpert, P.L., and Bhutani, V.K., *Gastrointestinal and renal blood flow velocity profile in neonates with birth asphyxia.* J Pediatr, 1994. **125**(4): p. 625-7.
96. van Bel, F., Guit, G.L., Schipper, J., van de Bor, M., and Baan, J., *Indomethacin-induced changes in renal blood flow velocity waveform in premature infants investigated with color Doppler imaging.* J Pediatr, 1991. **118**(4 Pt 1): p. 621-6.
97. Wong, S.N., Lo, R.N., and Yu, E.C., *Renal blood flow pattern by noninvasive Doppler ultrasound in normal children and acute renal failure patients.* J Ultrasound Med, 1989. **8**(3): p. 135-41.
98. Yura, T., Yuasa, S., Fukunaga, M., Badr, K.F., and Matsuo, H., *Role for Doppler ultrasound in the assessment of renal circulation: effects of dopamine and dobutamine on renal hemodynamics in humans.* Nephron, 1995. **71**(2): p. 168-75.
99. Kalantarinia, K., Belcik, J.T., Patrie, J.T., and Wei, K., *Real-time measurement of renal blood flow in healthy subjects using contrast-enhanced ultrasound.* American Journal of Physiology-Renal Physiology, 2009. **297**(4): p. F1129-F1134.
100. Kay, D.H., Mazonakis, M., Geddes, C., and Baxter, G., *Ultrasonic microbubble contrast agents and the transplant kidney.* Clin Radiol, 2009. **64**(11): p. 1081-7.
101. Yamamoto, T., Tada, T., Brodsky, S.V., Tanaka, H., Noiri, E., Kajiya, F., and Goligorsky, M.S., *Intravital videomicroscopy of peritubular capillaries in renal ischemia.* Am J Physiol Renal Physiol, 2002. **282**(6): p. F1150-5.
102. Angelescu, M., Kraus, T., Wiesel, M., Hergesell, O., Haberkorn, U., and Klar, E., *Assessment of renal graft function by perioperative monitoring of cortical microcirculation in kidney transplantation.* Transplantation, 2003. **75**(8): p. 1190-6.
103. Anaise, D., Oster, Z.H., Atkins, H.L., Arnold, A.N., Weis, S., Waltzer, W.C., and Rapaport, F.T., *Cortex perfusion index: a sensitive detector of acute rejection crisis in transplanted kidneys.* J Nucl Med, 1986. **27**(11): p. 1697-701.
104. Hamilton, D., Miola, U.J., and Payne, M.C., *The renal transplant perfusion index: reduction in the error and variability.* Eur J Nucl Med, 1994. **21**(3): p. 232-8.

105. Andrews, P.M., Petroll, W.M., Cavanagh, H.D., and Jester, J.V., *Tandem scanning confocal microscopy (TSCM) of normal and ischemic living kidneys.* Am J Anat, 1991. **191**(1): p. 95-102.
106. Andrews, P.M., Khirabadi, B.S., and Bengs, B.C., *Using tandem scanning confocal microscopy to predict the status of donor kidneys.* Nephron, 2002. **91**(1): p. 148-55.
107. Campo-Ruiz, V., Lauwers, G.Y., Anderson, R.R., Delgado-Baeza, E., and Gonzalez, S., *Novel virtual biopsy of the kidney with near infrared, reflectance confocal microscopy: a pilot study in vivo and ex vivo.* J Urol, 2006. **175**(1): p. 327-36.
108. Kang, J.J., Toma, I., Sipos, A., McCulloch, F., and Peti-Peterdi, J., *Quantitative imaging of basic functions in renal (patho)physiology.* Am J Physiol Renal Physiol, 2006. **291**(2): p. F495-502.
109. Dunn, K.W., Sandoval, R.M., Kelly, K.J., Dagher, P.C., Tanner, G.A., Atkinson, S.J., Bacallao, R.L., and Molitoris, B.A., *Functional studies of the kidney of living animals using multicolor two-photon microscopy.* Am J Physiol Cell Physiol, 2002. **283**(3): p. C905-16.
110. Yu, W., Sandoval, R.M., and Molitoris, B.A., *Rapid determination of renal filtration function using an optical ratiometric imaging approach.* Am J Physiol Renal Physiol, 2007. **292**(6): p. F1873-80.
111. Clark, A.L., Gillenwater, A., Alizadeh-Naderi, R., El-Naggar, A.K., and Richards-Kortum, R., *Detection and diagnosis of oral neoplasia with an optical coherence microscope.* J Biomed Opt, 2004. **9**(6): p. 1271-80.
112. Chen, Y., Andrews, P.M., Aguirre, A.D., Schmitt, J.M., and Fujimoto, J.G., *High-resolution three-dimensional optical coherence tomography imaging of kidney microanatomy ex vivo.* J Biomed Opt, 2007. **12**(3): p. 034008.
113. Andrews, P.M., Chen, Y., Onozato, M.L., Huang, S.W., Adler, D.C., Huber, R.A., Jiang, J., Barry, S.E., Cable, A.E., and Fujimoto, J.G., *High-resolution optical coherence tomography imaging of the living kidney.* Lab Invest, 2008. **88**(4): p. 441-9.
114. Li, Q., Onozato, M.L., Andrews, P.M., Chen, C.W., Paek, A., Naphas, R., Yuan, S., Jiang, J., Cable, A., and Chen, Y., *Automated quantification of microstructural dimensions of the human kidney using optical coherence tomography (OCT).* Opt Express, 2009. **17**(18): p. 16000-16.
115. Onozato, M.L., Andrews, P.M., Li, Q., Jiang, J., Cable, A., and Chen, Y., *Optical coherence tomography of human kidney.* J Urol. **183**(5): p. 2090-4.
116. Tojo, A., *Optical coherence tomography in the kidney: a step toward echo microscopy.* J Urol. **183**(5): p. 1669-70.
117. Yang, V.X.D., Gordon, M., Qi, B., Pekar, J., Lo, S., Seng-Yue, E., Mok, A., Wilson, B., and Vitkin, I., *High speed, wide velocity dynamic range Doppler optical coherence tomography (Part I): System design, signal processing, and performance.* Opt Express, 2003. **11**(7): p. 794-809.
118. Yu, L. and Chen, Z., *Doppler variance imaging for three-dimensional retina and choroid angiography.* J Biomed Opt, 2010. **15**(1): p. 016029.
119. Wang, Y., Bower, B.A., Izatt, J.A., Tan, O., and Huang, D., *Retinal blood flow measurement by circumpapillary Fourier domain Doppler optical coherence*

tomography. J Biomed Opt, 2008. **13**(6): p. 064003.
120. Werkmeister, R.M., Dragostinoff, N., Pircher, M., Gotzinger, E., Hitzenberger, C.K., Leitgeb, R.A., and Schmetterer, L., *Bidirectional Doppler Fourier-domain optical coherence tomography for measurement of absolute flow velocities in human retinal vessels.* Opt Lett, 2008. **33**(24): p. 2967-9.
121. Barton, J., Izatt, J.A., Kulkarni, M.D., Yazdanfar, S., and Welch, A.J., *Three-dimensional reconstruction of blood vessels from in vivo color Doppler optical coherence tomography images.* Dermatology, 1999. **198**(4): p. 355-61.
122. Zhao, Y., Chen, Z., Saxer, C., Shen, Q., Xiang, S., de Boer, J.F., and Nelson, J.S., *Doppler standard deviation imaging for clinical monitoring of in vivo human skin blood flow.* Opt Lett, 2000. **25**(18): p. 1358-60.
123. Li, H., Standish, B.A., Mariampillai, A., Munce, N.R., Mao, Y., Chiu, S., Marcon, N.E., Wilson, B.C., Vitkin, A., and Yang, V.X.D., *Feasibility of interstitial Doppler optical coherence tomography for in vivo detection of microvascular changes during photodynamic therapy.* Lasers Surg Med, 2006. **38**(8): p. 754-61.
124. Yang, V.X.D., Tang, S.J., Gordon, M.L., Qi, B., Gardiner, G., Cirocco, M., Kortan, P., Haber, G.B., Kandel, G., Vitkin, I.A., Wilson, B.C., and Marcon, N.E., *Endoscopic Doppler optical coherence tomography in the human GI tract: initial experience.* Gastrointest Endosc, 2005. **61**(7): p. 879-90.
125. Hackbarth, H., Buttner, D., Jarck, D., Pothmann, M., Messow, C., and Gartner, K., *Distribution of glomeruli in the renal cortex of Munich Wistar Fromter (MWF) rats.* Ren Physiol, 1983. **6**(2): p. 63-71.
126. Stahl, W.M., *Effect of Mannitol on the Kidney: Changes in Intrarenal Hemodynamics.* N Engl J Med, 1965. **272**: p. 382-6.
127. Lindstrom, K.E., Ronnstedt, L., Jaremko, G., and Haraldsson, B., *Physiological and morphological effects of perfusing isolated rat kidneys with hyperosmolal mannitol solutions.* Acta Physiol Scand, 1999. **166**(3): p. 231-8.
128. Behnia, R., Koushanpour, E., and Brunner, E.A., *Effects of hyperosmotic mannitol infusion on hemodynamics of dog kidney.* Anesth Analg, 1996. **82**(5): p. 902-8.
129. Deng, X., Welch, W.J., and Wilcox, C.S., *Role of nitric oxide in short-term and prolonged effects of angiotensin II on renal hemodynamics.* Hypertension, 1996. **27**(5): p. 1173-9.
130. Ekelund, L. and Gothlin, J., *Effect of angiotensin on normal renal circulation determined by angiography and a dye dilution technique.* Acta Radiol Diagn (Stockh), 1977. **18**(1): p. 39-48.
131. Gothlin, J.H., Krakenes, J., and Tvete, S., *The effects of angiotensin on the diagnostics and haemodynamics in renal angiography.* Eur J Radiol, 1983. **3**(4): p. 328-30.
132. Hall, J.E. and Granger, J.P., *Renal hemodynamic actions of angiotensin II: interaction with tubuloglomerular feedback.* Am J Physiol, 1983. **245**(2): p. R166-73.
133. Denton, K.M., Anderson, W.P., and Sinniah, R., *Effects of angiotensin II on regional afferent and efferent arteriole dimensions and the glomerular pole.* Am J Physiol Regul Integr Comp Physiol, 2000. **279**(2): p. R629-38.
134. Yang, V.X.D., Gordon, M., Tang, S.J., Marcon, N., Gardiner, G., Qi, B., Bisland, S., Seng-Yue, E., Lo, S., Pekar, J., Wilson, B., and Vitkin, I., *High speed, wide*

velocity dynamic range Doppler optical coherence tomography (Part III): in vivo endoscopic imaging of blood flow in the rat and human gastrointestinal tracts. Opt Express, 2003. **11**(19): p. 2416-24.
135. Molitoris, B.A. and Sandoval, R.M., *Intravital multiphoton microscopy of dynamic renal processes.* Am J Physiol Renal Physiol, 2005. **288**(6): p. F1084-9.
136. Li, B., Yao, J., Kawamura, K., Oyanagi-Tanaka, Y., Hoshiyama, M., Morioka, T., Gejyo, F., Uchiyama, M., and Oite, T., *Real-time observation of glomerular hemodynamic changes in diabetic rats: effects of insulin and ARB.* Kidney Int, 2004. **66**(5): p. 1939-48.
137. Schmitz, V., Schaser, K.D., Olschewski, P., Neuhaus, P., and Puhl, G., *In vivo visualization of early microcirculatory changes following ischemia/reperfusion injury in human kidney transplantation.* Eur Surg Res, 2008. **40**(1): p. 19-25.
138. Adler, D.C., Chen, Y., Huber, R., Schmitt, J., Connolly, J., and Fujimoto, J.G., *Three-dimensional endomicroscopy using optical coherence tomography.* Nature Photonics, 2007. **1**(12): p. 709-716.
139. Yang, V.X.D., Mao, Y.X., Munce, N., Standish, B., Kucharczyk, W., Marcon, N.E., Wilson, B.C., and Vitkin, I.A., *Interstitial Doppler optical coherence tomography.* Optics Letters, 2005. **30**(14): p. 1791-3.
140. Hariri, L.P., Bonnema, G.T., Schmidt, K., Winkler, A.M., Korde, V., Hatch, K.D., Davis, J.R., Brewer, M.A., and Barton, J.K., *Laparoscopic optical coherence tomography imaging of human ovarian cancer.* Gynecol Oncol, 2009. **114**(2): p. 188-94.
141. Adler, D.C., Huber, R., and Fujimoto, J.G., *Phase-sensitive optical coherence tomography at up to 370,000 lines per second using buffered Fourier domain mode-locked lasers.* Opt Lett, 2007. **32**(6): p. 626-8.
142. Mariampillai, A., Leung, M.K., Jarvi, M., Standish, B.A., Lee, K., Wilson, B.C., Vitkin, A., and Yang, V.X., *Optimized speckle variance OCT imaging of microvasculature.* Opt Lett, 2010. **35**(8): p. 1257-9.
143. Makita, S., Hong, Y., Yamanari, M., Yatagai, T., and Yasuno, Y., *Optical coherence angiography.* Opt Express, 2006. **14**(17): p. 7821-40.
144. Wang, R.K., *Optical Microangiography: A Label Free 3D Imaging Technology to Visualize and Quantify Blood Circulations within Tissue Beds in vivo.* IEEE J Sel Top Quantum Electron, 2010. **16**(3): p. 545-554.
145. Chen, C.W., Betz, M.W., Fisher, J.P., Paek, A., and Chen, Y., *Macroporous hydrogel scaffolds and their characterization by optical coherence tomography.* Tissue Engineering: Part C, 2010. **in press**: p. DOI: 10.1089/ten.tec.2010.0072.
146. Dunkers, J., Cicerone, M., and Washburn, N., *Collinear optical coherence and confocal fluorescence microscopies for tissue engineering.* Opt Express, 2003. **11**(23): p. 3074-9.
147. Tang, S., Sun, C.H., Krasieva, T.B., Chen, Z., and Tromberg, B.J., *Imaging subcellular scattering contrast by using combined optical coherence and multiphoton microscopy.* Opt Lett, 2007. **32**(5): p. 503-5.
148. Vinegoni, C., Ralston, T., Tan, W., Luo, W., Marks, D.L., and Boppart, S.A., *Integrated structural and functional optical imaging combining spectral-domain optical coherence and multiphoton microscopy.* Applied Physics Letters, 2006. **88**(5): p. 053901.

149. Regan, M.C., Young, L.S., Geraghty, J., and Fitzpatrick, J.M., *Regional renal blood flow in normal and disease states.* Urol Res, 1995. **23**(1): p. 1-10.
150. Leitgeb, R.A., Drexler, W., Unterhuber, A., Hermann, B., Bajraszewski, T., Le, T., Stingl, A., and Fercher, A.F., *Ultrahigh resolution Fourier domain optical coherence tomography.* Optics Express, 2004. **12**(10): p. 2156-2165.
151. Drexler, W., *Ultrahigh-resolution optical coherence tomography.* Journal of Biomedical Optics, 2004. **9**(1): p. 47-74.
152. Lameire, N., Van Biesen, W., and Vanholder, R., *Acute renal failure.* Lancet, 2005. **365**(9457): p. 417-30.
153. Thadhani, R., Pascual, M., and Bonventre, J.V., *Acute renal failure.* N Engl J Med, 1996. **334**(22): p. 1448-60.
154. Nolan, C.R. and Anderson, R.J., *Hospital-acquired acute renal failure.* J Am Soc Nephrol, 1998. **9**(4): p. 710-8.
155. Liano, F. and Pascual, J., *Epidemiology of acute renal failure: a prospective, multicenter, community-based study. Madrid Acute Renal Failure Study Group.* Kidney Int, 1996. **50**(3): p. 811-8.
156. Anderson, R.J. and Barry, D.W., *Clinical and laboratory diagnosis of acute renal failure.* Best Pract Res Clin Anaesthesiol, 2004. **18**(1): p. 1-20.
157. Star, R.A., *Treatment of acute renal failure.* Kidney Int, 1998. **54**(6): p. 1817-31.
158. Dubovsky, E.V., Russell, C.D., Bischof-Delaloye, A., Bubeck, B., Chaiwatanarat, T., Hilson, A.J., Rutland, M., Oei, H.Y., Sfakianakis, G.N., and Taylor, A., Jr., *Report of the Radionuclides in Nephrourology Committee for evaluation of transplanted kidney (review of techniques).* Semin Nucl Med, 1999. **29**(2): p. 175-88.
159. Bellomo, R., Kellum, J.A., and Ronco, C., *Defining acute renal failure: physiological principles.* Intensive Care Med, 2004. **30**(1): p. 33-7.
160. Perico, N., Cattaneo, D., Sayegh, M.H., and Remuzzi, G., *Delayed graft function in kidney transplantation.* Lancet, 2004. **364**(9447): p. 1814-27.
161. Moran, K., Mulhall, J., Kelly, D., Sheehan, S., Dowsett, J., Dervan, P., and Fitzpatrick, J.M., *Morphological changes and alterations in regional intrarenal blood flow induced by graded renal ischemia.* J Urol, 1992. **148**(2 Pt 1): p. 463-6.
162. Taylor, A., Jr., Eshima, D., and Alazraki, N., *99mTc-MAG3, a new renal imaging agent: preliminary results in patients.* Eur J Nucl Med, 1987. **12**(10): p. 510-4.
163. Russell, C.D., Thorstad, B.L., Stutzman, M.E., Yester, M.V., Fowler, D., and Dubovsky, E.V., *The kidney: imaging with Tc-99m mercaptoacetyltriglycine, a technetium-labeled analog of iodohippurate.* Radiology, 1989. **172**(2): p. 427-30.
164. Aktas, A., Aras, M., Colak, T., Gencoglu, A., and Karakayali, H., *Comparison of Tc-99m DTPA and Tc-99m MAG3 perfusion time-activity curves in patients with renal allograft dysfunction.* Transplant Proc, 2006. **38**(2): p. 449-53.
165. Taylor, A., Jr., Ziffer, J.A., and Eshima, D., *Comparison of Tc-99m MAG3 and Tc-99m DTPA in renal transplant patients with impaired renal function.* Clin Nucl Med, 1990. **15**(6): p. 371-8.
166. Juillard, L., Janier, M.F., Fouque, D., Lionnet, M., Le Bars, D., Cinotti, L., Barthez, P., Gharib, C., and Laville, M., *Renal blood flow measurement by positron emission tomography using 15O-labeled water.* Kidney Int, 2000. **57**(6): p. 2511-8.

167. Chen, B.C., Germano, G., Huang, S.C., Hawkins, R.A., Hansen, H.W., Robert, M.J., Buxton, D.B., Schelbert, H.R., Kurtz, I., and Phelps, M.E., *A new noninvasive quantification of renal blood flow with N-13 ammonia, dynamic positron emission tomography, and a two-compartment model.* J Am Soc Nephrol, 1992. **3**(6): p. 1295-306.
168. Shelton, M.E., Green, M.A., Mathias, C.J., Welch, M.J., and Bergmann, S.R., *Assessment of regional myocardial and renal blood flow with copper-PTSM and positron emission tomography.* Circulation, 1990. **82**(3): p. 990-7.
169. Huang, A.J., Lee, V.S., and Rusinek, H., *MR imaging of renal function.* Radiol Clin North Am, 2003. **41**(5): p. 1001-17.
170. Huang, A.J., Lee, V.S., and Rusinek, H., *Functional renal MR imaging.* Magn Reson Imaging Clin N Am, 2004. **12**(3): p. 469-86, vi.
171. Kobayashi, H., Kawamoto, S., Jo, S.K., Sato, N., Saga, T., Hiraga, A., Konishi, J., Hu, S., Togashi, K., Brechbiel, M.W., and Star, R.A., *Renal tubular damage detected by dynamic micro-MRI with a dendrimer-based magnetic resonance contrast agent.* Kidney Int, 2002. **61**(6): p. 1980-5.
172. Montet, X., Ivancevic, M.K., Belenger, J., Jorge-Costa, M., Pochon, S., Pechere, A., Terrier, F., and Vallee, J.P., *Noninvasive measurement of absolute renal perfusion by contrast medium-enhanced magnetic resonance imaging.* Invest Radiol, 2003. **38**(9): p. 584-92.
173. Ludemann, L., Nafz, B., Elsner, F., Grosse-Siestrup, C., Meissler, M., Kaufels, N., Rehbein, H., Persson, P.B., Michaely, H.J., Lengsfeld, P., Voth, M., and Gutberlet, M., *Absolute quantification of regional renal blood flow in swine by dynamic contrast-enhanced magnetic resonance imaging using a blood pool contrast agent.* Invest Radiol, 2009. **44**(3): p. 125-34.
174. Detre, J.A., Wang, J., Wang, Z., and Rao, H., *Arterial spin-labeled perfusion MRI in basic and clinical neuroscience.* Curr Opin Neurol, 2009. **22**(4): p. 348-55.
175. Wang, J.J., Hendrich, K.S., Jackson, E.K., Ildstad, S.T., Williams, D.S., and Ho, C., *Perfusion quantitation in transplanted rat kidney by MRI with arterial spin labeling.* Kidney Int, 1998. **53**(6): p. 1783-91.
176. Williams, D.S., Zhang, W., Koretsky, A.P., and Adler, S., *Perfusion imaging of the rat kidney with MR.* Radiology, 1994. **190**(3): p. 813-8.
177. Golay, X. and Petersen, E.T., *Arterial spin labeling: benefits and pitfalls of high magnetic field.* Neuroimaging Clin N Am, 2006. **16**(2): p. 259-68, x.
178. Petersen, E.T., Zimine, I., Ho, Y.C., and Golay, X., *Non-invasive measurement of perfusion: a critical review of arterial spin labelling techniques.* Br J Radiol, 2006. **79**(944): p. 688-701.
179. Pollock, J.M., Tan, H., Kraft, R.A., Whitlow, C.T., Burdette, J.H., and Maldjian, J.A., *Arterial spin-labeled MR perfusion imaging: clinical applications.* Magn Reson Imaging Clin N Am, 2009. **17**(2): p. 315-38.
180. Wei, K., Le, E., Bin, J.P., Coggins, M., Thorpe, J., and Kaul, S., *Quantification of renal blood flow with contrast-enhanced ultrasound.* J Am Coll Cardiol, 2001. **37**(4): p. 1135-40.
181. Mule, S., De Cesare, A., Lucidarme, O., Frouin, F., and Herment, A., *Regularized estimation of contrast agent attenuation to improve the imaging of microbubbles in small animal studies.* Ultrasound Med Biol, 2008. **34**(6): p. 938-48.

182. Sullivan, J.C., Wang, B., Boesen, E.I., D'Angelo, G., Pollock, J.S., and Pollock, D.M., *Novel use of ultrasound to examine regional blood flow in the mouse kidney.* Am J Physiol Renal Physiol, 2009. **297**(1): p. F228-35.
183. Wan, L., Yang, N., Hiew, C.Y., Schelleman, A., Johnson, L., May, C., and Bellomo, R., *An assessment of the accuracy of renal blood flow estimation by Doppler ultrasound.* Intensive Care Med, 2008. **34**(8): p. 1503-10.
184. Fujimoto, J.G., *Optical coherence tomography for ultrahigh resolution in vivo imaging.* Nature Biotechnology, 2003. **21**(11): p. 1361-1367.
185. Bouma, B.E., Yun, S.H., Vakoc, B.J., Suter, M.J., and Tearney, G.J., *Fourier-domain optical coherence tomography: recent advances toward clinical utility.* Curr Opin Biotechnol, 2009. **20**(1): p. 111-8.
186. Schuman, J.S., Puliafito, C.A., and Fujimoto, J.G., *Optical coherence tomography of ocular diseases (2nd Edition)*. 2004, Thorofare, NJ: Slack Inc.
187. D'Amico, A.V., Weinstein, M., Li, X., Richie, J.P., and Fujimoto, J., *Optical coherence tomography as a method for identifying benign and malignant microscopic structures in the prostate gland.* Urology, 2000. **55**(5): p. 783-7.
188. Pitris, C., Goodman, A., Boppart, S.A., Libus, J.J., Fujimoto, J.G., and Brezinski, M.E., *High-resolution imaging of gynecologic neoplasms using optical coherence tomography.* Obstetrics and Gynecology, 1999. **93**(1): p. 135-9.
189. Evans, J.A., Poneros, J.M., Bouma, B.E., Bressner, J., Halpern, E.F., Shishkov, M., Lauwers, G.Y., Mino-Kenudson, M., Nishioka, N.S., and Tearney, G.J., *Optical coherence tomography to identify intramucosal carcinoma and high-grade dysplasia in Barrett's esophagus.* Clinical Gastroenterology and Hepatology, 2006. **4**(1): p. 38-43.
190. Scheeren, T.W., Martin, K., Maruschke, M., and Hakenberg, O.W., *Prognostic value of intraoperative renal tissue oxygenation measurement on early renal transplant function.* Transpl Int. **24**(7): p. 687-96.
191. Snoeijs, M.G., Vink, H., Voesten, N., Christiaans, M.H., Daemen, J.W., Peppelenbosch, A.G., Tordoir, J.H., Peutz-Kootstra, C.J., Buurman, W.A., Schurink, G.W., and van Heurn, L.W., *Acute ischemic injury to the renal microvasculature in human kidney transplantation.* Am J Physiol Renal Physiol. **299**(5): p. F1134-40.
192. Andrews, P.M., Khirabadi, B.S., and Bengs, B.C., *Using vital microscopy (tscm) to evaluate living kidneys.* Ital J Anat Embryol, 2001. **106**(2 Suppl 1): p. 439-48.
193. Hattori, R., Ono, Y., Kato, M., Komatsu, T., Matsukawa, Y., and Yamamoto, T., *Direct visualization of cortical peritubular capillary of transplanted human kidney with reperfusion injury using a magnifying endoscopy.* Transplantation, 2005. **79**(9): p. 1190-4.
194. Huber, R., Adler, D.C., and Fujimoto, J.G., *Buffered Fourier domain mode locking: unidirectional swept laser sources for optical coherence tomography imaging at 370,000 lines/s.* Optics Letters, 2006. **31**(20): p. 2975-2977.
195. Moon, S. and Kim, D.Y., *Ultra-high-speed optical coherence tomography with a stretched pulse supercontinuum source.* Optics Express, 2006. **14**(24): p. 11575-11584.
196. Wieser, W., Biedermann, B.R., Klein, T., Eigenwillig, C.M., and Huber, R., *Multi-Megahertz OCT: High quality 3D imaging at 20 million A-scans and 4.5*

GVoxels per second. Optics Express, 2010. **18**(14): p. 14685-14704.
197. Siegel, R., Ward, E., Brawley, O., and Jemal, A., *Cancer statistics, 2011: the impact of eliminating socioeconomic and racial disparities on premature cancer deaths.* CA Cancer J Clin. **61**(4): p. 212-36.
198. American Cancer Society. *Kidney Cancer (Adult) - Renal Cell Carcinoma*. 2011 [cited; Available from: http://www.cancer.org/Cancer/KidneyCancer/DetailedGuide/kidney-cancer-adult-key-statistics.
199. Cohen, H.T. and McGovern, F.J., *Renal-cell carcinoma.* N Engl J Med, 2005. **353**(23): p. 2477-90.
200. Novick, A.C., *Kidney cancer: past, present, and future.* Urol Oncol, 2007. **25**(3): p. 188-95.
201. Chow, W.H., Devesa, S.S., Warren, J.L., and Fraumeni, J.F., Jr., *Rising incidence of renal cell cancer in the United States.* JAMA, 1999. **281**(17): p. 1628-31.
202. Frank, I., Blute, M.L., Cheville, J.C., Lohse, C.M., Weaver, A.L., and Zincke, H., *Solid renal tumors: an analysis of pathological features related to tumor size.* J Urol, 2003. **170**(6 Pt 1): p. 2217-20.
203. Gill, I.S., Matin, S.F., Desai, M.M., Kaouk, J.H., Steinberg, A., Mascha, E., Thornton, J., Sherief, M.H., Strzempkowski, B., and Novick, A.C., *Comparative analysis of laparoscopic versus open partial nephrectomy for renal tumors in 200 patients.* J Urol, 2003. **170**(1): p. 64-8.
204. Silverman, S.G., Gan, Y.U., Mortele, K.J., Tuncali, K., and Cibas, E.S., *Renal masses in the adult patient: the role of percutaneous biopsy.* Radiology, 2006. **240**(1): p. 6-22.
205. Schmidbauer, J., Remzi, M., Memarsadeghi, M., Haitel, A., Klingler, H.C., Katzenbeisser, D., Wiener, H., and Marberger, M., *Diagnostic accuracy of computed tomography-guided percutaneous biopsy of renal masses.* Eur Urol, 2008. **53**(5): p. 1003-11.
206. Link, R.E., Bhayani, S.B., Allaf, M.E., Varkarakis, I., Inagaki, T., Rogers, C., Su, L.M., Jarrett, T.W., and Kavoussi, L.R., *Exploring the learning curve, pathological outcomes and perioperative morbidity of laparoscopic partial nephrectomy performed for renal mass.* J Urol, 2005. **173**(5): p. 1690-4.
207. Dechet, C.B., Zincke, H., Sebo, T.J., King, B.F., LeRoy, A.J., Farrow, G.M., and Blute, M.L., *Prospective analysis of computerized tomography and needle biopsy with permanent sectioning to determine the nature of solid renal masses in adults.* J Urol, 2003. **169**(1): p. 71-4.
208. Hollingsworth, J.M., Miller, D.C., Daignault, S., and Hollenbeck, B.K., *Rising incidence of small renal masses: a need to reassess treatment effect.* J Natl Cancer Inst, 2006. **98**(18): p. 1331-4.
209. Mabjeesh, N.J., Avidor, Y., and Matzkin, H., *Emerging nephron sparing treatments for kidney tumors: a continuum of modalities from energy ablation to laparoscopic partial nephrectomy.* J Urol, 2004. **171**(2 Pt 1): p. 553-60.
210. Uzzo, R.G. and Novick, A.C., *Nephron sparing surgery for renal tumors: indications, techniques and outcomes.* J Urol, 2001. **166**(1): p. 6-18.
211. Fergany, A.F., Hafez, K.S., and Novick, A.C., *Long-term results of nephron sparing surgery for localized renal cell carcinoma: 10-year followup.* J Urol,

2000. **163**(2): p. 442-5.
212. Lane, B.R. and Gill, I.S., *5-Year outcomes of laparoscopic partial nephrectomy.* J Urol, 2007. **177**(1): p. 70-4; discussion 74.
213. Atwell, T.D., Farrell, M.A., Callstrom, M.R., Charboneau, J.W., Leibovich, B.C., Patterson, D.E., Chow, G.K., and Blute, M.L., *Percutaneous cryoablation of 40 solid renal tumors with US guidance and CT monitoring: initial experience.* Radiology, 2007. **243**(1): p. 276-83.
214. Atwell, T.D., Farrell, M.A., Callstrom, M.R., Charboneau, J.W., Leibovich, B.C., Frank, I., and Patterson, D.E., *Percutaneous cryoablation of large renal masses: technical feasibility and short-term outcome.* AJR Am J Roentgenol, 2007. **188**(5): p. 1195-200.
215. Wood, B.J., Ramkaransingh, J.R., Fojo, T., Walther, M.M., and Libutti, S.K., *Percutaneous tumor ablation with radiofrequency.* Cancer, 2002. **94**(2): p. 443-51.
216. Varkarakis, I.M., Allaf, M.E., Inagaki, T., Bhayani, S.B., Chan, D.Y., Su, L.M., Jarrett, T.W., Kavoussi, L.R., and Solomon, S.B., *Percutaneous radio frequency ablation of renal masses: results at a 2-year mean followup.* J Urol, 2005. **174**(2): p. 456-60; discussion 460.
217. Schmitt, J.M., *Optical coherence tomography (OCT): a review.* IEEE Journal of Selected Topics in Quantum Electronics, 1999. **5**(4): p. 1205-15.
218. Linehan, J.A., Bracamonte, E.R., Hariri, L.P., Sokoloff, M.H., Rice, P.S., Barton, J.K., and Nguyen, M.M., *Feasibility of optical coherence tomography imaging to characterize renal neoplasms: limitations in resolution and depth of penetration.* BJU Int.
219. Erdogan, F., Demirel, A., and Polat, O., *Prognostic significance of morphologic parameters in renal cell carcinoma.* Int J Clin Pract, 2004. **58**(4): p. 333-6.
220. Fuhrman, S.A., Lasky, L.C., and Limas, C., *Prognostic significance of morphologic parameters in renal cell carcinoma.* Am J Surg Pathol, 1982. **6**(7): p. 655-63.
221. Medeiros, L.J., Gelb, A.B., and Weiss, L.M., *Renal cell carcinoma. Prognostic significance of morphologic parameters in 121 cases.* Cancer, 1988. **61**(8): p. 1639-51.
222. Bensalah, K., Peswani, D., Tuncel, A., Raman, J.D., Zeltser, I., Liu, H., and Cadeddu, J., *Optical reflectance spectroscopy to differentiate benign from malignant renal tumors at surgery.* Urology, 2009. **73**(1): p. 178-81.
223. Bensalah, K., Tuncel, A., Peshwani, D., Zeltser, I., Liu, H., and Cadeddu, J., *Optical reflectance spectroscopy to differentiate renal tumor from normal parenchyma.* J Urol, 2008. **179**(5): p. 2010-3.
224. Parekh, D.J., Lin, W.C., and Herrell, S.D., *Optical spectroscopy characteristics can differentiate benign and malignant renal tissues: a potentially useful modality.* J Urol, 2005. **174**(5): p. 1754-8.
225. Schmitt, J.M., Knuttel, A., and Bonner, R.F., *Measurement of Optical-Properties of Biological Tissues by Low-Coherence Reflectometry.* Applied Optics, 1993. **32**(30): p. 6032-6042.
226. Barwari, K., de Bruin, D.M., Cauberg, E.C., Faber, D.J., van Leeuwen, T.G., Wijkstra, H., de la Rosette, J., and Laguna, M.P., *Advanced diagnostics in renal*

mass using optical coherence tomography: a preliminary report. J Endourol. **25**(2): p. 311-5.
227. Faber, D., van der Meer, F., Aalders, M., and van Leeuwen, T., *Quantitative measurement of attenuation coefficients of weakly scattering media using optical coherence tomography.* Opt Express, 2004. **12**(19): p. 4353-65.
228. Sakata, L.M., Deleon-Ortega, J., Sakata, V., and Girkin, C.A., *Optical coherence tomography of the retina and optic nerve - a review.* Clin Experiment Ophthalmol, 2009. **37**(1): p. 90-9.
229. Kubo, T. and Akasaka, T., *Recent advances in intracoronary imaging techniques: focus on optical coherence tomography.* Expert Rev Med Devices, 2008. **5**(6): p. 691-7.
230. Kubo, T., Ino, Y., Tanimoto, T., Kitabata, H., Tanaka, A., and Akasaka, T., *Optical coherence tomography imaging in acute coronary syndromes.* Cardiol Res Pract. **2011**: p. 312978.
231. Adler, D.C., Zhou, C., Tsai, T.H., Lee, H.C., Becker, L., Schmitt, J.M., Huang, Q., Fujimoto, J.G., and Mashimo, H., *Three-dimensional optical coherence tomography of Barrett's esophagus and buried glands beneath neosquamous epithelium following radiofrequency ablation.* Endoscopy, 2009. **41**(9): p. 773-6.
232. Shen, B. and Zuccaro, G., Jr., *Optical coherence tomography in the gastrointestinal tract.* Gastrointest Endosc Clin N Am, 2004. **14**(3): p. 555-71, x.
233. Testoni, P.A. and Mangiavillano, B., *Optical coherence tomography in detection of dysplasia and cancer of the gastrointestinal tract and bilio-pancreatic ductal system.* World J Gastroenterol, 2008. **14**(42): p. 6444-52.
234. Boppart, S.A., Luo, W., Marks, D.L., and Singletary, K.W., *Optical coherence tomography: feasibility for basic research and image-guided surgery of breast cancer.* Breast Cancer Res Treat, 2004. **84**(2): p. 85-97.
235. Pitris, C., Jesser, C., Boppart, S.A., Stamper, D., Brezinski, M.E., and Fujimoto, J.G., *Feasibility of optical coherence tomography for high-resolution imaging of human gastrointestinal tract malignancies.* J Gastroenterol, 2000. **35**(2): p. 87-92.
236. Zagaynova, E., Manyak, M.J., Streltsova, O., Gladkova, N., Feldchtein, F., and Kamensky, V., *A multicenter study of optical coherence tomography for diagnosis and guided surgery of bladder cancer.* Journal of Clinical Oncology, 2004. **22**(14): p. 391s-391s.
237. Gambichler, T., Regeniter, P., Bechara, F.G., Orlikov, A., Vasa, R., Moussa, G., Stucker, M., Altmeyer, P., and Hoffmann, K., *Characterization of benign and malignant melanocytic skin lesions using optical coherence tomography in vivo.* J Am Acad Dermatol, 2007. **57**(4): p. 629-37.
238. Kawakami-Wong, H., Gu, S., Hammer-Wilson, M.J., Epstein, J.B., Chen, Z., and Wilder-Smith, P., *In vivo optical coherence tomography-based scoring of oral mucositis in human subjects: a pilot study.* J Biomed Opt, 2007. **12**(5): p. 051702.
239. Escobar, P.F., Rojas-Espaillat, L., Tisci, S., Enerson, C., Brainard, J., Smith, J., Tresser, N.J., Feldchtein, F.I., Rojas, L.B., and Belinson, J.L., *Optical coherence tomography as a diagnostic aid to visual inspection and colposcopy for preinvasive and invasive cancer of the uterine cervix.* International Journal of Gynecological Cancer, 2006. **16**(5): p. 1815-1822.
240. Whiteman, S.C., Yang, Y., van Pittius, D.G., Stephens, M., Parmer, J., and

Spiteri, M.A., *Optical coherence tomography: Real-time imaging of bronchial airways microstructure and detection of inflammatory/neoplastic morphologic changes.* Clinical Cancer Research, 2006. **12**(3): p. 813-818.
241. Bohringer, H.J., Boller, D., Leppert, J., Knopp, U., Lankenau, E., Reusche, E., Huttmann, G., and Giese, A., *Time-domain and spectral-domain optical coherence tomography in the analysis of brain tumor tissue.* Lasers in Surgery and Medicine, 2006. **38**(6): p. 588-597.
242. Goldberg, B.D., Iftimia, N.V., Bressner, J.E., Pitman, M.B., Halpern, E., Bouma, B.E., and Tearney, G.J., *Automated algorithm for differentiation of human breast tissue using low coherence interferometry for fine needle aspiration biopsy guidance.* J Biomed Opt, 2008. **13**(1): p. 014014.
243. Tsai, M.T., Lee, H.C., Lee, C.K., Yu, C.H., Chen, H.M., Chiang, C.P., Chang, C.C., Wang, Y.M., and Yang, C.C., *Effective indicators for diagnosis of oral cancer using optical coherence tomography.* Optics Express, 2008. **16**(20): p. 15847-15862.
244. Tsai, M.T., Lee, H.C., Lu, C.W., Wang, Y.M., Lee, C.K., Yang, C.C., and Chiang, C.P., *Delineation of an oral cancer lesion with swept-source optical coherence tomography.* Journal of Biomedical Optics, 2008. **13**(4): p. 044012.
245. Turchin, I.V., Sergeeva, E.A., Dolin, L.S., Kamensky, V.A., Shakhova, N.M., and Richards-Kortum, R., *Novel algorithm of processing optical coherence tomography images for differentiation of biological tissue pathologies.* Journal of Biomedical Optics, 2005. **10**(6): p. 064024.
246. Zysk, A.M. and Boppart, S.A., *Computational methods for analysis of human breast tumor tissue in optical coherence tomography images.* Journal of Biomedical Optics, 2006. **11**(5).
247. Qi, X., Sivak, M.V., Isenberg, G., Willis, J.E., and Rollins, A.M., *Computer-aided diagnosis of dysplasia in Barrett's esophagus using endoscopic optical coherence tomography.* Journal of Biomedical Optics, 2006. **11**(4).
248. Goldberg, B.D., Iftimia, N.V., Bressner, J.E., Pitman, M.B., Halpern, E., Bouma, B.E., and Tearney, G.J., *Automated algorithm for differentiation of human breast tissue using low coherence interferometry for fine needle aspiration biopsy guidance.* Journal of Biomedical Optics, 2008. **13**(1).
249. Chen, Y., Aguirre, A.D., Hsiung, P.L., Huang, S.W., Mashimo, H., Schmitt, J.M., and Fujimoto, J.G., *Effects of axial resolution improvement on optical coherence tomography (OCT) imaging of gastrointestinal tissues.* Optics Express, 2008. **16**(4): p. 2469-2485.
250. Kim, C.S., Wilder-Smith, P., Ahn, Y.C., Liaw, L.H., Chen, Z., and Kwon, Y.J., *Enhanced detection of early-stage oral cancer in vivo by optical coherence tomography using multimodal delivery of gold nanoparticles.* J Biomed Opt, 2009. **14**(3): p. 034008.